Large-Scale Three Dimensional Modelling of a Direct Methanol Fuel Cell Stack

John Wilkie McIntyre

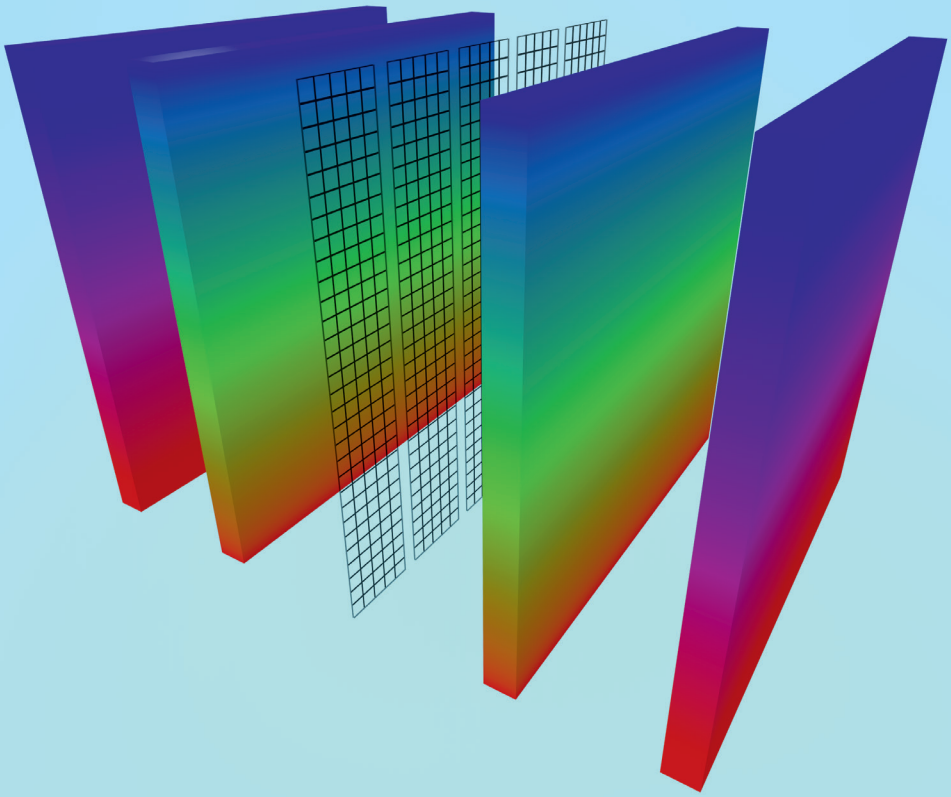

Energie & Umwelt / Energy & Environment
Band / Volume 289
ISBN 978-3-95806-094-4

JÜLICH
FORSCHUNGSZENTRUM

Schriften des Forschungszentrums Jülich
Reihe Energie & Umwelt / Energy & Environment Band / Volume 289

Forschungszentrum Jülich GmbH
Institute of Energy and Climate Research
Electrochemical Process Engineering (IEK-3)

Large-Scale Three Dimensional Modelling of a Direct Methanol Fuel Cell Stack

John Wilkie McIntyre

Schriften des Forschungszentrums Jülich
Reihe Energie & Umwelt / Energy & Environment Band / Volume 289

ISSN 1866-1793 ISBN 978-3-95806-094-4

Bibliographic information published by the Deutsche Nationalbibliothek.
The Deutsche Nationalbibliothek lists this publication in the Deutsche Nationalbibliografie; detailed bibliographic data are available in the Internet at http://dnb.d-nb.de.

Publisher and Distributor: Forschungszentrum Jülich GmbH
Zentralbibliothek
52425 Jülich
Tel: +49 2461 61-5368
Fax: +49 2461 61-6103
Email: zb-publikation@fz-juelich.de
www.fz-juelich.de/zb

Cover Design: Grafische Medien, Forschungszentrum Jülich GmbH

Printer: Grafische Medien, Forschungszentrum Jülich GmbH

Schriften des Forschungszentrums Jülich
Reihe Energie & Umwelt / Energy & Environment, Band / Volume 289

D 82 (Diss. RWTH Aachen University, 2015)

ISSN 1866-1793
ISBN 978-3-95806-094-4

The complete volume is freely available on the Internet on the Jülicher Open Access Server (JuSER) at www.fz-juelich.de/zb/openaccess.

Abstract

In this dissertation a direct methanol fuel cell stack model is described that resolves the electrochemical performance in individual cells, while having the capability to capture large scale effects across an entire stack through the use of a supercomputer. Typically stack sizes of 10 to 100 cells are modelled by dividing up cells into elements that are then distributed amongst the central processing units of the available cluster. The model contains thermal generation, polarisation losses in the bipolar plate, and gas expansion in the anode stream, modelled as a continuum.

Using this model a number of studies were undertaken: A parametric study looking at optimising reactant feed in which the methanol stoichiometry and concentration were varied, which also served also as a method of validation for the model against test data collected in parallel. The second study looks at fuel starvation, and what happens when one half of a cell in a stack experiences a reduction in feed stoichiometry and the impact across neighbouring cells in the stack. This highlighted critical effects that lead to smoothing of the anodic over-potential due to high in-plane conductivity of the bipolar plate, and cross-sectional current profiles that indicate bypassing of the under-feed region. The third study looks at the effect of water saturation on the cathode, and provides insight into the transition between non-critical to critical levels of water blockage in cathode gas diffusion layer, also highlighting the role that anode limiting current plays on the current density profile. The final section deals with the performance, scalability and convergence behaviour of the code, demonstrating the inherent flexibility and speed of such a method to create a holistic large-scale fuel cell model.

Kurzfassung

In dieser Dissertation wird eine Direkt-Methanol-Brennstoffzellen-Stack-Modell beschrieben, daß die elektrochemische Leistung in Zellen einer Brennstoffzellen-Stack löst, und die Fähigkeit hat, Großskaleneffekte über einen ganzen Stack zu erfassen. Dies wird durch den Einsatz von einem Supercomputer ermöglicht. Stackgrößen von 10 bis 100 Zellen werden typischerweise gelöst, durch das Aufteilen von Zellen in kleinere Elemente. Diese Elemente werden dann über den verfügbaren CPU der Cluster verteilt. Das Modell enthält Gleichungen für thermische Erzeugung, Polarisationsverluste in der Bipolar-Platte und Gasexpansion im Anodenstrom. Eine Reihe von Untersuchungen wurden durchgeführt: Die Erste ist eine parametrische Studie über die Optimierung der Edukteinspeisung in dem Stöchiometrie und Konzentration der Methanolfluß variiert wurde, und diente dazu als eine Validierung des Modells, in dem es gegen paralell gesamelte Testdaten vergliechen wurde. Die zweite Studie befasst sich mit Kraftstoffmangel im Falle eine verringerung der Stoichiometrie über eine Hälfte der Zelle in einem Stack, und die Auswirkungen auf die Nachbarzellen im Stack. Zwei kritischen Effekte sind vorgekommen, und zwar die Glättung der anodische Überpotential aufgrund der hohen Leitfähigkeit in der Bipolarplatte. Der zweite Effekt ist in die Querschnittsprofile der Stom zu sehen, in dem es die unterversogtem Region umgeht, und führt zum Gradient im Stromprofile. Die dritte Studie untersucht die Wirkung von Wassersättigung auf der Kathode, und gibt einen Einblick in den Übergang zwischen unkritischen auf kritische Sättigung in der Kathodengasdiffusionsschicht, und der Einfluss das Grenzstromprofile der Anodenseite. Der letzte Abschnitt befasst sich mit der Leistung, Skalierbarkeit und Konvergenzverhalten des Codes, was die Flexibilität und Geschwindigkeit eines solchen Verfahren, zum groß, ganzheitlichen Brennstoffzellenmodell führt.

Contents

1 Fundamentals 13
1.1 The Methanol Economy 13
1.2 Fuel Cells 14
1.2.1 Chemistry 16
1.2.2 Materials and Construction 16
2 Challenges in DMFC Technology 18
2.1 Performance 18
2.1.1 Backing Layer 20
2.1.2 Catalyst Layer 24
2.1.3 Membrane 26
2.2 DMFC Durability 27
2.2.1 Critical Operating Regimes 28
2.2.2 Catalyst Degradation 28
2.3 Goals 31
2.3.1 Stack operation and optimisation 32
2.3.2 Non-standard operation: Disruption effects and their consequences . 32
3 Modelling of a fuel cell stack 33
3.1 Zero-dimensional (0D) model 33
3.1.1 Base Model 33
3.1.2 Key assumptions 37
3.2 Large—scale numerical model 39
3.2.1 Stack decomposition 39
3.2.2 Electric Model 40

3.2.3 Electrochemical model 41
3.2.4 Model for the flow in anode and cathode feed channels 42
3.3 Dimensionless system of equations 44
3.3.1 Heat transport model 44
3.4 Additional Elements for Modelling Failure Regimes 48
3.4.1 Feed Disruption 48
3.4.2 Partial cathode flooding 49
3.5 Summary 52
4 Code 54
4.1 Model Development 54
4.1.1 Model Control 54
4.1.2 Flexibility 55
4.1 Numerical Details 56
4.2 Poisson and Zero-In Solvers 56
4.3 Algorithm 57
4.3.1 Main Function 59
4.3.2 Temperature 60
4.3.3 Electric and Electrochemical Model 61
4.4 Communication and Scaling 62
4.5 Summary 65
5 Model Fitting 66
5.1 Typical Experimental Stack Variants and Constants 66
5.2 Electrochemical performance parameters: 0D 68
5.3 Fuel supply related parameters 70

5.4 Summary 73

6 Results 74

6.1 Model Fitting 74

6.1.1 Electrochemical performance parameters: 0D Tafel Coefficients and Exchange Current Density 74

6.1.2 Fuel supply related parameters 75

6.2 Temperature Distribution 80

6.3 Optimal Feed Parameters 84

6.3.1 Methanol Stoichiometry 84

6.3.2 Methanol Starting Concentration 85

6.3.3 Operational Envelopes 88

6.3.4 Minimum Concentration 90

6.4 Feed Disturbance 91

6.4.1 Minor Disturbance 91

6.4.2 Extreme Disturbance 93

6.5 Cathode Flooding 98

6.5.1 Non-critical disruption 99

6.5.2 Transition region 100

6.5.3 Critical disruption 108

6.6 Convergence 114

6.6.1 Normal Operation 114

6.6.2 Feed Disturbance 115

6.6.3 Cathode Flooding 118

7 Summary 121

8 Conclusions 124

9 References 126

Table 1.1 Table of western European alphabet symbols with their descriptions and units.

Symbol	Description	Unit
b^a	Anodic Tafel Slope	V
b^c	Cathodic Tafel Slope	V
c_m	Methanol molar concentration	mol l^{-1}
D_M	Membrane Methanol Diffusion Coefficient	m^2 s^{-1}
D_b	Backing Layer Methanol Diffusion Coefficient	m^2 s^{-1}
F	Faraday Constant	C mol^{-1}
h_p	BP Thickness	m
i_*^a	Anodic Exchange Current Density	A m^{-3}
i_*^c	Cathodic Exchange Current Density	A m^{-3}
J	Total Load Current	A m^{-2}
j	Local Current	A m^{-2}

$\hat{j}$	Scaled Local Current density	
j_{cross}	Cross-over Current density	A m^{-2}
j_{lim}	Limiting Current density	A m^{-2}
k	CO_2 Bubble Acceleration Parameter	
L_c	Channel Length	m
l_m	Membrane Thickness	m
l_b	Backing Layer Thickness	m
R	BP Resistance	Ω m
S	Cell Surface Area	m^2
T	Temperature	K
v	Flow velocity	m s^{-1}

Table 1.2 Table of Greek alphabet symbols with their descriptions and units.

Symbol	Description	Unit
β	Cross-over Parameter	
β_*	Dimensionless Cross-over Parameter	
ε	Newman's Reaction Penetration Depth	
η	Overpotential	V
η_{act}	Activation Overpotential	V
λ^a	Methanol Stoichiometry	
λ^c	Air Stoichiometry	
σ_p	BP Conductivity	S m^{-1}
σ_t	Catalyst layer Conductivity	S m^{-1}

1 Fundamentals

Modern life requires a lot of energy to support all the technology that we surround ourselves with. Generation of this energy has, up till now, mostly been undertaken following the centralized generation principle, where large power stations provide electricity for a region. This means that energy needs to be transported over long distances to reach its point of use, and has efficiency losses associated with it. This combined with the desire to reduce our reliance on fossil fuels, has spawned research into numerous different clean or highly efficient energy generating technologies, such as wind or solar power, which provide local generation capacity, commonly referred to as decentralised energy generation. Transport and storage of this energy still remains a key issue, and one highly interesting proposal is to use hydrogen or its derivatives as a chemical store, thus allowing significant improvements to efficiency in transport and storage while also allowing exploitation of renewable sources to a greater extent.

1.1 The Methanol Economy

Alcohol fuels are well known, and have been in use right since the invention of the internal combustion engine [1]. Methanol has a high energy density, and is relatively clean burning due to a higher ratio of Hydrogen to Carbon molecules – 4:1. Methanol can be synthesised through various pathways, the two most common being bio-methanol from agricultural feedstock, or from Syn-gas generated from natural gas using Fischer-Tropsch synthesis [2].

Methanol has similar storage requirements to petroleum fuels – it is liquid up to 65 °C at ambient pressure, and has similar safety and handling requirement. It is advantageous compared to hydrogen fuels where the distribution has its own technical challenges. Hydrogen storage in liquid form requires temperatures lower than -253 °C , and the associated cryogenic processing to get it into liquid state, while gas storage brings with it

challenges in the construction of sturdy pressure vessels. There are a myriad of finer technical challenges and details covering all the aspects of a hydrogen based energy economy, which are dealt with elsewhere [3-5]. Methanol provides an option that is not dissimilar from current fuels, and would not require the more radical shift necessary for proposed hydrogen economy models. It is even proposed as a bridging as well as complementary technology; firstly allowing a more gentle transition to clean energy technologies; secondly, in combination with hydrogen, providing a synthesis route that uses CO_2 as a feedstock [6].

Fuel cells are a supporting technology within both the hydrogen and methanol economy concept. They facilitate highly efficient decentralised power generation, while taking hydrogen, or hydrogen derivatives like methane or methanol, directly as a feedstock.

1.2 Fuel Cells

Fuel cells operate by converting chemical energy into electricity and heat. This is achieved through direct electro-chemical conversion - a process that has an inherently high efficiency. There are three components that are fundamental to fuel cell construction (Figure 1.1): These are an anodic electrode, a cathodic electrode, where the reaction takes place and an ionic conductive electrolyte that separates both. Fuel cells operate with a continuous feed of reactants, and so additionally require flow fields which distribute reactants over the anode and cathode. Continuous fuel streams consisting of fuel and oxidising agent (usually O_2 from air) are fed to a cell into the anode and cathode respectively. The distinction of anode or cathode is derived from the electro-chemical half-cell reaction that takes place there. The electrolyte, a polymer membrane is sandwiched between the anode and cathode, separating them, and isolating against electrical contact of electron conducting phases. The membrane allows transport of the ion that couples the two half-cell reactions together, while electrons are conducted through an external electrical circuit. A catalyst is necessary to assist conversion, and allow reasonable rates of conversion. Thus, conversion of a fuel cell takes

place at the interface of several phases: A catalyst phase, a chemical fuel phase, an electron conducting phase and an ion conducting phase.

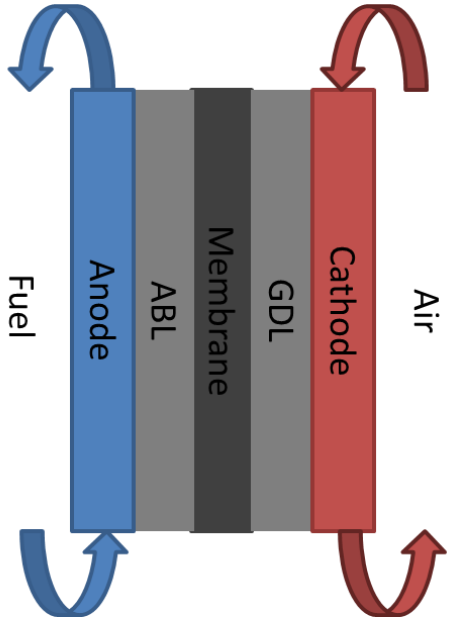

Figure 1.1: Schematic of a fuel cell with anode (left), separated from the cathode (right) by a membrane in to middle.

The design of a fuel cell electrode is based around maximising this four-phase interface, in order to maximise effective conversion area within the cell, and reduce wasted surface of costly materials like catalyst. Membrane materials are also of intense interest, as membranes are usually not 100 % selective for the desired ion, and secondary transport effects lead to losses in efficiency [7].

Fuel cells are a very interesting technology for providing high efficiency decentralized power generation for applications requiring between 0.1 to 200 kW [8]. Different types of cells have different operating ranges, with some types lending themselves to larger applications; studies have shown that DMFC is commercially viable under 1 kW [9]. The number of potential applications is as diverse as the various different types of fuel cells, and each fuel cell type has its own specific advantages and requirements that need to be

adapted to the application. This work is concerned with one specific type of fuel cell, namely the direct methanol fuel cell (DMFC), which uses a methanol-water solution as fuel and air as oxidant.

1.2.1 Chemistry

Direct methanol fuel cells (DMFCs), as the name suggests, use methanol as a fuel, which is fed to the anode, while air is fed to the cathode. The conversion process occurring inside a DMFC is broken down into half-cell reactions, defined by which side of the cell they occur on. The anodic half-cell reaction, seen below in equation (1.1), shows the conversion of methanol into carbon dioxide, protons and electrons via the methanol oxidation reaction (MOR). The cathodic half-cell reaction (equation (1.2)) is a typical oxygen reduction reaction (ORR).

$$CH_3OH + H_2O \longrightarrow CO_2 + 6H^+ + 6e^- \tag{1.1}$$

$$6H^+ + 6e^- + \frac{3}{2}O_2 \longrightarrow 3H_2O \tag{1.2}$$

A proton exchange membrane (PEM) is used to separate anode and cathode, and conducts protons from the anodic half-cell reaction to the cathodic half-cell reaction, thus coupling them into the reaction shown below in equation (1.3) [7].

$$CH_3OH + H_2O + \frac{3}{2}O_2 \longrightarrow CO_2 + 3H_2O \tag{1.3}$$

1.2.2 Materials and Construction

DMFC is composed of multiple layers, with each layer providing certain functionality. In the centre of the cell is a membrane which allows proton transport. The membrane is sandwiched on either side by the electrodes. These are composed of catalyst layer and backing layer. As the name suggests the catalyst layer contains a precious metal catalyst, usually an alloy of Platinum and Ruthenium. The job of the anode backing layer is to

homogenize methanol—water supply over the cell surface, to provide an electron conductive phase, while allowing fuel to diffuse to the catalyst layer. Similarly, on the cathode side where the GDL allows air to diffuse to catalyst sites, and allows product water to diffuse away into the air channel. This entire unit is referred to as a membrane electrode assembly (MEA). An MEA is sandwiched in between two flow-fields. The flow-fields have channels that supply the cell with methanol and air. These are sealed on either side by bi-polar plates, which are electrically conductive. The conversion process within a DMFC occurs at the interface of four phases: reactant and catalyst phases, as well as electron and proton transport phases. Because of this, construction of a cell has to maximize this interfacial area, meaning that the material structures have to be optimized on the micro-scale. This also means that there are processes that occur over a range of scales. Generally, attempts to model cell operation have to deal with characteristic lengths for processes spanning six to eight orders of magnitude [7].

2 Challenges in DMFC Technology

Cells are combined together into a stack, so called because they are stacks of cells. Stack lifetime is the single greatest issue affecting DMFC commercial viability [10]. Achieving lifetimes of above a few thousand hours, is only possible by understanding the physics behind DMFC operation, and modelling work provides useful insights into how to increase this life expectancy. DMFCs operate under intricate regimes of heat and mass transfer, and rely on the use of multiple types of materials working in concert in order to function. Any number of things in this complex and delicate balance can break down leading to reduced performance or even catastrophic failure. Generally these problems can be divided into two brackets: performance and durability.

2.1 Performance

Cell performance is concerned broadly with the parameters that affect the voltage and power output of a cell or stack. Additionally, fuel and system efficiency also factor in to the assessment of performance, all of which are impacted by cell construction and the quality and geometry of components, as well as operating conditions. Fuel efficiency can be calculated as actual power production over maximal power produced by an ideal cell without losses – with V^0 being the reversible cell voltage:

$$\eta^{cell} = \frac{J^{cell} V^{cell}}{J^{fuel} V^0}$$

Where J^{cell} is cell current, V^{cell} is cell voltage, and J^{fuel} is fuel consumption converted to current units using the Faraday equation. System efficiency incorporates all peripheral equipment – pumps, heat exchangers, etc. – and efficiency is calculated using system output divided by equivalent fuel consumption in terms of chemical energy usage, again from the Faraday equation:

$$\eta^{sys} = \frac{J^{sys} V^{sys}}{J^{fuel} V^{0}}$$

Where η^{sys} is system efficiency, J^{sys} is total current provided by the system, V^{sys} is system voltage, and J^{fuel} is fuel consumption as a current from the Faraday equation.

In this section details of the principle components in a DMFC are given with the issues affecting their function, and the effect of these issues on performance. A useful metric for determining cell and stack performance are polarisation curves. Polarisation curves represents cell voltage plotted against cell current. Figure 2.1 shows a typical polarisation curve for a DMFC. The curve is divided into three parts: Activation, resistive and mass transport limited regions. The activation is the region from zero current to 50 mA cm^{-2}. Cell voltage drops sharply from open circuit voltage (OCV) at zero current as reaction activation on either side of the cell causes potential losses. The resistive region is linear and is where ohmic losses are the dominant effect visible (typically between 100 – 300 mA cm^{-2} in DMFC operating with high fuel stoichiometry and feed concentration of 1 M methanol solution); hence the linear drop in voltage with increasing current. The mass transport limited region is where diffusion of reactants through their respective diffusion media becomes the critical feature affecting potential losses. This manifests as an exponential increase in potential losses, and a corresponding downward drop in the polarisation curve eventually ending when cell voltage becomes zero; this point is referred to as cell limiting current.

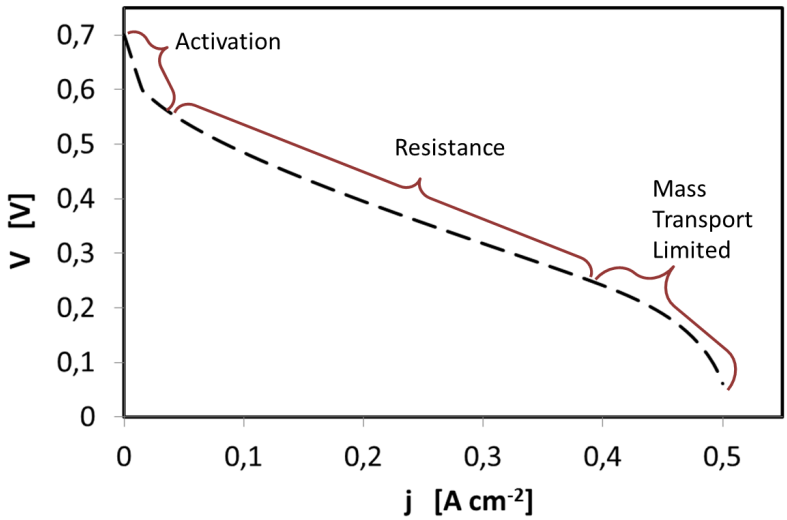

Figure 2.1: Schematic of a DMFC polarisation curve. Here the resistive region is between 50 – 400 mA cm^{-2} with the activation region to the left of it between 0 – 50 mA cm^{-2}, and the mass transport limited region to the right, above 400 mA cm^{-2}.

The regions defined in curve in Figure 2.1 are characterised by potential losses in all the functional layers, with specific effects contributing more significance depending on the operating regime. To illustrate the nature of these losses, in the following sections we consider these layers separately.

2.1.1 Backing Layer

The backing layer is responsible for transporting reactants to and from the reaction layer. The diffusion media must allow for transport of methanol or air to the respective electrode, but it must also allow for proper removal of reaction products, water and CO_2 otherwise the cell runs to risk of flooding or delamination.

Anode

The anode backing layer has to balance two important functions: High electric conductivity, and fast transport of liquid reactants to, and gaseous products from, the catalyst

layer. One particular design consideration is what type material is used. Different materials exhibit different characteristics when clamped under pressure within the cell. Electronic resistivity is reduced if compressive force is increased while permeability, and therefore reactant mass transport, is reduced by it [11].

The hydrophobicity of the backing layer has a significant impact on its mass transport properties. Backing layers are often treated with PTFE in order to improve gas transport, and it is postulated that this has a significant effect on cell performance [12]. Gas removal is a very important function of the anode backing layer. Carbon dioxide forms discreet slugs of gas in the anode backing layer, which then bubble into the anode feed channel. Because the bubbles form a continuous gas phase, they have a significant effect on methanol diffusion. The diffusion coefficient of methanol in CO_2 is three orders of magnitude larger than in water, while the methanol concentration in the gas phase is about three orders of magnitude lower than in the liquid phase; the product of gaseous methanol concentration by diffusivity is in the same order of magnitude, as for the liquid methanol [12-15]. If backing layers are treated with Teflon, in order to increase hydrophobicity, this can lead to a decrease in the effective transport coefficient [16]. A decrease in hydrophobicity (increase hydrophilicity) is achieved by adding Nafion ionomer to the anode backing layer

Cathode

On the cathode side removal of product water has a significant impact on cell performance and is the topic of much investigation. Electro-osmotic and hydraulic flux of water from the anode side sums with the water generated in the oxygen reduction reaction (ORR), resulting in a large level of liquid water saturation, s, in the cathode (volume fraction of liquid water in the cathode) [17, 18].

The key parameters governing the level of s in the cathode are cell current, temperature, amount of water vapour and velocity of air flow in the channel. The current determine the amount of water produced, the temperature and water vapour pressure

control the direction of water phase transition, while the air flow velocity regulates the rate of water removal from the cell.

The condensation of water in the cathode leads to significant reductions in oxygen diffusivity. By increasing air flow velocity, it is possible to reduce or even prevent water condensation. However this means that more energy is spent for air pumping and more water is removed from the stack, and the stack would no longer operate with a closed water cycle and require water re-filling, while heat management and operating temperature are also effected. This would add a level of complexity to operational maintenance that is considered unacceptable for commercial applications. It is therefore preferable to operate the stack with a low air flow rate, and gain a better understanding of the effect of liquid water on stack operation to mitigate the negative effects that it brings [19].

During normal operation air travelling along the cathode channel becomes saturated with water. This water comes from two sources: Water produced in the oxygen reduction reaction (ORR) running in cathode catalyst layer (CCL) of a DMFC and water transported by the electro-osmotic drag from the anode [20]. At the point where the air in the channel becomes fully saturated ($s = 1$) a liquid water front forms, where water condenses out. The presence of liquid water in the channel manifests severe flooding of the cathode backing layer (GDL), which significantly reduces the oxygen diffusivity through the GDL. This disruption to the oxygen transport to the catalyst sites has a strong effect on current production within the cell, leading to higher transport losses and lower limiting current. The disruption starts causing strong cross-currents within the cell, and eventually leads to partial cell reversal [21, 22].

State-of-the-art multi-dimensional CFD modelling of single DMFCs nicely capture the two-phase transport processes within the cell on the anode side [13, 14, 23]. The presence of water on the cathode has a profound effect on membrane water transport [24], and water management in the cathode is critical to optimal cell performance [25]. The GDL water saturation profile along the channel is difficult to model. Work has been done on modelling liquid water transport in a PEM fuel cell gas-diffusion layer (GDL) to find current-dependent water saturation at the GDL/microporous layer interface from the GDL water contact angle, GDL thickness porosity and permeability [26], [27]. Two-phase flow properties of the GDL such as the capillary pressure and the permeability of the porous media greatly affect the liquid water transport rate and the level of liquid saturation in the GDL [21, 28].

Water saturation lowers the effective oxygen diffusivity D_{Ox}^{x} in the GDL as follows [29]

$$D_{Ox}^{x} = D_{Ox}^{dry}\left(1-s\right)^{n} \tag{1}$$

Here D_{Ox}^{dry} is the oxygen diffusivity in the dry GDL and the exponent *n* is an empirical parameter that has a value between 1 and 3. This parameter is dependent on GDL properties, such as porosity or hydrophobicity. Determining *n* is nontrivial, and the dependence of oxygen diffusivity on saturation is the topic of on-going research.

In the literature, the mechanisms that regulate water transport in DMFC are not fully consolidated and limited effort has been dedicated to analyse flooding onset of the GDL and its consequences on DMFC operation [30]. In this work (Section 3.4.2) a simple Fick's model for oxygen diffusion in the GDL is used with the parameterisation of D_{Ox}^{x} above to get an idea of cell performance under conditions where the GDL is flooded. Flooding is modelled as a step change in the liquid saturation *s* along the channel.

2.1.2 Catalyst Layer

The catalyst layer is where the half-cell electrochemical reactions occur. Normally, catalyst materials are made from platinoid metals, with the most common DMFC catalysts being alloys of platinum and ruthenium on the anode side, and platinum on the cathode side. Performance is generally governed by three issues: Active catalytic area, feed molecules transport, and ionic conductivity [31-34]. These correspond to three of the four phases in the "four-phase boundary". With the electronic phase not represented, because of its inherent high conductivity meaning that it is not limiting factor [35]. Controlling catalyst layer characteristics is done by selecting various additives that affect the rheological properties of the catalyst layer, as well as catalyst loading.

Ionic Conductivity

Impedance measurements struggle to resolve ionic conductivities, because the resistance of the ionic phase is masked by the more conductive electronic phase, as well as by the capacitance effects of the electronic ionic interface [36]. However, Ionic conductivity does not have as significant an impact as crossover and catalyst loading [35]. It is also the case that electronic conductivity is roughly three orders of magnitude larger than ionic conductivity meaning BPP electronic conductivity has a far greater impact. That is to say, ionic (proton) conductivity is usually poor, due to high catalyst loading needed to minimize the activation losses [35, 37].

Catalyst loading

Active catalytic area is governed by catalyst loading [38, 39]. Intuitively, the more catalyst that is present, the more available reaction sites there are, and higher conversion fluxes are possible. Higher loadings are more expensive due to higher precious metal content, and cost optimization necessitates reducing the specific loading of catalyst within the CL. A major aspect in CL optimization is enhancing the utilization of the catalyst material; since this incurs a major fraction of the overall costs of the fuel cell system it is desirable to get as much out of it as possible [33, 40].

In the mid 90s *Murphy et al* report an optimal loading for polymer electrolyte fuel cells (PEMFC) of 5 mg cm^{-2} of platinum black [41]. Three years later *Ralph et al* report loadings of between 0.01 – 1.0 mg cm^{-2} of geometric electrode area [39]. As materials and production methods improved catalysts shifted from platinum black to carbon supported platinum [42], allowing for much greater true catalytic area, and in 2004 *Gasteiger et al* report a specific power density based on platinum loading of around 0.9–1.2 g_{Pt} kW^{-1} equating to a loading of between 0.6 – 0.8 mg_{Pt} cm^{-2} [38]. This is acceptable for stationary or uninterrupted power supply, but still too much for automotive applications which require a loading of under 0.4 g_{Pt} kW^{-1} to make them attractive for widespread use. Typical Pt/Ru loading in the modern anode catalyst layers for DMFC are between 0.1 – 2 mg cm^{-2} [43].

Reaction accessibility

While the anode takes liquid feed liquid and produces gas, the cathode is fed with gas phase reactant, but can produce liquid reactant if the thermodynamic conditions are conducive, which they are at normal operating conditions. Reaction accessibility is therefore a significant issue on the cathode side, where product water removal is critical to operation. Flooding in the GDL leads to water blocking the cathode CL and hindering the ORR. Depending on CL thickness the penetration depth of reactants is between 50-70 % of active layer thickness [41], which is significant for the electrochemical model later developed.

Nafion ionomer content has a crucial role in balance proton conductivity, catalyst utilization, and oxygen mass transport in the cathode catalyst layer (CCL). It has been shown that Nafion content does not have any great influence on the catalyst utilization and Tafel slope for the ORR in the range of 10 to 50 wt%, but has a significant impact on the pore structure as well as proton conduction. As Nafion content increases, the porosity of the catalyst layer is reduced and resistance to oxygen mass transport increases. It has been shown that cathodes containing 30 % by weight of Nafion exhibit the best performance in terms of power generation [44].

Lots of work has also been done by colleagues in *Forschungszentrum Jülich* on additives to the anode catalyst layer (ACL). The influence of a Fumion ionomer on the microstructure and thereby the electrochemical properties of both primary and secondary pores in DMFC anode catalyst layers have been extensively investigated. Ionomer phases formed by Fumion ionomers have a mean tortuosity about twice that of Nafion, which may be caused by a stronger tendency to form ionomer films in the catalyst layers. It is postulated that the ionomer has a film-forming ability that is lacking in Nafion, and is supported by several points: Decreased electrochemical active surface area (ECSA); poor connectivity between primary and secondary pores; pore blocking from ionomer [37]. This work shows how even significant improvements to material characteristics can lead to unwanted side effects in situ, and how delicate the balance of the 'four-phase boundary' can be even on the anode side, which is considered to be more straightforward from a mass transport perspective when compared to the CCL.

2.1.3 Membrane

Nafion membranes are the most common types to be implemented in DMFCs. Nafion membranes need to remain hydrated in order to maintain their proton conductivity, while in DMFCs this is not a problem with liquid water on the anode side. One of the most critical issues affecting DMFC operation is methanol cross-over, whereby methanol diffuses through the membrane from anode to cathode causing performance losses and a drop in fuel utilisation (and an associated drop in efficiency). Methanol concentration has a significant impact on parasitic permeation through the membrane, and leads to potential losses on both anode and cathode side [45]. Crossover is also affected by membrane thickness and methanol diffusivities in membrane and backing layer [46-49].

Typically, water permeates to the cathode through three mechanisms [50]: Diffusion, electro-osmotic drag and hydraulic permeation. The mechanisms can be differentiated by the driving forces involved in each; hydraulic permeation is driven by the

pressure gradient over the membrane, while electro-osmotic drag occurs due to water molecules' electro-static interaction with protons within the membrane. The water concentration is increased in the cathode CL due to the ORR, and water is transported out in the air stream. Generally, stacks lose water over time if they do not recycle condensate from the cathodic air stream. This is also an important aspect in the development of new membrane materials, as having a closed water cycle is imperative to making the technical application worthwhile against competing technologies. Experiments have shown that at low current densities water-crossover flux is dominated by diffusion. At high current densities the water flux due to the electro—osmotic effect increases significantly [46]. This means that the net water-transport increases with increasing current density.

It has been reported that cell operating temperature, oxygen flow rate and membrane thickness all have significant influences on water crossover. As expected, Water-crossover flux increases with temperature but decreases with increasing membrane thickness. High oxygen flow rates greatly increased the water-crossover flux through the membrane by increasing the concentration gradient of water through the cell [17, 46].

Reducing membrane thickness is of itself only important when considering specific conductivities, and diffusivities of the various reactants that pass through it, however it is considered particularly advantageous to reduce it for the purpose of minimising cell thickness, in order to increase specific power density [51].

2.2 DMFC Durability

The lifespan of a cell is very important for calculating the economic benefits of a DMFC system. Lifespan is determined by a performance degradation rate normally measured in mV h^{-1}, at a defined current density and other defined boundary conditions and a minimum performance requirement below which the system become uneconomical to run. Despite being easily measurable, there are many factors that influence this degradation rate, and it is difficult to quantify this from a theoretical point of view. Degradation in the function

of any sub-component, can lead to elevated performance losses, without any clear indication on a macroscopic level as to where the problem originates. Catalyst leaching is a major suspect, and Ruthenium dissolution is a topic of great interest [52-59].

2.2.1 Critical Operating Regimes

The rate of performance degradation is linked to the performance of the cell. High potential losses within the cell indicate critical regimes of operation, and this is linked to how much 'stress' the cell is under. Non-uniformity in cell performance, which leads to locally elevated overpotentials, can cause non-uniform ageing within a cell, causing it to become partially degraded – with part of its area experiencing a higher rate of degradation. It has been suggested that this leads to 'degradation waves' that spread out radially from points of high overpotential loss, eventually killing a cell's performance, as the area influenced increases [60, 61].

In real applications, individual cells are assembled into a stack. DMFC stacks are typically comprised of ten to a hundred cells connected in series. Cells can influence each other, and disturbances, visible in temperature or current production, penetrate through the stack often effecting neighbouring cells. A local resistive spot might be visible three cells away, and manifest as a depression of both temperature and local current and a localised increase in overpotential losses [61, 62]. Changes in the catalyst layer, such as agglomeration, can cause local changes in cell performance, and evince this effect.

2.2.2 Catalyst Degradation

Degradation of standard *Pt/C* cathode and *PtRu/C* anode catalysts is often severe and irreversible, and is known to occur by precious metal dissolution and agglomeration – specifically: Oswald ripening, crystal migration/coalescence, detachment from the support, and active site contamination. In addition, CLs suffer from carbon support corrosion [54, 56].

These detrimental processes lower the number of active catalyst sites [53]. With agglomeration the size of electro-catalytic particles increases with operation time (on the level of thousands of hours).

Current interrupt measurements, MeOH-stripping experiments and cyclic voltammetry measurements show that one reason for performance loss in degradation tests is the loss of catalyst activity inside the ACL and CCL due to dissolution and migration of Ruthenium. This is confirmed by EDX analysis CCL segments used in these degradation tests [59].

It has been suggested that ruthenium cross-over doesn't depend on methanol or water cross-over [63], but it becomes more significant closer to the methanol outlet [64]; suggesting that high anodic overpotentials are linked to high dissolution rates of ruthenium. It has been determined that dissolution increases by increasing: the upper potential limit in cyclic voltammetry experiment; acidity; oxygen partial pressure and by adding chloride ions. Ruthenium catalysts deteriorate by an order of magnitude more than the platinum catalyst, and carbon supported catalysts deteriorate by one order of magnitude more than the unsupported catalyst under the same conditions [57].

Attempts have been made to stabilize both catalyst layers. Work done on nitrogen doped catalyst showed that when normalized to ECSA, the N-doped *PtRu/C* exhibits superior methanol oxidation performance to undoped *PtRu/C* as well as commercially available *PtRu/C* of similar metal loading [58].

2.2.3 State of DMFC Modelling

Simple 2D models are well established in the arena DMFC modelling [23]. Generally, these come in two forms: numerical and analytical, with analytical models often dealing with non-Tafel kinetics [48, 65]. These models commonly deal with methanol concentration gradients, and methanol losses due to parasitic methanol permeation, with interest also

being paid to water transport on the cathode side [14, 18, 20, 24, 30]. Also of interest is the two-phase nature of the anode feed, and some models deal with this aspect [13, 66]. Dynamic models exist, but are simplified and deal only with a few sub-components due to complexity and computational requirements [67]. Due to the interest in methanol cross-over models address transport phenomena in the membrane [18, 24, 68] and regimes within anodic and cathodic catalyst layers [31, 33, 51, 69-72]. This thesis builds on work done which incorporates many of the aspects commonly dealt with in the area of DMFC modelling, and adding one significant aspect to it, namely resolving an entire stack in 3D [73, 74].

2.3 Goals

The aim of this work is to model aspects of a DMFC stack based on a novel approach to stack modelling. The model is primarily concerned with capturing large scale effects across a 100 cell DMFC stack (nominally within the 1 kW class), and to capture physical effects that come about due to interactions between the multiple cells that comprise the stack. A highly scalable and flexible modelling method is needed in order to allow modelling of different experimental stack variants, as well as capturing the essential physics of fuel cell stack operation.

This work formed part of a greater project to further develop DMFC technology by understanding ageing processes in greater detail. It has been suggested in literature that local defects in the cell act like tumours, which grow over time reducing cell performance of the surrounding area, and eventually leading to degradation over the entire cell area [60-62]. The goal of the modelling was to develop a DMFC stack simulation – one that is unique in its scale and scope. This model would need to resolve local micro-scale effects, but also weave these into a larger stack picture, thus providing insight into how local effects impact global performance.

The advantage of developing a large-scale simulation is the benefit of visualising what happens inside a stack that would be otherwise impossible, and the predictive ability that modelling provides for optimisation and further development. This thesis aims to lay out visualisations from several simulations undertaken with the model code, and provide guidelines for optimisation, where optimal operational envelopes are developed for parameters.

The approach provides a lot of freedom to choose specific simulation experiments. One aspect that cannot be neglected is model validation with experimental data, which provides relevance to further simulation studies. Local effects can manifest in a numerous different circumstances, and this work will deal with some of the most interesting operating regimes that are relevant to normal stack operation. Optimisation of the stack is of interest

to modellers as well as modelling of common faults that can occur during operation like disruptions to fuel supply

2.3.1 Stack operation and optimisation

The Stack model can be used to optimise stack operation and help experimentalists determines what performance and operating conditions occur for specific parameter sets. Extending this idea it is possible to then use the model to predict what will occur in a stack with altered parameters and predict its behaviour. The grander strategy then is to determine an optimal set of parameters tailored to specific applications. Because DMFC stack modelling is still in its infancy, it is the goal of this work to start to address the issue of stack optimisation.

By changing fuel supply parameters, like starting feed concentration, fuel stoichiometry; or altering material properties – for instance backing layer diffusivity – it is possible to build up a picture of an optimal set of values. These operational envelopes can then provide information for further application specific development.

2.3.2 Non-standard operation: Disruption effects and their consequences

The model allows us to explore local defects, and their effects on stack operation. Failures in the supply of fuel to the reaction zones within a cell lead to changes in the production of current, and local potential losses. This work aims to explore how these local changes effect stack performance.

3 Modelling of a fuel cell stack

The modelling work that has been undertaken is presented here in two stages. The first stage – the zero-dimensional model – shows how a simple analytical model for a DMFC polarisation curve provides a starting point for understanding the fundamental electrochemical processes that govern DMFC operation. This is then expanded upon in the second stage, which gives details of the full stack model. The full model that is then used to explore DMFC operation in the simulations, as detailed in the results chapter.

3.1 Zero-dimensional (0D) model

In literature, there is a misunderstanding with the term "zero-dimensional models". Typically, this term is used to denote a model, which represents an analytical expression for the cell polarization curve. However, analytical polarization curve can be obtained using either semi-empirical arguments, or as exact analytical solution to the conservation equations. In the latter case, a "0D model" is a result of solution of 1D or even 2D mass and charge conservation equations.

The model below employs analytical expressions for the half-cell polarization voltages (overpotentials) resulting from solution of a 1D, through-plane mass and charge transport problem in a DMFC. The model does not take into account variation of flow parameters along the channel. Nonetheless, the model is useful for an initial estimate of kinetic and transport parameters of DMFC, as discussed below.

3.1.1 Base Model

Local cell 6voltage V_{cell} is equal to OCV – V_{oc} – minus overpotential and ohmic losses:

$$V_{cell} = V_{oc} - \eta^a - \eta^c - Rj$$

(3.1)

Where η^a and η^c represent anodic and cathodic overpotentials respectively, *R* is cell resistivity, and *j* is local cell current.

A modified Perry-Newman-Cairns model extended to include transport losses was used to find the half-cell overpotentials [31, 34]. This model offers a good basis for describing half-cell polarizations, because it includes losses due to methanol crossover, activation, proton transport losses and losses due to feed molecules diffusion in the respective backing layer:

$$\frac{\eta^a}{b^a} = \operatorname{arcsinh}\left(\frac{\varepsilon_a^2}{2}\left(\beta_a^2 + \tilde{j}_a^2\right)\right) - \ln\left(1 - \frac{j}{j_{\lim}^a}\right) - \ln\left(1 + \beta_{cross}\right)$$

(3.2)

$$\frac{\eta^c}{b^c} = \operatorname{arcsinh}\left(\frac{\varepsilon_c^2}{2}\left(\beta_c^2 + \left(\tilde{j}_c + \tilde{j}_{cross}\right)^2\right)\right) - \ln\left(1 - \left(j + j_{cross}\right) / j_{\lim}^c\right)$$

(3.3)

Where b^a and b^c are Tafel slopes of the MOR and ORR respectively. β_a and β_c are calculated using the respective dimensionless electrode (subscript '*e*') current density according to:

$$\beta_e = \frac{\sqrt{2\tilde{j}_e}}{1 + \sqrt{1.12\tilde{j}_e} \cdot e^{\sqrt{2\tilde{j}_e}}} + \frac{\pi \tilde{j}_e}{2 + \tilde{j}_e}$$

(3.4)

where $j_e = j_a$ at the anode and $j_e = j_c + j_{cross}$ at the cathode.

The first terms in Eqs. (3.2) and (3.3) represent reaction activation overpotential including the voltage loss due to the proton transport in the catalyst layer. This leads to quite significant voltage losses due to electrode ionic resistance. It can be shown, that in the limit of small cell current, the first terms in Eqs. (3.2) and (3.3) reduce to the standard Tafel law, while at high currents these terms describe doubling of Tafel slope because of the poor proton transport in the CL [31].

The second terms in Eqs. (3.2) and (3.3) describe the voltage loss due to the feed molecules transport in the backing (gas-diffusion) layer. Note that the total current on the cathode side is a sum of useful and crossover currents. The last logarithm in Eq. (3.2) describes voltage loss due to lowering of methanol concentration on the anode side caused by methanol crossover. As the main mechanism of crossover is diffusion, this term is independent of cell current.

$\tilde{j}_e$ is non-dimensionalised using the respective normalizing current j_e^* for the electrode:

$$\tilde{j}_e = \frac{j}{j_e^*}$$

(3.5)

j_e^* Cross-over current is non-dimensionalised using cathodic normalizing current:

$$\tilde{j}_{cross} = \frac{j}{j_c^*}$$

(3.6)

Normalizing current is given by

$$j_e^* = \frac{\sigma_{ion} b^e}{l_t}$$

(3.7)

Where σ_{ion} is ionic conductivity, b^e is the Tafel slope for the respective electrode, and l_t is electrode thickness.

Parameter ε_e is the Newman's dimensionless reaction penetration depth:

$$\varepsilon_e = \sqrt{\frac{\sigma_{ion} b^e}{2 i_e^* l_t^2}}$$

(3.8)

Here i_e^* is the volumetric exchange current density (A m^{-3}) for the respective electrode.

Equivalent current density of methanol cross-over current is given by

$$j_{cross} = \beta_{cross}^* \left(j_{\lim}^a - j \right)$$

(3.9)

Where β_{cross}^* is cross-over parameter which determines the rate of crossover through the membrane:

$$\beta_{cross}^* = \frac{\beta_{cross}}{1 + \beta_{cross}}$$

(3.10)

and

$$\beta_{cross} = \frac{\overline{D}_m l_b^a}{\overline{D}_{MeOH}^a l_m}$$

(3.11)

Is a ratio of methanol mass transfer coefficients in membrane and in the anode backing layer. Here $\overline{D}_m$ is the methanol diffusion coefficient in membrane of a thickness l_m, and $\overline{D}^a_{MeOH}$ is the methanol diffusion coefficient in the anode backing layer of a thickness l^a_b.

Limiting currents are proscribed by the maximum mass flux transferable through the BL / GDL:

$$j^a_{\lim} = \frac{6F\bar{D}^a_{MeOH}\bar{C}_{MeOH}}{l^a_b} \quad (3.12)$$

$$j^c_{\lim} = \frac{4F\bar{D}^c_{Ox}\bar{C}_{Ox}}{l^c_b} \quad (3.13)$$

Where *F* is the Faraday constant, $\bar{D}^a_b$ and $\bar{D}^c_b$ are the methanol and oxygen diffusion coefficients in the BL/GDL averaged over the cell surface, l^a_b and l^c_b are the thickness of the anode BL and cathode GDL respectively and $\bar{C}_{MeOH}$ and $\bar{C}_{Ox}$ are the average concentrations of methanol and oxygen respectively.

3.1.2 Key assumptions

It is important to note that the variation of the feed and oxygen concentration along the channel, including two-phase effects on the anode side, are not taken into account in the 0D model. This assumption can only be justified at high fuel and oxygen stoichiometries (high lambda), where due to reactant excess the concentration variation along the channel is minimal.

This model also neglects changes to diffusion characteristics in both anode BL and cathode GDL. On the anode side the presence of CO_2 bubbles alter methanol diffusion

properties of the BL, while on the cathode side, condensation of water leads to a reduction of oxygen diffusivity in the GDL. Again these issues can be mitigated by high reactant velocities (high lambda). For this reason the notation $\bar{D}_r$ and $\bar{C}_r$ has been used to describe average diffusion coefficients and concentrations of '*r*' reactants. These assumptions provide a solid model of point performance in the cell, and form the core of the electrochemical model.

The model has been used for comparison with the experimental polarization curves (Section 5). Fitting the model to the measured curves allowed us to estimate the basic transport and kinetic parameters of the cell. These parameters were then used in large-scale numerical calculations.

3.2 Large—scale numerical model

3.2.1 Stack decomposition

A large—scale numerical model is based on a following idea. The stack is decomposed into a number of modules (cells); each module consists of a bipolar plate (BP) and adjacent MEA (Figure 3.1). In the bipolar plate, heat and current transport are described by 2D in-plane models, whereas in the MEA, heat, mass and charge transport are assumed to be in the through–plane direction only [74].

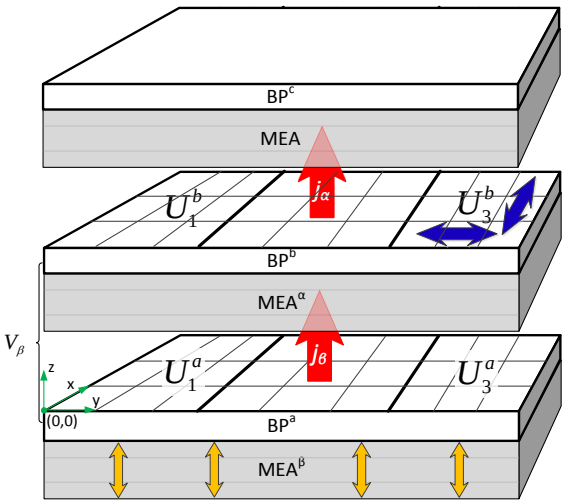

Figure 3.1: Stack schematic showing division of cell elements 'U_i'. FD approximations are indicated by yellow arrows, while red arrows show (axial) current. Blue arrows show in-plane effects that are calculated with the solvers.

Furthermore, each module is "cut" into elementary units U_i with single straight air and methanol channels (Figure 3.1). These units form building blocks for the parallel model implementation: the number of units in a stack equals the number of CPUs required. This gives flexibility to scale–up the model to 100–cell stacks by using several thousand CPU cores, practically without increasing the wall–clock time for calculations.

3.2.2 Electric Model

Local non-uniformities in a cell can cause in-plane currents in the bipolar plate. To model this cell coupling, the in-plane variation of bipolar plate potential has to be taken into account.

Generally, the distribution of voltage over the BP volume is described by a 3D Laplace equation. However, in a fuel cell stack, the thickness of the BP is two orders of magnitude smaller, than the in–plane size. This allows us to approximate the axial (z–) derivative in Laplace equation by the difference of local normal currents j_α and j_β coming in and out of the BP (Figure 5.1). This reduces a 3D Laplace problem to a 2D Poisson equation [75, 76]

$$\frac{\partial^2 V}{\partial x^2} + \frac{\partial^2 V}{\partial y^2} = \frac{j_\alpha - j_\beta}{\sigma_p h_p} \tag{3.14}$$

where σ_p is the BP electric conductivity, and h_p thickness. Note that BP voltage is calculated with respect to the point with zero coordinates on each BP, i.e., V represents the relative variation of BP potential (Figure 5.1).

Voltage of cell β clamped between the two BPs a and b is

$$V_\beta = V_\beta^{(0,0)} + V_a - V_b \tag{3.15}$$

where $V_\beta^{(0,0)}$ is the voltage drop between the points with coordinates $(0,0)$ on BPs a and b (Figure 5.1). Note that the Latin letters a, b,... enumerate BPs, while Greek letters α, β,... enumerate cells.

On the other hand, cell voltage is OCV V_{oc} (assumed to be the same for all cells) minus internal voltage losses inside the cell:

$$V_\beta = V_{oc} - \eta^a - \eta^c - Rj \tag{3.16}$$

where η^a, η^c are the anode and the cathode half–cell overpotentials and R accumulates the membrane and contact resistances. Equating (3.15) and (3.16), and rearranging terms we get

$$V_a - V_b + V_\beta^{loss} = V_{oc} - V_\beta^{(0,0)} \tag{3.17}$$

where

$$V_\beta^{loss} \equiv \eta^a + \eta^c + Rj \tag{3.18}$$

is the total voltage loss in the cell β. Note that the right side of Eq.(3.17) is independent of coordinates.

The total current through each cell in the stack is the same, i.e.

$$\int_S j\, dS = JS \tag{3.19}$$

where S is the cell active area and J is the mean current density. Multiplying (3.17) by j and integrating over S, we get

$$V_\beta^{(0,0)} = V_{oc} - \frac{1}{JS}\int_S \left(V_a - V_b + V_\beta^{loss}\right) j\, dS \tag{3.20}$$

This equation was used to determine $V_\beta^{(0,0)}$.

3.2.3 Electrochemical model

The anode and the cathode half–cell overpotentials η^a and η^c, respectively, are given by [66]

$$\frac{\eta^a}{b^a} = \operatorname{arcsinh}\left(\frac{\varepsilon_a^2}{2}\left(\beta_a^2 + \tilde{j}^2\right)\right) - \ln\left(1 - \frac{j}{j_{\lim}^a}\right) + \ln(1+\beta) \tag{3.21}$$

$$\frac{\eta^c}{b^c} = \operatorname{arcsinh}\left(\frac{\varepsilon_c^2}{2}\left(\beta_c^2 + \left(\tilde{j} + \tilde{j}_{cross}\right)^2\right)\right) - \ln\left(1 - \frac{(j + j_{cross})}{j_{\lim}^c}\right) \tag{3.22}$$

which are the same as in section 3.1, except that these now describe local overpotential due to changing feed conditions within the cell. Crossover (Eq. 3.9), crossover beta parameter (Eq. 3.10) and limiting currents (Eq. 3.12 & 3.13) remain the same as depicted in section 3.1.

The diffusion coefficient for methanol through the backing layer is taken from experimental data, with Arrhenius exponential factors from [77, 78]($m^2\ s^{-1}$):

$$D_b^a = 2.173 \cdot 10^{-9} \exp\left(2436\left(\frac{1}{343} - \frac{1}{T}\right)\right) \tag{3.23}$$

The following equations (3.24) and (3.25) were used to account for the Arrhenius dependence of exchange current density on temperature ($A\ m^{-3}$):

$$i_*^a = \frac{94.25}{l_t} \exp\left(\frac{35570}{8.314}\left(\frac{1}{353} - \frac{1}{T}\right)\right) \tag{3.24}$$

$$i_*^c = \frac{0.394}{l_t} \exp\left(\frac{73200}{8.314}\left(\frac{1}{343} - \frac{1}{T}\right)\right) \tag{3.25}$$

where l_t is the catalyst layer thickness. An anodic reference current of 942.5 mA cm^{-2} at 80°C, as well as Arrhenius exponents within both these equations are taken from [14], with reference temperatures of 353 K and 343 K respectively [14]. Cathodic reference exchange current density was fitted using our experimental data.

3.2.4 Model for the flow in anode and cathode feed channels

Carbon dioxide bubbles are produced by the MOR and these are swept along in the anode channel with the feed stream. The anode stream is modelled as a uniform phase with

physical properties being the average of liquid and gas phases. Mass conservation in the anode channel reads

$$\frac{\partial\left(v^a c_m\right)}{\partial x} = -\frac{\left(j + j_{cross}\right)}{6Fh^a} \tag{3.26}$$

where v^a is the anode flow velocity, c_m is the average local methanol molar concentration in the channel over two phases, and h^a is the anode channel height. Change in the methanol molar flux, $v^a c_m$, is due to methanol consumption by the local current j and the crossover current j_{cross}.

A simple mass balance equation for CO_2 produced in the reaction leads to the equation for the flow velocity [66, 79]

$$6Fh^a c_m^0 J \frac{\partial v^a}{\partial x} = kj \tag{3.27}$$

Physically, CO_2 bubbles dramatically accelerate the flow, with the rate of velocity growth being proportional to the local current density. In equation (3.27), k is a model parameter which determines the degree of flow acceleration [66, 79]. Note that only a useful current contributes to the bubbles production; crossover current does not appear in Eq.(3.27) as it generates CO_2 on the cathode side.

Oxygen concentration c_{ox} is modelled as an exponential decay along the cathode channel [80]

$$c_{ox}(x) = c_{ox}^0 \exp\left(\frac{x}{L}\ln\left(1 - \frac{1}{\lambda^c}\right)\right) \tag{3.28}$$

where λ^c is oxygen stoichiometry, L is the channel length and c_{ox}^0 is the inlet oxygen concentration. This equation models the decay of oxygen concentration along the cathode air channel parametrically.

3.3 Dimensionless system of equations

Variables are non-dimensionalised to simplify and parametrise equations, delivering values which give an indication of intrinsic properties, and is common practice when dealing with systems governed by differential equations. The system of equations discussed above was non–dimensionalised using the following variables

$$\tilde{x} = \frac{x}{L}, \quad \tilde{y} = \frac{y}{L}, \quad \tilde{\eta} = \frac{\eta}{b^c}, \quad \tilde{j} = \frac{j}{j_{\lim}^{a0}}, \quad \tilde{v} = \frac{v}{v^0}, \quad \tilde{c} = \frac{c}{c^0} \tag{3.29}$$

where the superscript 0 marks the inlet values and $j_{\lim}^{a0}$ is given by Eq.(3.12) with $c_m = c_m^0$, inlet methanol concentration. The resulting system of equations is listed in Table 1. Overall, the model takes into account MOR and ORR reaction overpotentials, voltage losses due to methanol and oxygen mass transport in the backing layers, due to methanol transport in the channels and voltage loss due to in—plane currents in bipolar plates.

3.3.1 Heat transport model

Heat balance in a fuel cell is determined by the heat released in the electrochemical and chemical reactions occurring in the electrodes, heating or cooling from neighbouring cells, and by cooling due to water evaporation. Temperature distribution in the stack volume is governed by a 3D Laplace equation

$$\lambda_{\parallel}\left(\frac{\partial^2 T}{\partial x^2} + \frac{\partial^2 T}{\partial y^2}\right) + \lambda_{\perp}\frac{\partial^2 T}{\partial z^2} = \nabla \cdot \vec{q} \tag{3.30}$$

where $\lambda_{\parallel}$ and $\lambda_{\perp}$ are the stack thermal conductivities in the xy–plane and along the stack axis z, respectively, and $\vec{q}$ is the sum of all source and sink heat fluxes. By analogy to the electric model, due to the large facial area of BPs as compared to their thickness, Eq.(3.30) can be reduced to the 2D Poisson equation:

$$\lambda_{\parallel}\left(\frac{\partial^2 T_n}{\partial x^2}+\frac{\partial^2 T_n}{\partial y^2}\right)=\frac{q_\alpha - q_\beta}{h_z}-\frac{\lambda_\perp}{h_z^2}\left(T_{n+1}-2T_n+T_{n-1}\right) \tag{3.31}$$

where q_α, q_β are the heat fluxes from the cells α and β, respectively, h_z is the sum of BP and MEA thicknesses, and T_n the temperature of the n^{th} BP. The last term on the right side of Eq.(3.31) approximates the second derivative along the stack axis in Eq.(3.30).

Sources of heat represented by the q terms take into account heat produced by the useful and parasitic (on the cathode side) electrochemical reactions. The major sink term in the equation is water evaporation (see below).

It is convenient to introduce dimensionless temperature and pressure

$$\tilde{T}=\frac{T}{T_{298}},\quad \tilde{p}=\frac{p}{p_{atm}} \tag{3.32}$$

where T_{298} and p_{atm} are the standard temperature and pressure. Collecting terms and using non–dimensional variables, the heat transport equation takes the form

$$\frac{\partial^2 \tilde{T}_n}{\partial \tilde{x}^2}+\frac{\partial^2 \tilde{T}_n}{\partial \tilde{y}^2}=-\left(\tilde{q}^c-\tilde{q}^a\right)+\psi_w^2\left(\tilde{p}_w^{sat}-\tilde{p}_w\right)-\frac{\lambda_\perp L^2}{\lambda_{\parallel} h_z^2}\left(\tilde{T}_{n+1}-2\tilde{T}_n+\tilde{T}_{n-1}\right) \tag{3.33}$$

where $\tilde{q}^c$ is the heat flux from the cathode side of the $(n+1)$ th MEA, $\tilde{q}^a$ is the heat flux from the anode side of the n th MEA, and the term with ψ_w^2 describes the cooling due to liquid water evaporation. Here $p_w^{sat}(T_n)$ is the pressure of saturated water vapour at a temperature T_n.

The heat flux pervading n th BP from the cathode side of the $(n+1)$ th MEA is given by

$$\tilde{q}^c=\left(\omega^2\tilde{T}_n+\varphi^2\tilde{\eta}^c\right)\tilde{j}+\omega_{cross}^2\tilde{T}_n\tilde{j}_{cross} \tag{3.34}$$

The first term on the right side of Eq.(3.34) represents thermodynamic and irreversible heating in the useful electrochemical reaction, the second term describes heating in the parasitic methanol–oxygen reaction. A similar equation, though without the crossover term represents q_n^a, the heat flux from the anode of the nth MEA. The dimensionless parameters ω, ω_{cross}, φ and ψ_w are given in Table 3.1.

Table 3.1: Dimensionless coefficients for heat transfer model equations – Eq. (3.26) and (3.27).

Water Evaporation	$\psi_w^2 = \dfrac{L^2 \Delta H_{evap} \cdot K_{evap} \left(\varepsilon_{BL}\ s\ \rho_s^0\right) p^*}{\lambda\ T^*\ M_w}$
Electrochemical Reaction	$\omega^2 = \dfrac{L^2 \Delta S\ j_{\lim}^{a0}}{\lambda\ 6\ F\ h_z}$
Crossover	$\omega_{cross}^2 = \dfrac{L^2 \Delta S_{cross}\ j_{\lim}^{a0}}{\lambda\ 6\ F\ h_z}$
Potential	$\varphi^2 = \dfrac{L^2 b_a j_{\lim}^{a0}}{\lambda\ T^*\ h_z}$

The boundary conditions for cell temperature are determined using free convective heat transfer. We have four vertical surfaces – two end plates and two sides, and one horizontal plane – the top surface of the stack. The bottom surface is taken as adiabatic, as the stack is considered perfectly insulated from free convective effects on its underside

(Figure 2). For both vertical and horizontal edges air is warmed, and rises due to buoyancy siphoning away heat.

The velocity of the cooling air as well as fluid properties are determined using Grashof, Prandtl and Rayleigh numbers. Heat flux is calculated at the cell walls based on empirically derived Churchill-Chu equations [25], from which the Nusselt number – Nu_L – is obtained, and from there the convective heat transfer coefficient – α – to the surroundings

$$a = \frac{Nu_L k_{air}}{L_{surf}} \tag{3.35}$$

where k_{air} is the thermal conductivity of air, and L_{surf} the characteristic length of the surface. For example, endplate temperature T_N is found by rearranging Eq. (3.36) to get T_N explicitly – Eq (3.37)

$$-\lambda_{\perp} \frac{\partial T}{\partial z} = \alpha \left(T_N - T_{amb} \right) \tag{3.36}$$

$$T_N = \frac{\lambda_{\perp} T_{N-1} + \alpha h_z T_{amb}}{\lambda_{\perp} + \alpha h_z} \tag{3.37}$$

where T_{N-1} is the temperature of the BP next to the endplate, and T_{amb} is the ambient temperature.

3.4 Additional Elements for Modelling Failure Regimes

In order to model special cases in which there is a failure in some aspect of the cell function additional model elements are activated in the stack model. This section deals with how two failure cases were modelled. Specifically, details are given on how a model for the disruption of methanol supply was implemented, and the second, a model for partial flooding of the cathode with product water.

3.4.1 Feed Disruption

Failure in methanol or oxygen supply leads to non–uniform distribution of local current over the cell surface. This non–uniformity induces in–plane currents in the bipolar plate and the respective gradient in the BP voltage V. Feed disturbances are modelled as a disruption to the feed stoichiometry of methanol (Figure 3.2). To study these regimes, the code was modified to allow for disparate flow rates over a pre-defined area of the cell. This could then be applied to either one, or several specific cells in the stack, allowing control over both the area and degree of feed disturbance applied.

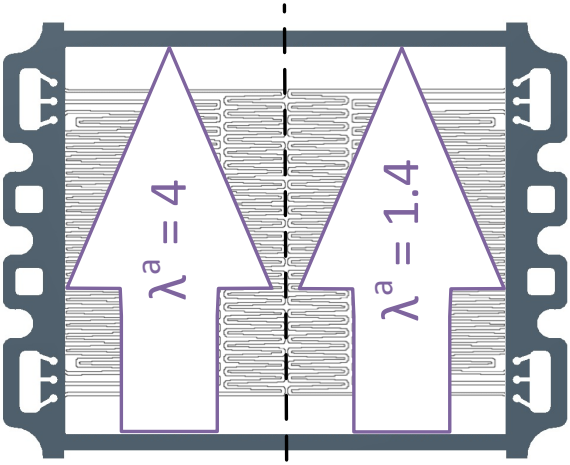

Figure 3.2: Schematic of feed disruption simulation showing a feed reduction over half the cell area; where methanol stoichiometry is reduced from 4 to 1.4.

3.4.2 Partial cathode flooding

Partial cathode flooding may hinder oxygen transport to the catalyst sites. Experiments show that in typical operating conditions, water is accumulated in the bottom part of the cell due to gravity forces. In each cell a condensation front forms below which the cathode is partly flooded (Figure 3.3).

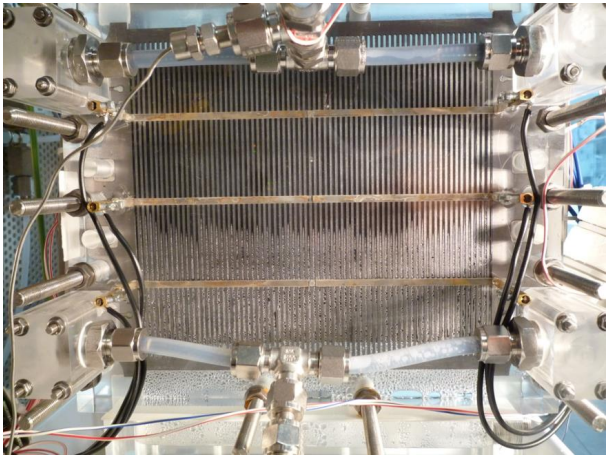

Figure 3.3: Image of cathode flooding in the GDL, showing distinct transition between dry, unsaturated region, and the flooded region of the cell in an experimental cell. This Plexiglas cell shows air saturated with water in the flow field, and indicates that the cathode GDL is also saturated.

The condensation front is modelled as a rapid change in the oxygen diffusion coefficient D_{Ox}^{x} in the cathode backing layer (GDL) as a stepwise *tanh*-function of distance *x* along the air channel:

$$D_{Ox}^{x} = \left((1-s)^{n} + \frac{\left(1-(1-s)^{n}\right)}{2}\left(1 + \tanh\left(\frac{x - x^{*}}{\sigma}\right)\right)\right) D_{Ox}^{dry} \qquad (3.38)$$

Here s is the liquid saturation of the flooded part of the GDL (see below), σ is the thickness of the transition region between flooded and non-flooded regions and x^{*} is the point at which the condensation front occurs. Eq.(3.38) models rapid, but smooth transition between the reference value of "dry" diffusion at the inlet of the air channel D_{Ox}^{dry}, and the reduced diffusivity of the flooded region $D_{Ox}^{fld} = D_{Ox}^{dry}(1-s)^{n}$. The width of the transition region is kept small (4% of the channel length) in order to mimic the steep front of the phase change of

water observed in experiments. We specify a flooding amplitude parameter which describes the ratio of flooded to "dry" oxygen diffusivities:

$$A_D = \frac{D_{Ox}^{fld}}{D_{Ox}^{dry}} \tag{3.39}$$

Eq.(3.38) is illustrated in Figure 3.4. Note that "dry" oxygen diffusivity includes the liquid saturation factor corresponding to the "dry" region, so that *s* represents the liquid saturation in the flooded part of the cell.

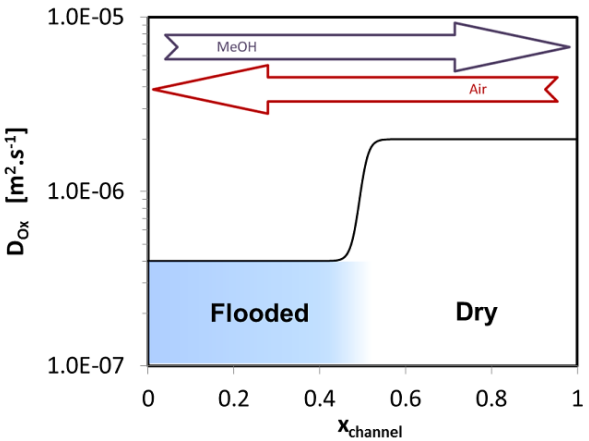

Figure 3.4: Schematic showing the variation of oxygen diffusivity in the cathode GDL along the channel. Partially flooded regime is modelled as a rapid but smooth transition between two different diffusivities – D_{Ox}^{dry} and D_{Ox}^{fld} – along the air channel. Reactant are in counter-flow, with the air inlet at x=1 and outlet at x=0.

Table 3.2: Table of parameters used to control the shape and effect of the condensation front model equation (Eq. 5.31).

Symbol	Description	Unit	Value
A_D	Flooding Amplitude Parameter	-	0 – 1

D_{Ox}^{dry}	Dry Oxygen Diffusion Coefficient in Cathode GDL	$m^2\ s^{-1}$	2×10^{-6}
x^*	Distance of the Midpoint of Condensation Front along the channel	-	0.5
σ	Half the Width of The Condensation Front	-	0.02

3.5 Summary

At first a simple model for overpotential losses is developed to account for basic operation of the fuel cell; it calculates the losses at a single point based on feed, geometric and electrochemical parameters. This is then used to calculate local overpotentials in the stack model, which includes concentration gradients along the cell active surface. The model consists of three main parts – thermal, electric and electrochemical sub-models. The thermal model includes:

- Heat Equation including terms for thermal sources and sinks – reaction, water vaporisation, etc.
- Boundary conditions for both vertical and horizontal surfaces based on free convection.
- Heat exchange with feed streams.

The electric model includes:

- BP voltage solver
- BP voltage boundary conditions

The electrochemical model includes local polarisation curve model with terms for losses from:

- Activation

- Diffusion
- Methanol cross-over

Additional equations are introduced to capture specific defects, specifically partial feed disruption and cathode flooding. These respectively model the case of partial feed disruption to the cell, and the occurrence of liquid water in the GDL, which reduces oxygen diffusivity.

4 Code

This section deals with how the simulation code is structured. The model is programmed in C++ using Message Passing Interface (MPI) for parallelisation. Modelling equations are formulated and implemented in modules of code that apply these with help of numerical solvers to find solutions to the domain variables. Details of how these modules interact are elucidated below.

4.1 Model Development

With the ubiquity of good scientific and engineering tools for modelling, it is perhaps surprising to decide to develop one's own modelling tool. Although commercial tools provide a springboard for developing a modelling platform, the physical and chemical models they utilize (the functions they employ to describe the change of variables) are often opaque to the user. This means that the user must either establish how these tools perform calculations or assume that the software knows best. The code developed to support this work is completely transparent to the user, allowing access at even a fundamental level, and provides complete oversight of the specific physics involved at every level of the programme.

4.1.1 Model Control

Physical equation solvers are plugged into a programme structure that is designed for purpose. Every variable can be read by the user, and this information can be published at the end of each calculation cycle allowing the user to analyse the data that is used and produced with very fine detail. This can lead to large amount of data being produced, and the programme also allows for control of when this occurs, thus also allowing the user to avoid information overload.

4.1.2 Flexibility

The code developed for this work is specifically written to take full advantage of multi-core machines. Although designed for use on JUROPA, the *Forschungzentrum Jülich*'s cluster machine, the code can be deployed on any parallel platform that supports MPI (Message Passing Interface). This does not necessarily need to be a supercomputer, but can also be a small scale office cluster network that has been set up with MPI.

The code is also specifically designed to be flexible in scale, with a view to allowing the user to model any size of fuel cell stack. It does this by subdividing cells into elements, and allowing elements to communicate with each other, exchanging information about their temperature, current and potential. This not only allows the user to accommodate any stack, but also to apply more computing power to the problem as the code grows in complexity, thus giving the user direct control over convergence time. Smaller clusters can be used, albeit as long as the time for convergence is reasonable. If processor capacity is not an issue, cells can be spread across many cores, and convergence time significantly reduced.

Each element has an associated numerical mesh that is used by numerical solvers to calculate the domain variables. If we consider a cell composed of several elements, together the cell contains '*ppc*' points per cell. Each element is assigned to an individual CPU. Convergence time can be calculated as

$$t^{element} = \frac{\text{ppc}}{epc}\left(\bar{n}^{it} \times \bar{t}^{it}\right)$$

where t is convergence time per CPU, $\bar{n}^{it}$ is the average number of iterations per point and $\bar{t}^{it}$ is average run-time per point per iteration – the time required to solve a single average point on the mesh in a single pass of the solvers.

Convergence is determined by the residual error calculated for each mesh element after every solver cycle. Once the maximal residual error is lower than a user specified number the calculation is considered converged. Convergence time is strongly determined

by how smooth the solution for each variable is. Regimes with sharp changes in the domain variables need more time to be solved. To get round this the user must apply a finer mesh in order to reduce the gradients between mesh points. A finer mesh means more points that each CPU must calculate, and if one uses uniform square meshes doubling the number of points per edge causes computing work to quadruple. However, a finer mesh also reduces the total number of iterations needed for convergence. Details of convergence and computational load for the simulations can be found in section 6.6.

4.1 Numerical Details

The simulation code is designed to be used in conjunction with local HPC resources, specifically the JUROPA cluster. JUROPA is a Simultaneous Multi-threading machine consisting of 2208 computing nodes, with each node made up of 2 Intel Xeon X5570 (Nehalem-EP) quad-core processors. Each processor has a clock speed of 2.93 GHz and 24 GB (DDR3; 1066 MHz) of memory available. This gives JUROPA a total of 17664 cores total, and a peak performance of 207 Teraflops. Each unit is solved on a separate core; upon completion of an iteration step the units exchange the data with the neighbours. This approach allows fast simulation of an application – relevant 100 – cell stacks by using large number of cores (about a thousand or more). Each cell has a resolution of approximately 600 points per side – meaning 360000 total grid points per fuel cell of a size of 15 by 15 cm^2. For smaller meshes we observe a loss of convergence of the Poisson solver for BP voltage. Typical simulation runs require 16 cores per cell meaning 80 to 160 are needed for short stacks, and 800 to 1200 for long-stacks. Solutions to reference stacks converge quickly usually taking one minute to solve a single point in the polarisation curve. Non-standard regime of stack operation requires more time, and although this is dependent on what kind of disturbance occurs within the stack, for typical feed disturbances one point in the polarisation curve takes about two minutes.

4.2 Poisson and Zero-In Solvers

In this section details of the numerical solvers are given. These solvers are well known, and widely used for numerical applications. Iterative numerical methods are needed to solve some of the model equations.

The SOR (successive over-relaxation) numerical Poisson solver is a well-known and robust tool for solving numerical 2D Poisson equations. The solver works on each mesh point, applying an input function to iteratively converge on the solution according to

$$\phi^{n+1} = (1-\omega)\phi^n + \omega \cdot f(\phi^n)$$

where ϕ^n is the domain variable at step n, $f(\phi^n)$ is the 5-point numerical approximation of the Laplace operator in the 2D space, and ω is a relaxation parameter that hinders rapid changes during the iteration process, which can lead to instability.

Nonlinear equations have been solved using the Zero-In solver, which is another well known, and sturdy root finding solver similar to the Newton solver. . This solver is primarily used to find the overpotentials, from the electro-chemical model, given the load current, feed concentration, and temperature.

4.3 Algorithm

The programme goes through three main phases: Initialisation, calculation and reporting (Figure 4.1). In the initialisation phase the code has to determine what resources are available, and how to distribute these accordingly.

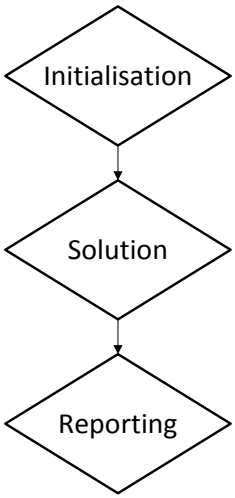

Figure 4.1: Schematic of the three conceptual phases in the programme's algorithm – Initialisation, Solution and Reporting.

Once resources (CPU cores) are allocated, the programme constructs a stack from the allocated resources and reserves memory space for variables in preparation for the next phase – calculation.

In the calculation phase solver functions iteratively provide solutions to Poisson equations for the stack temperature and voltage, making it necessary to exchange information with neighbouring elements (see below). Once conditions have been met for the solver to finish this iterative process, the solution data is passed to a printing routine, and the solver is re-engaged for the next operating point on the polarization curve, using the solution obtained as an initial condition.

Each routine is a separate object within the C++ object oriented programming (OOP) context. This ability to separate specific functionality into discrete sections of code, known asobjects, is the main reason for choosing C++. The modular design also provides clarity when

dealing with complex programmes, providing transparent structure and organisation to the code.

4.3.1 Main Function

. At the start of the simulation three significant initialisations occur: class variables, communication groups and mesh objects (Figure 4.2). Variables initialize with user defined default values, which cover stack parameters such as cell geometry, feed concentrations, coefficients, etc. Communication initialization sets up how elements relate spatially to each other; this is further detailed in section **Error! Reference source not found.**. Once an element knows its position within the stack, it initializes all necessary mesh objects – the numerical grid on which the solvers will work. A mesh object is the data structure that contains local variables in a grid, as well as the basic solver routines that work on that grid to solve model equations. This mesh object forms the fundamental building block of the simulation. At this point the simulation has created our stack in the virtual environment, and the simulation is ready to begin calculating.

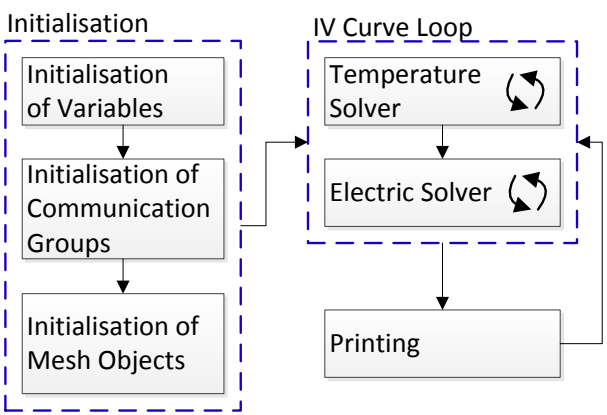

Figure 4.2: Schematic of sub-sections of initialisation and of numerical solvers. Initialisation has three distinct parts, where variables, communication groups and mesh objects are set-up. Each solver consists of an iterating loop, with convergence conditions that cause the loop to break once complete.

The code then enters the polarization curve loop. This loop steps through the current range that the user defines, at user defined intervals. This iterative block contains both temperature and electric models, and iterates until the residual error for both solvers is lower than the proscribed limit. The solver algorithms are described below.

Once convergence conditions have been met the code prints all raw mesh data, and adds the latest data point to "compiled reports" like polarization curves, as well as cell averaged parameters and convergence reports.

In the next point on the polarization curve the initial values for each mesh variable are taken as those from the previous point. This is particularly useful for points that lie close together on the polarisation curve, as each profile will be very similar to the previous one, and by using the previous results as the starting point for the next iterative step, convergence time is significantly reduced. These values are also saved to the disk, and provide a useful back-up should the programme terminate prematurely. This data can then be read at the start of any simulation run, and allow the user to continue interrupted simulations.

4.3.2 Temperature

The temperature solver loop iterates to produce stack temperature, schematically represented in Figure 4.3. The Poisson solver requires an input function from the model equations, and consists of the RHS of Eq. (3.24). The Poisson solver iterates until a residual error of 10^{-5} is reached, at which point it refreshes the boundary heat fluxes for edges and endplates, checks global residual – the residual for all elements in the stack, and re-iterates.

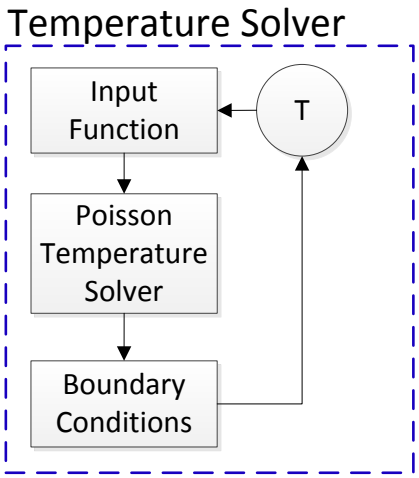

Figure 4.3: Schematic of the temperature solver loop showing Poisson input function where model equations are inserted; the solver; and (re-)calculation of boundary conditions.

4.3.3 Electric and Electrochemical Model

The electrochemical model determines the overpotential losses based on load current (see Eqs.(3.2), (3.3)). Implementation of this model is schematically represented in Figure 4.4 as the code within the "Polarisation Curve" blue bounding box, together with the electric model. The electrochemical model provides the electric solver with voltage losses, allowing it to solve for a profile for BPP voltage. In the electric model the polarization curve part runs first, taking the initialised BPP voltage as the input on the first iteration, and the actual voltage thereafter. Overpotentials are calculated using the model described in Eqs.(3.2), (3.3). BPP voltage is then reinserted into the electrochemical model, which re-calculates overpotential losses. Local concentration and velocity profiles are also determined by the electrochemical model based on local current which is derived from the polarisation curve model (section **Error! Reference source not found.**). These correspond to variables j_{cell}, C_m and v_m depicted in Figure 4.4.

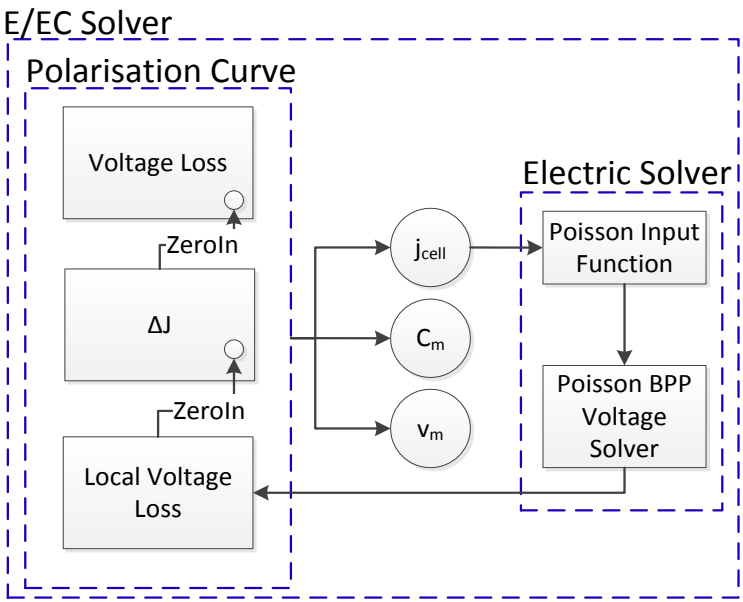

Figure 4.4: Schematic of the electric/electro-chemical model showing polarisation curve and electric solver modules. The polarisation curve module feeds values for local current to the electric solver module, which in turn feeds values for BPP voltage back to the polarisation curve solver iteratively.

4.4 Communication and Scaling

Because the stack is divided up, the programme needs to link cells together to provide the entire solution. The process of information exchange that allows the code to link all the elements together is referred to as communication. This section contains an overview of how it works in principle, and how it enables the stack model to be extremely flexible in scale.

Each cell in the stack is divided into elements. These are rectangular sub-divisions that contain numerical meshes that hold various data and domain variables, and form the input of the numerical solvers. Elements are given a default global rank the moment they are created, at the initialisation phase. Although this allows us to identify each element, however

subdividing this global set into smaller subsets is necessary to define stack and cell geometry and to simplify communication. Each element is given a rank based on its position within the cell – its section rank; each cell is given a rank within the stack – cell rank. These two subsets of rank are important for the two types of data transfer: intra- and inter-cell communication.

Because elements only cover part of the cell they need to communicate with each other in order to pass the current value of their domain variables to each other to generate a homogenous cell picture. Where there is no common edge with a neighbouring element, i.e. the element is on the edge of the cell, boundary conditions are defined. MPI handles the identification and physical distribution of this information using handles that are opaque to the user, meaning that it ensures that data is passed to the correct processing cores, without the user having to manage physical addresses. Figure 4.5 shows a schematic of this type of communication, where variables in the overlapping zones are passed between elements within a cell. All elements share two columns within the mesh array with each neighbour. This common set of points corresponds to the same physical position on the cell, and elements pass the inner column, and receive the neighbours' data into the outer column – mesh edge.

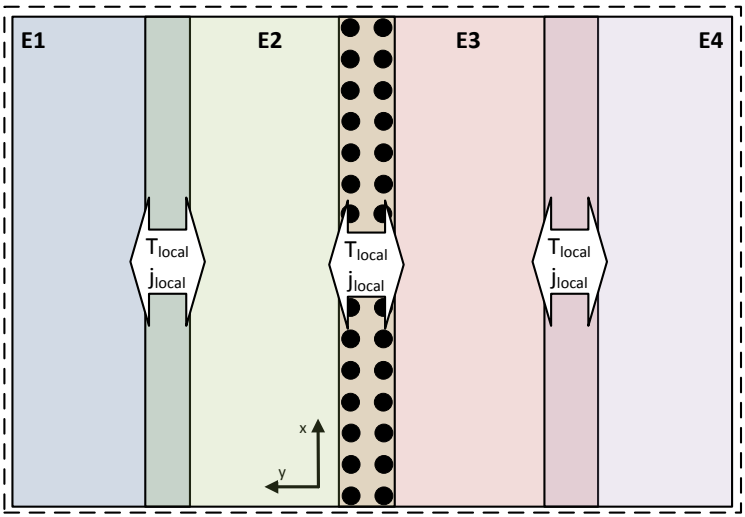

Figure 4.5: Schematic of inter-cell communication. Cells are divided into elements which transfer data between each other in order to create a smooth picture of the entire cell. Elements – E1 to E4 – exchange data for overlapping points (black dots) passing the column data one in from the edge, and receiving into its edge column from its neighbours.

In order to account for axial effects, elements also exchange their variables with neighbours in adjacent cells (Figure 4.6). These elements have the same section rank within the cell, but a cell number of either $n-1$ or $n+1$. Elements pass their entire temperature and voltage arrays to both adjacent cells, or just to one neighbour if they form part of an endplate, and store corresponding arrays received from neighbours. Similar to intra-cell communication, where a cell is an endplate, boundary conditions are prescribed.

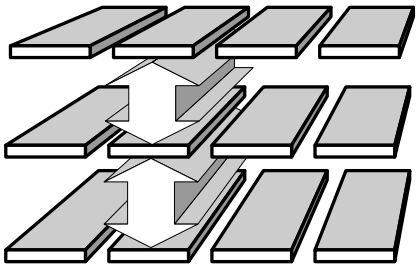

Figure 4.6: Schematic of intra-cell communication. Elements transfer data between others in neighbouring cells in order to create a smooth picture of the entire stack. This type of communication encompasses transport effects through the stack, allowing multi-cell stacks to be simulated. In this case the entire mesh array is sent to its neighbours.

4.5 Summary

The programme is designed to allow the simulation of a DMFC on a multi-CPU computer system, or multiple computers. At the core are two well-known and sturdy numerical solvers, and these are used to solve physical equations derived in chapter 3. The code distributes the load by dividing the stack up into smaller elements that are given to each CPU. Data is compiled back into one homogenous picture, which manages the seamless passing of data between elements so as to produce a complete unbroken image of the stack. The programme is built in modular fashion typical for C++ programmes, with distinct functionality separated into discrete sections of code.

5 Model Fitting

Fitting is a key element of model validation, and in this chapter a direct comparison is made between the 3D model and experimental data. The primary method used to do this is by comparing experimental polarisation curves to simulated ones. This is particularly useful, because the curves provide a picture of overall performance across a range of operating currents, and allow us to check whether all aspects of the model fit with expected data.

In this chapter the parameters are collected into three sets based on what aspect of cell operation they affect. These three categories are geometry and material constants, values governing electro-chemical performance and fuel supply parameters.

Fitting is done in two stages: First using the 0D model for a first approximation for all parameters, and then this data is inputted into the 3D model for the second stage of the fitting process. Fitting is initially done using Maple and the 0D model to obtain a first guess for each respective parameter to be fitted using Maple's internal curve fitting routines. These are then fed to the large stack model, compared to experimental data and adjusted to provide a precise fit.

5.1 Typical Experimental Stack Variants and Constants

Typically, the following cases have been considered for curve fitting: experimental lab scale test cells or short stacks typically running with 1 M methanol feed at stoichiometries under 10. Long stacks in the 1 kW power range run at lower feed concentrations from 0.25 – 0.35 M, and feed stoichiometries typically between 10 – 20.

Single cells are run isothermally at the desired temperature of 70 °C, and are heated using the anode feed and/or heated endplates, while stacks of more than ten cells are run

adiabatically. Due to greater thermal mass, heat production, and better surface area to volume ratio these stacks do not require external heating.

Choosing the parameters that describe geometry is straightforward, as they pertain to easily measurable quantities. For the purposes of fitting, all parameters relating to stack geometry are kept constant. Cell dimensions are 17.75 cm at the sides producing a cell area of 315 cm^2. Actual stacks have serpentine anode flow-fields, while the cathode air channels are straight. The 3D stack model does not capture this specific geometry, but instead simplifies the flow to straight, non-ribbed flow channels. Many different cell geometries exist; the general characteristic of all flow fields is to spread feed as evenly around the cell surface as possible, and because of this, flow is generalized to straight non-ribbed channels in the model. This allows the model to transcend specific flow field geometries, by generalising their function. This approach avoids unnecessary complexity, and maintains a broader overview of cell function.

Material constants are generally well known, and are either provided by suppliers, or where this is not the case, the parameters have been measured in general characterisation experiments within the institute. Thermal and electrical conductivities, significant lengths, etc. can be found below in Table 5.1.

Table 5.1: Table of parameters governing cell geometry, and basic material properties.

Symbol	Description	Unit	Value
h_p	BP Thickness	m	0.005

L_c	Channel Length	m	0.150
l_m	Membrane Thickness	m	100×10^{-6}
l_b	Backing Layer Thickness	m	150×10^{-6}
S	Cell Surface Area	m^2	0.0225
T	Temperature	K	273+70

5.2 Electrochemical performance parameters: 0D

Electrochemical parameters appearing in Eqs.(3.2)—(3.3) have a significant impact on the stack/cell performance. Initial estimate for these parameters was performed using a 0D model discussed in Section 4. Generally, the procedure is as following. The equation (3.1) for the cell voltage with Eqs.(3.2) and (3.3) for the half-cell overpotantials was fitted to the experimental polarization curve of a single stand-alone cell. Some of the parameters in this equation have been fixed at their literature values, the others were treated as fitting parameters. Maple's *NonlinerFit* function, which calculates the best fit using a least squares method was used for the initial 0D fit. This method gives a fit with the minimum *variance* from the input curve, thus providing a fit with the least error variance from the target curve.

When fitting multiple different feed concentrations – varied C_m^0 – The 0D model solved in Maple produces a new set of parameters for each respective starting concentration. Maple produces different fit functions, corresponding to the different concentrations, which in turn provide marginally different outputs. This means that it is possible to produce a small range in which the parameter can lie. This parameter range can then be used for the large-scale model.

Important to note is that the fitting parameters obtained in this way result from a simplified 0D model. The main idealization which stands behind 0D model is uniformity of methanol and oxygen concentrations over the cell surface estimate.

Exchange current densities (ECD) are taken from literature sources. Changes to the ECD in either electrode cause a constant shift in the polarization curve, uniformly increasing or decreasing cell voltage. Raising or lowering either electrode's ECD has the effect of uniformly increasing or decreasing cell performance – shifting the whole polarization curve either up or down. Changes of less than 10 % from examples found in literature are considered acceptable. ECD for anode and cathode (A cm^{-3}) are

$$i_*^a = 94.25 \exp\left(\frac{35570}{8.314}\left[\frac{1}{353} - \frac{1}{T}\right]\right) \tag{5.1}$$

$$i_*^c = 0.08 \exp\left(\frac{73200}{8.314}\left[\frac{1}{353} - \frac{1}{T}\right]\right) \tag{5.2}$$

where T is the local temperature in Kelvin.

Figure 5.1 shows a fit against an experimental stack using base parameters from Table **5.1** and using the fitted parameters given in Table 5.2, and shows good agreement in the low current region – below 100 mA cm^{-2}.

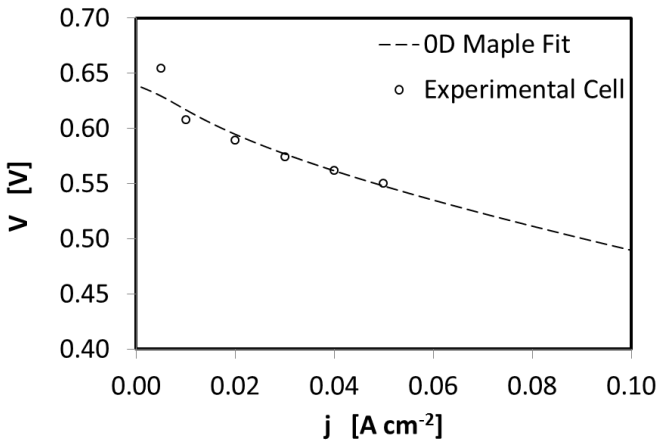

Figure 5.1: 0D polarization curve fit using Maple's *non-linear fit* function, and compared with the low current region of an experimental cell polarization curve.

Table 5.2: Parameters governing electro-chemical performance.

Symbol	Description	Unit	Value
b^a	Anodic Tafel Slope	V	0.036
b^c	Cathodic Tafel Slope	V	0.028
i_*^a	Anodic Exchange Current Density	A m^{-3}	(6.1)
i_*^c	Cathodic Exchange Current Density	A m^{-3}	(6.2)
R	BP Resistance	Ω m	5×10^{-5}
β_*	Dimensionless Cross-over		0.18
ε	Newman's Reaction Penetration		(3.16)
σ_t	Catalyst layer ionic conductivity	S m^{-1}	1

5.3 Fuel supply related parameters

The 0D model, by its nature of only providing overpotential losses for a specific concentration of reactants, neglects the change of methanol concentration along the length of the channel. When fitting the Stack model it is necessary for the effects of local concentration to be accounted for. This concentration profile is affected by several physical factors, and in turn influences local current production within the cell. The two-phase nature of the anode flow adds an additional layer of complexity to a model of consumption of methanol through reaction and cross-over.

One major consideration is that diffusion of methanol through the two phases differs by three orders of magnitude, while convective flow within the porous BL complicates the issue further. This means that it is difficult to develop a straightforward physical description

of methanol diffusion in the BL. As a first guess it is possible to assume that methanol diffusivity is that of a dilute methanol solution ($1.28 \cdot 10^{-9}$ m^2 s^{-1}). However, because gas bubbles improve methanol diffusion, methanol diffusivity can be expressed as a function of channel length – $D_m(x)$. Using a constant value for methanol is the simplest option, and the literature value for methanol in water diffusivity means that the methanol diffusion coefficient is that of the anode inlet

$$D_m(x)\big|_{x=0} = D_m^0 \tag{5.3}$$

Which is empirically derived in sub-section 6.1.2 – Determining Diffusion Experimentally. This is then used as the average diffusivity across the channel length – $\bar{D}_m$. Diffusion is, however, not locally solved. As CO_2 is produced it forms discrete gas channels in the ABL. These gas channels are reported to improve methanol diffusion through the backing layer as the diffusivity of methanol in CO_2 is three orders of magnitude larger than in water. However this is counteracted by the effect that local methanol concentration decreases, because it must diffuse out of the liquid phase, which is reduced due to the presence of bubbles. Diffusion is determined using limiting currents in an experimental stack at high methanol stoichiometry, the results of which are shown in section 6.1. In this manner the effective diffusion coefficient of the backing layer is determined as a function dependent on starting concentration. This provides a parametric dependence for diffusivity, but its weakness is that it is stack specific, and must be fitted for different backing layer, and flow field types, rather than being related to material or feed properties.

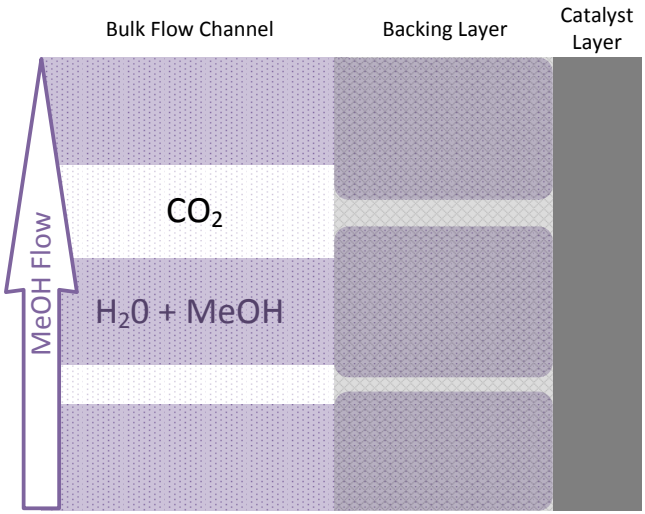

Figure 5.2: Schematic of CO_2 gas bubble channel formation showing a simplification of gas channels in the ABL, which are then wicked away by the anode feed stream.

In addition to the parameters used in the 0D model, parameters that govern more complex model aspects introduced by concentration gradients of reactants need to be fitted. One such parameter is k_v, which governs the acceleration of the anodic feed stream based on the rate of reaction, and captures the increase in velocity that bubbles cause. Increasing k_v has the same effect as reducing λ^a – causing the mass transport limited region of the polarization curve to occur at lower load current. This is because it has the effect of increasing anode feed flow velocity keeping feed molarity constant, and thereby steepening the methanol concentration gradient. This means there is less methanol available along the channel.

Another significant parameter related to fuel supply is crossover. Cross-over can be fitted according to two criteria: A cross-over current between 80 — 100 mA cm^{-2} at 100 mA cm^{-2} [46, 51, 81, 82], and cell OCV. The impact of changes to β^* are most significant in the low current region of the curve – load currents under 100 mA cm^{-2} for a cell with 1 M

feed concentration – where cross-over is the largest due to high available methanol and low load current.

Symbol	Description	Unit	Value
c_m	Methanol molar concentration	mol l^{-1}	1
D_M	Membrane Methanol Diffusion	m^2 s^{-1}	5×10^{-10}
D_b	Backing Layer Methanol Diffusion	m^2 s^{-1}	2.18×10^{-9}
k	CO_2 Bubble Acceleration		3

5.4 Summary

In this chapter parameters that appear in the model are defined, these determine all facets of stack operation and behaviour. Stack geometry, feed characteristics, and component material properties are taken from values for typical experimental DMFC variants, while electrochemical performance is fitted using Maple for the first approximation, and real stack performance data is then used for fine tuning. Feed parameters are defined by the operating conditions prescribed in each individual experiment, but in the case of backing layer diffusion calibration with experiments is undertaken. Further discussion of fitting along with the associated figures is handled in section 6.1.

6 Results

This chapter is divided into five sub-chapters that deal with results from fitting, three simulation cases and data on model performance. The three simulation cases deal with optimized operational regimes, feed disturbance and cathode flooding studies respectively.

6.1 Model Fitting

In this sub-chapter the results obtained from fitting the stack model with experimental data is presented. This section gives details on the efforts undertaken to validate the model with a real system, and shows the underlying strength as well as critical issues surrounding the application of the model to analysing DMFC stacks and their operation.

6.1.1 Electrochemical performance parameters:

0D Tafel Coefficients and Exchange Current Density

Figure 6.1 shows polarisation curves from the 0D-model fitted with an experimental lab cell. The experimental cell had an area of 17.64 cm^2, with a methanol stoichiometry of 4, and air stoichiometry 4 at 500 mA cm^2. Three different starting concentrations were simulated – 0.33 M, 0.5 M and 1 M methanol solution at the same feed lambdas as in the experimental cell. The experimental data points are fed into Maple, which then applies a fitting algorithm and produces the simulated curve. It shows Maple's fitting procedure produces a good fit for the low load current part of the polarization curve. This is, however, achieved using different values for the respective Tafel coefficients when fitting multiple starting concentrations of methanol, and provides us with the numerical fit for overpotential losses (Eq. 3.2 & 3.3). Additionally the curves completely fail above a load current of 100 mA cm^{-2} where the modelled curve becomes mass transport limited (MTL), while in the

experimental curve the MTL region has a flatter gradient, and reaches 0 V at around 500 mA cm^{-2} (Figure 6.3). These Tafel coefficients, however, provide a good first guess for the Tafel parameters in the stack model.

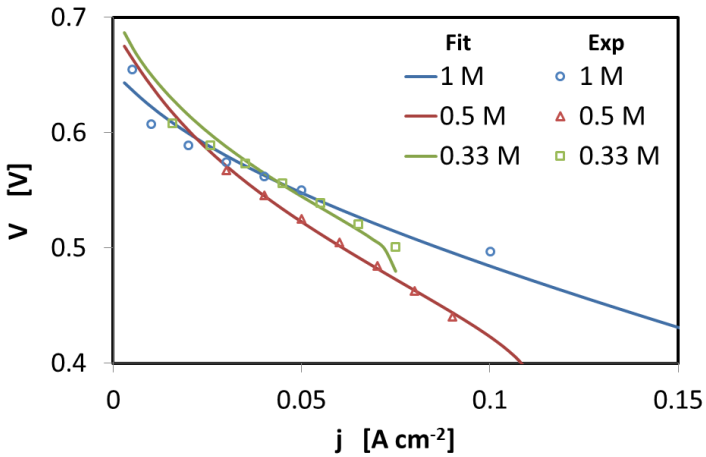

Figure 6.1: Experimental polarization curves (points) for three methanol concentrations: 0.33 M, 0.5 M & 1 M, with curves from Maple's *non-linear fit* algorithm (lines).

6.1.2 Fuel supply related parameters

One significant aspect that the 0D model fails to describe is changes to feed concentration over the length of the Channel. This change in concentration has a significant effect on current production within the cell, which needs to be compensated with fitted parameters taken from 0D model. Figure 6.2 shows a typical concentration gradient for a cell operating at 400 mA cm^{-2} with a methanol stoichiometry of 2.5 at 400 mA cm^{-2}. Educt flows along the *x*-axis in counter current. Methanol flows from $x = 0$ to $x = 1$, while air flows from $x = 1$ to $x = 0$. Spatially this corresponds to methanol flowing from the bottom to the top of the cell, and air from top to bottom.

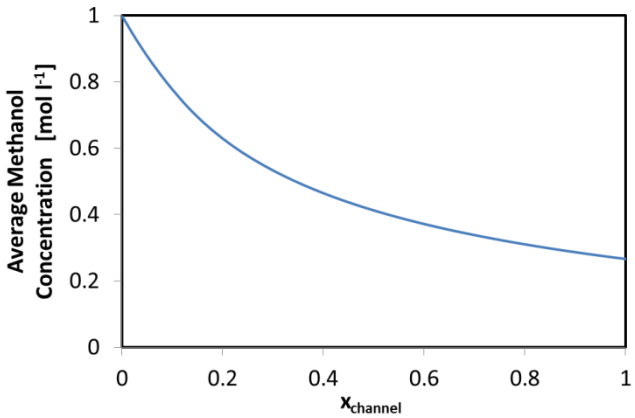

Figure 6.2: Average methanol concentration (including gas slugs) along the anode channel for a cell operating at 400 mA cm^{-2} with a methanol stoichiometry of λ^a = 2 @ 500 mA cm^{-2}.

The stack model shows lower performance because of reactant concentration gradients. This means that curves using the exact parameter set from the 0D model underperform compared to the projection derived from Maple. By trimming ECD and cross-over parameters, the curve can be re-aligned to the experimental curves.

In addition to concentration gradient the anode feed flow also experiences a change in velocity. CO_2 bubbles cause an increase to the volumetric flow in the anode channel. The velocity is primarily affected by the *k* factor in introduced in section **Error! Reference source not found.**, which governs acceleration due to bubble expansion; In this example *k*=3.

Both concentration gradient and velocity in the anode feed channel have an impact on the diffusion of reactants in the anode backing layer due to their influence on methanol concentration in the ABL. This is most prominent in the mass transport limited part of the polarization curve, and we can see that the 0D model utterly fails to accurately describe what happens to cell performance in this regime (Figure 6.3 above 0.2 A cm^{-2} for 1 M, and above 0.1 A cm^{-2} for 0.5 M).

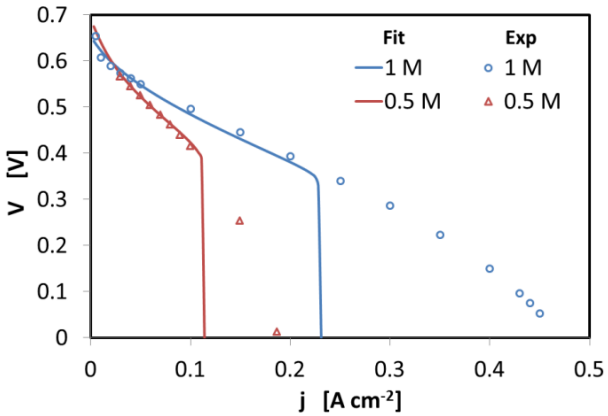

Figure 6.3: Full comparison of Maple fitted and experimental polarization curves showing clear disparity in the mass transport limited region.

The stack model follows the experimental curves better than the 0D model; however it overestimates performance in the mass transport limited region – the last third of each respective polarisation curve. Figure 6.4 shows simulation curves vs. experimental curves for four different concentrations: 0.33, 0.5, 0.76 and 1 M methanol feed concentration, this time using the full stack model. These curves show a much better fit with the high current regions of the experimental curves. Again, the experimental cell had an area of 17.64 cm^2, with a methanol stoichiometry of 4, and air stoichiometry 4 at 500 mA cm^{-2}. The cell was run isothermally at 70 °C.

The curves show good agreement in the low current region of the curve, with an error variance of 0.0149 under a current of 200 mA cm^{-2}, however above this current, in the high current regime, the variance is 0.231, with total variance for the entire curve equal to 0.232. I postulate that the overshoot is due to additional losses in either the ABL/GDL or respective catalyst layers that are not accounted for in the model. This could come from additional complexity in the diffusion of reactants or changes to the rate of reaction that is not addressed by the model equations [69]. However, in the range of normal operation – the low current regime – the model correlates outstandingly.

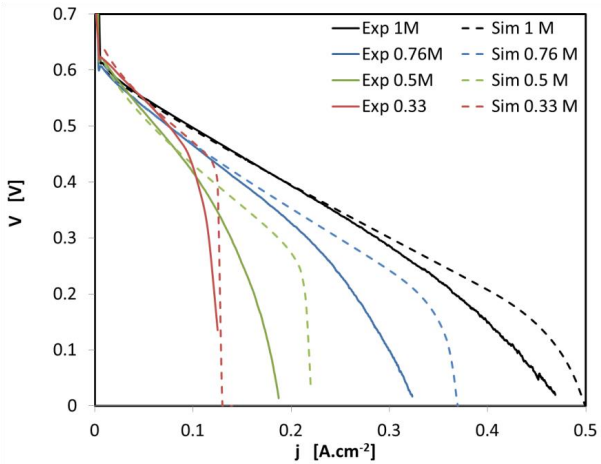

Figure 6.4: Comparison of Experimental and simulated polarization curves for four different starting methanol concentrations – 0.33 M, 0.5 M, 0.76 M & 1 M.

Determining Diffusion Experimentally

Using equation (3.12) together with experimental data for limiting currents (with excess air feed) it is possible to set the diffusion coefficient as the subject of the equation. This relationship of diffusion on concentration and limiting currents can be used to empirically determine the general effect of bubbles on the diffusion characteristics on the cell. Care has to be taken that concentration effects do not affect the outcome, but these can be excluded under certain conditions.

Figure 6.5 shows effective methanol diffusivity – D_{MeOH}^{eff} – determined using the equation for limiting current density (Eq. 3.12), and experimental data points for limiting current at the specified methanol stoichiometry for four different concentrations. As starting methanol feed concentration increases we see an increase in effective diffusion coefficient. This would suggest that higher concentrations improve the effect that bubbles have on improving methanol diffusion through the ABL.

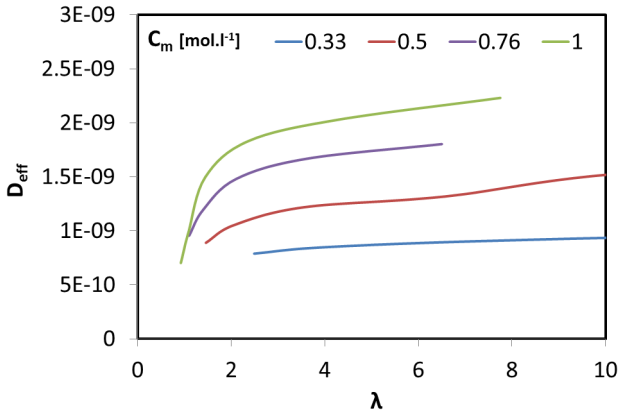

Figure 6.5: Effective diffusion coefficient transformed from experimentally derived limiting current plotted against methanol stoichiometry.

These curves can be used to derive the dependence of diffusion on feed concentration – providing a parametric relation for backing layer diffusivity based on methanol concentration. Caution is necessary when looking at this dependence at low concentrations, as it is not possible to exclude the possibility that concentration effects manifest strongly, and to eliminate this possibility high lambdas are considered safe. It is assumed that at very high methanol stoichiometry (above 10) the concentration gradient of methanol is minimal, and that the concentration remains that of the feed concentration – C^0_{MeOH}. At high lambdas D^{eff}_{MeOH} approaches an asymptote. This diffusivity can be considered the average diffusion at the corresponding concentration, as, due to high methanol stoichiometry, it is assumed that neither varies significantly. This asymptotic value is used to find the dependence of diffusivity – D^0_{MeOH} – on concentration, and is plotted in Figure 6.6. Parametric dependence of methanol diffusivity in the backing layer is taken as

$$D^0_{MeOH} = 1.595 \cdot 10^{-9} C^0_{MeOH} + 5.894 \cdot 10^{-10}$$

according to the fit with the experimental stack variant used for fitting.

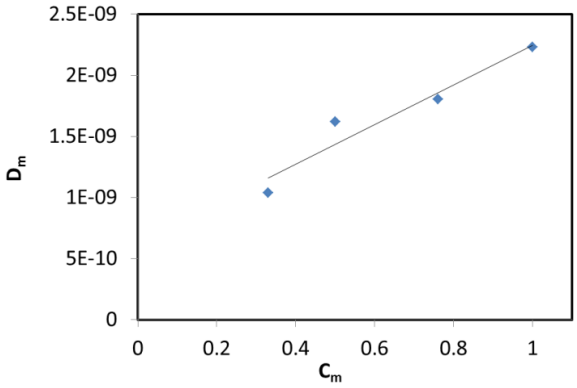

Figure 6.6: Effective diffusivity at high methanol stoichiometry calculated through limiting current equation (Eq. 5.12). Each point represents the asymptotic value for each curve in Figure 6.5.

6.2 Temperature Distribution

Figure 6.7 shows axial temperature distribution over different stack lengths. Spatially this corresponds to the average temperature in each BPP of the stack. This shows that temperature reaches a plateau in the middle of the stack, with temperature at the end-plates lower due to cooling from the surroundings. This temperature plateau is understandably higher for longer stacks, which produce more heat in relation to the surface, however this also approaches an asymptote as distance to the end-plates becomes less significant, and cell temperature is governed by heat flux to the surroundings through its own edges.

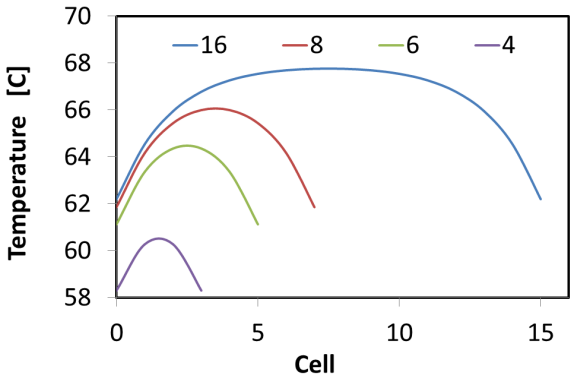

Figure 6.7: Stack axial temperature profiles based on average cell temperature for four different stack lengths: 4, 6, 8 & 16 cells.

Figure 6.8 shows two examples of cell temperature distribution – one of an end-plate and one of a cell in the middle of the stack. In both cases it can be seen that the cell's centre is warmest with heat flowing to the surroundings at the edges. Again, reactants flow along the *x*-axis in counter current. Methanol flows from $x = 0$ to $x = 1$, while air flows from $x = 1$ to $x = 0$. Spatially this corresponds to methanol flowing from the bottom to the top of the cell, and air from top to bottom. Methanol concentration is 1 M with a stoichiometry of 4, while air lambda is 10.

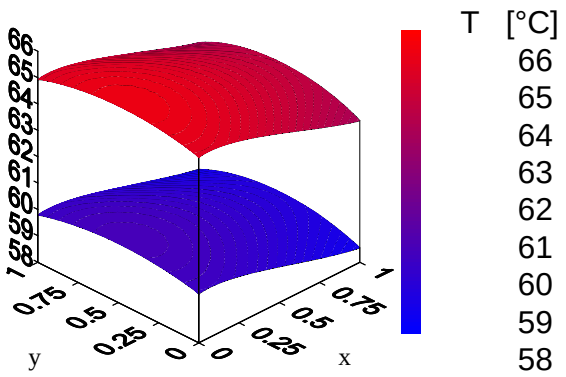

Figure 6.8: Local cell temperature profiles for cells from the end and middle of the stack. Methanol flows from $x = 0$ to $x = 1$, while air flows from $x = 1$ to $x = 0$. Methanol concentration is 1 M with a stoichiometry of 4, while air lambda is 10.

While methanol feed temperature and ambient temperature have an effect on the average stack temperature, it is the thermal conductivities of the BPP in both the in-plane and through-plane directions which determine the shape of local cell and axial temperature distribution. Figure 6.9 shows a 3D temperature profile for a 10 cell stack. Because of the low in-plane variation within the cell, it is reasonable to assume that cell temperature is isothermal, and for a sufficiently long stack, through plane variation can also be simplified. It is thus considered acceptable to assume the stack is isothermal for experiments that are only concerned with changes to the electric model, and by making this assumption we make significant savings in computing time.

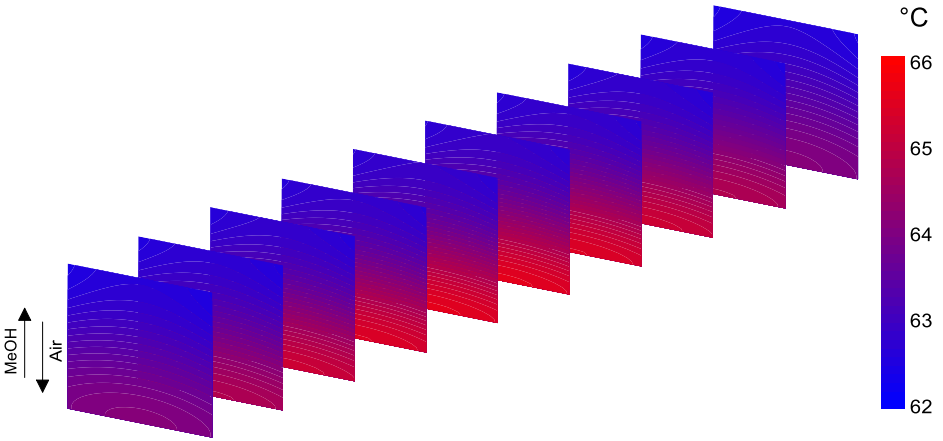

Figure 6.9: Cell temperature profiles for a 10 cell stack. Methanol flows from the bottom to the top of the cell, and air from top to bottom. Methanol concentration is 1 M with a stoichiometry of 4, while air lambda is 10.

6.3 Optimal Feed Parameters

In order to develop an idea of the optimal operational envelope of a DMFC stack, polarisation curves were used as a simple metric to compare performance of different stacks with varying feed parameters.

6.3.1 Methanol Stoichiometry

With increasing methanol stoichiometry the onset of mass transport limitation is shifted to higher currents, essentially extending the resistive region of the curve. For this stack variant a methanol lambda above 10 is redundant as the stack in amply supplied with feed, and is resistively limited (Figure 6.10).

Reducing methanol stoichiometry lowers the current at which mass transport limitation becomes significant. As λ^a approaches 1 limiting current decreases. This is because concentration gradients become steeper along the channel. When this happens the spread of local current production within the cell becomes larger. Figure 6.11 shows 3 profiles of local cell current for a λ^a of 2, 4 and 8 (L2, L4 and L8).

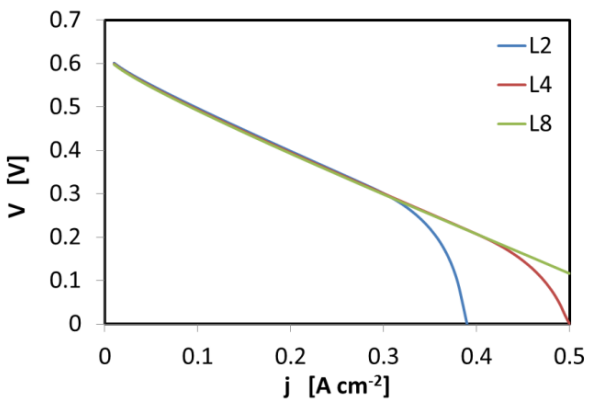

Figure 6.10: Polarisation curves for three different methanol stoichiometries – 2, 4 & 8.

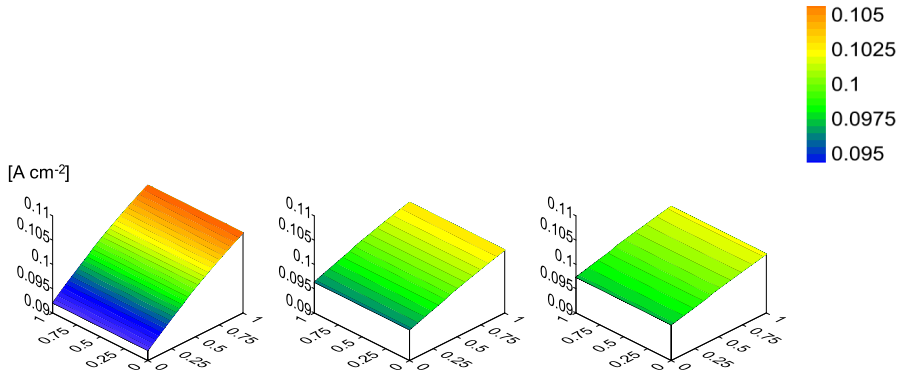

Figure 6.11: Local current profiles for three different methanol stoichiometries at an average load current of 100 mA cm^{-1} – λ^{a} of 2 (left), 4 (centre) & 8 (right).

6.3.2 Methanol Starting Concentration

Figure 6.12 shows a polarization curve for three different feed concentrations of methanol: 0.5 M, 0.76 M and 1 M; as C^{0}_{MeOH} decreases limiting current decreases. This is because concentration gradients become steeper along the channel, and the concentration gradient that drives diffusion of methanol through the backing layer becomes smaller.

However, reducing the feed concentration flattens the gradient of current production. Figure 6.13 shows 3 profiles of local cell current for a C^{0}_{MeOH} of 0.5 M, 0.76 M and 1 M at 100 mA cm^{-2}. This flattening out of the spread between minimum and maximum can be explained by the fact that cross-over is reduced due to lower concentration gradient driving diffusion through the membrane, and it is for this reason that it is preferable to run experimental stacks with the lowest possible concentration and highest lambda, as it leads to even local current production and high fuel efficiency.

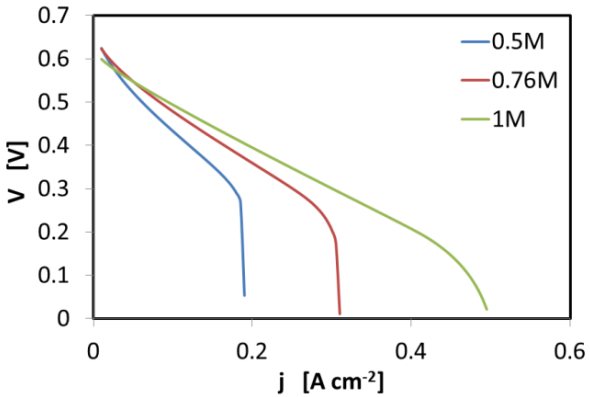

Figure 6.12: Polarisation curves for methanol stoichiometry of 4 at three different methanol concentrations – C^0_{MeOH} of 0.5 M, 0.76 M & 1 M.

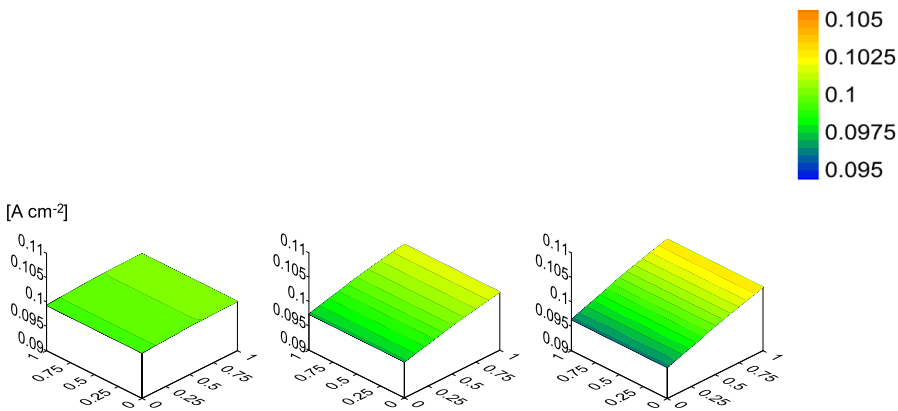

Figure 6.13: Local cell current profiles for methanol stoichiometry of 4 at 100 mA cm^{-2}, and three different methanol concentrations – C^0_{MeOH} of 0.5 M (left), 0.76 M (center) & 1 M (right).

The dependence of cross-over on concentration has been the focus of many studies. Increasing methanol concentration increases crossover, and this can be seen in Figure 6.14, which shows local cross-over current along the anode channel for three different lambdas for two different feed concentrations. It can also be seen that increasing lambda increases

overall crossover. This occurs because the drop in concentration over the length of the channel is flatter, and so crossover is higher at the outlet than at lower stoichiometries. Interestingly, halving the concentration drops crossover currents by around 80 %, although this cell exhibits crossover currents that are quite high – for typical DMFC concentrations of around 1 M – cells have crossover currents of around 80 mA cm^{-2} at a load current of 100 mA cm^{-2}. This significant reduction in crossover at lower concentrations is what improves system efficiency so dramatically, and negates the extra pumping costs involved in supplying methanol feed at stoichiometries of between 10 and 20.

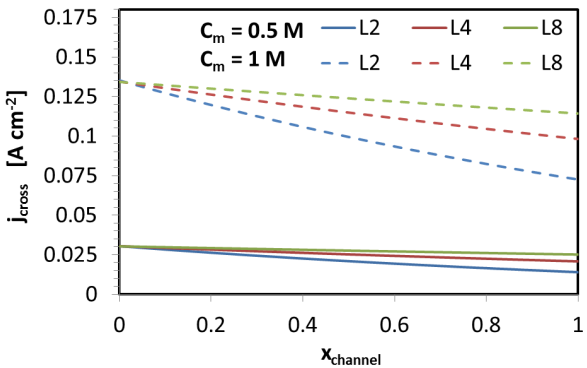

Figure 6.14: Local cell crossover current profiles along the anode channel for two different methanol concentrations – 0.5 M & 1 M, and three different methanol stoichiometries – λ^a of 2, 4 and 8.

Figure 6.15 shows concentration profiles for 1 M methanol feed concentration, and three different stoichiometries – 2, 4 and 8 all at 500 mA cm^{-2}. Important to note, is also the fact that these concentrations are based on the stream average concentration of methanol including CO_2 bubbles.

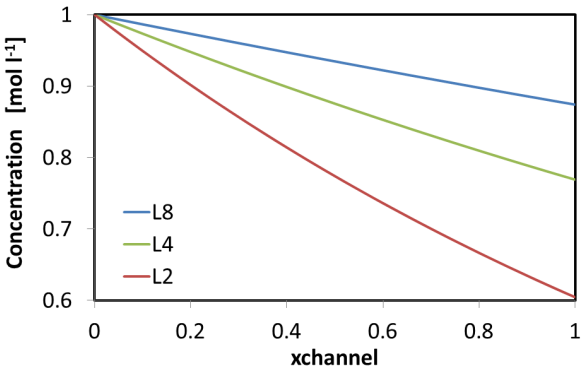

Figure 6.15: Local methanol concentration along the anode channel for a feed concentration of 1 M and three different stoichiometries – 2, 4 & 8.

6.3.3 Operational Envelopes

Using the limiting current it is possible to construct an operational envelope to find the best possible feed concentration and stoichiometry. Figure 6.16 shows limiting currents vs. methanol feed stoichiometry for three different starting concentrations. This shows the current at which the cell reaches 0 V for each respective starting methanol concentration.

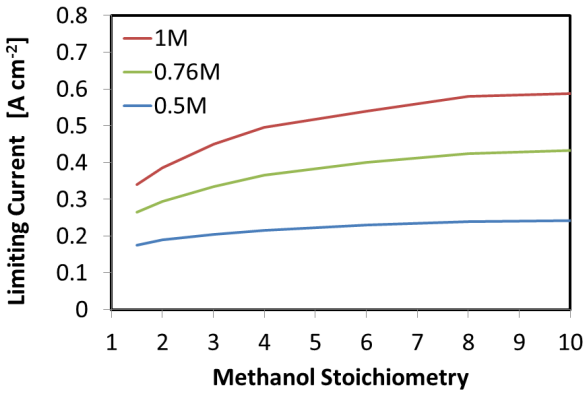

Figure 6.16: Stack limiting current vs. methanol stoichiometry for three different anode feed concentrations – 0.5 M, 0.76 M & 1 M.

This figure shows the hard limit of stack operation, and is therefore less useful for real applications. What is needed is an additional boundary condition: a minimum voltage condition. Real stacks have built in control cut-offs which shut the stack down, when stack or individual cell performance drops below a certain level. Typically these minimum allowable voltages are 200 mV individual cell voltage, and 300 mV average cell voltage. Figure 6.17 shows operational envelopes based on these new boundary conditions. These envelopes give an idea about global performance, however local cell voltage and current profiles should also factor into the decision of what parameters to use, and the local effects described in section 6.3.1 and 6.3.2 highlight the fact that lowest possible concentration, and highest possible lambda provide optimal local performance. However, it can be seen here that the average limiting current is not affected by methanol stoichiometries above 4. As Figure 6.10 shows, this is because an increase in lambda stretches out the resistive part of the polarization curve, without improving performance, and simply delays the onset of the mass transport limited region. Figure 6.17 also shows that the difference between limiting currents at the two voltage conditions get closer together at lower concentrations. It is postulated that this is due to the lower concentration driving force across the BL in the latter part of the anode channel.

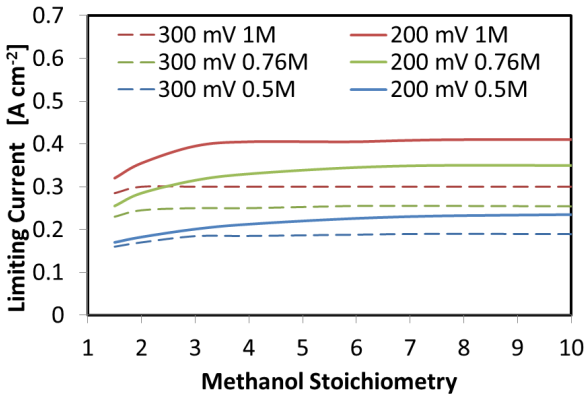

Figure 6.17: Limiting current vs. methanol stoichiometry based on a 200 mV minimum individual cell voltage (solid), and 300 mV minimum average cell voltage (dashed) for three different anode feed concentrations – 0.5 M, 0.76 M & 1 M.

6.3.4 Minimum Concentration

In real applications stacks usually operate between 100 mA cm^{-2} and 200 mA cm^{-2} and this combined with a 300 mV limit in average stack voltage provides a minimum boundary condition for methanol feed concentration. By incrementally lowering feed concentration, the lowest concentration that meets the performance criteria is found. Figure 6.18 shows 3 curves for 0.2 M, 0.275 M and 0.3 M methanol concentration at lambda 20, and shows that, while the minimum voltage condition is met, mass transport limitation means that a minimum concentration of 0.27 M is required to produce a current of 100 mA cm^{-2}. This concentration does however leave little room for error in the supply of methanol, and while performance is marginally improved by reducing concentration lower than 0.3 M, the gain in cell voltage is minimal.

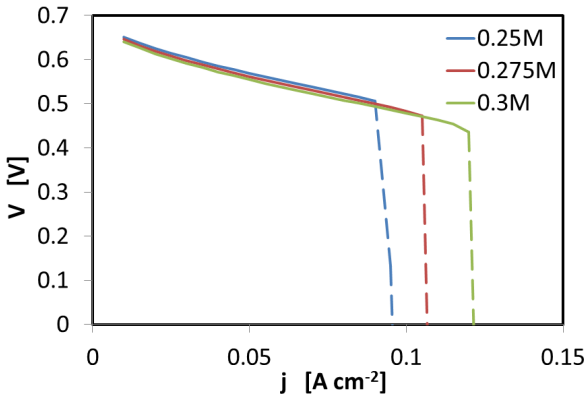

Figure 6.18: Polarisation curve for three methanol feed concentrations – 0.25 M, 0.275 M & 0.3 M.

6.4 Feed Disturbance

The model was used to study the effect of non-uniform methanol distribution over the surface of a single cell in a stack. We assumed, that the standard fuel flow corresponding to methanol stoichiometry of $\lambda^a = 4$ is applied to all the cells in a 5-cell stack each with 225 cm^2 cell area, except half of the cell #3, which is fed with a lower methanol stoichiometry. This situation models failure in the methanol manifold. Two different low methanol stoichiometries are used corresponding to two different severities of disturbance – $\lambda^a = 2$ (section 6.4.1 – Minor Disturbance) and $\lambda^a = 1.4$ (section 6.4.2 – Extreme Disturbance).

6.4.1 Minor Disturbance

Figure 6.19 shows current and anodic overpotential for a cell with half its area fed with $\lambda^a = 2$ and the other half with $\lambda^a = 4$. The parameters over the surface of the disturbed cell is compared to the distribution of parameters over the quasi-cell – "Reference", which

consists of two linked reference ”half-cells” fed with λ^a = 4 and 2. In order to quantify the effects caused by the feed disturbance, the parameters corresponding to the reference quasi-cell were subtracted from the simulated disturbed cell producing the absolute difference between reference and disturbed case – “Difference”. We see that this disturbance does not have any great impact on cell performance.

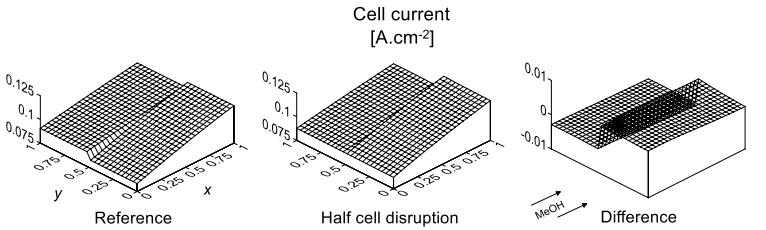

Figure 6.19: Local current profiles of (composite) reference case (left), disturbed cell (middle), and the difference between the two (right).

If we consider the local current profile shown on the left in Figure 6.19 – “reference” (also Figure 6.11 section 6.3.1) we see that the difference between maximums and minimums of λ^a = 2 and λ^a = 4 is only 5 mA cm^{-2} at 100 mA cm^{-2}. Figure 6.20 shows anodic overpotential for this case, and it can be seen that these two stoichiometric regimes differ only by 6 mV, while Figure 6.21 shows cathodic overpotential, similarly with a difference in the two regimes of only 2 mV. This indicates robustness against disparate flow regimes due mostly to the high in-plane conductivity of the BPP. This is looked at in further detail in the following section.

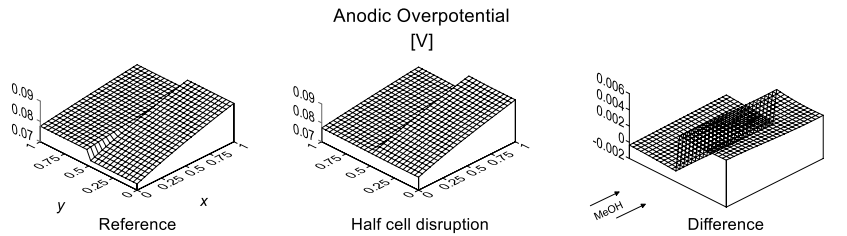

Figure 6.20: Local anodic overpotential profiles of (composite) reference case (left), disturbed cell (middle), and the difference between the two (right).

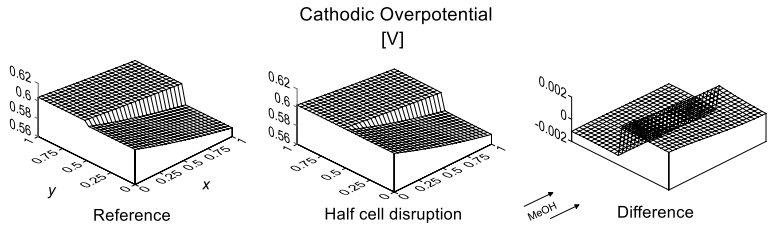

Figure 6.21: Local cathodic overpotential profiles of (composite) reference case (left), disturbed cell (middle), and the difference between the two (right).

6.4.2 Extreme Disturbance

The two reference cases are stacks run with a uniform methanol feed in all the cells, one at λ^a = 4 and the other at λ^a = 1.4. In all the cases air stoichiometry is kept high (λ^c = 10) such that mass transfer effects in the cathode channel are negligible. In the reference cases, the reactant feed is considered to be perfectly distributed along the y-axis (the width of the cell). Note that the methanol feed is supplied at the bottom of the stack (Figure 3.2).

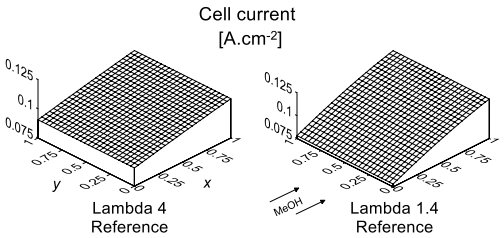

Figure 6.22: Local current profiles, j, for λ^a = 4 and 1.4 reference cases.

Polarization curves for both reference cells and disturbed cell are plotted in Figure 6.23. For all the cases a fixed load current was set at 100 mA cm^{-2}. The maps of local current

over the surface of reference cells are shown in Figure 6.24. Current at the methanol inlet is lower due to higher rate of crossover.

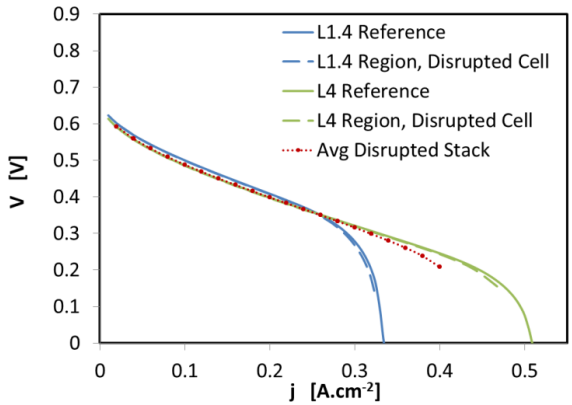

Figure 6.23: Local polarization curves in the cell with two different flow regimes compared with their respective reference cases. L4 and L1.4 refer to λ^a = 4 and λ^a = 1.4, respectively. Solid curves show the reference case, while broken lines show the local polarization curves within the disrupted cell for each flow regime. The curve "Avg Disrupted Stack" refers to the stack averaged polarization curve.

For convenience, the parts of the cell #3 fed with λ^a = 1.4 and 4 will be referred to as low- and high-λ^a domains. Below, the distribution of parameters over the surface of a disturbed cell is compared to the distribution of parameters over the quasi-cell, which consists of two linked reference "half-cells" fed with λ^a = 4 and 1.4. In order to quantify the effects caused by the feed disturbance, the parameters corresponding to the reference quasi-cell were subtracted from the simulated disturbed cell. This produces a picture of absolute difference between reference and disturbed case, that indicates how much each parameter changes. Figure 6.24 Figure 6.26 show each of these profiles – reference (quasi-cell), disturbed, and difference graphs.

Figure 6.24 compares the distributions of local current density. As can be seen, in the disturbed cell, the local current at the methanol inlet is uniform along the y-axis. Comparing the x-profiles of current in the disturbed and reference cells, we see that the shape of current in the disturbed cell is more uniform. This uniformity is achieved through a marginal decrease of current in the high-λ^a domain, and an increase in the low-λ^a domain (Figure 6.24). This homogenizes the local current in both domains.

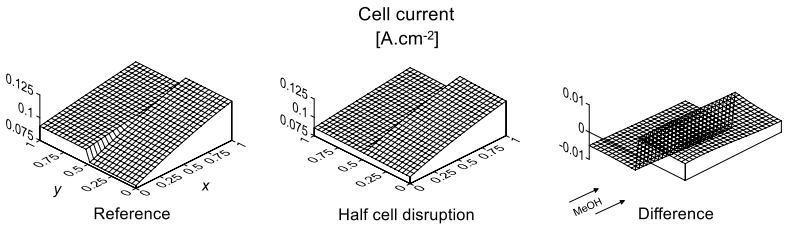

Figure 6.24: Local current profiles of (composite) reference case (left), disturbed cell (middle), and the difference between the two (right).

Homogenization of local current is supported by more uniform distribution of anodic and cathodic half-cell voltages in the disturbed cell, as compared to the reference quasi-cell. The anodic over potential at the inlet of low-λ^a domain is aligned with η^a in the high-λ^a domain; overall, the distribution of η^a in the disturbed cell is smoothed (Figure 6.25). The difference of anodic over potentials shows that η^a in the disturbed cell is higher than in the reference quasi-cell (Figure 6.25). This effect is due to slight decrease in η^a in the low-λ^a domain (Figure 6.25).

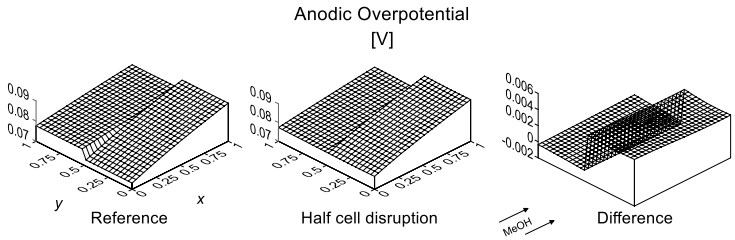

Figure 6.25: Local anodic overpotential profiles of (composite) reference case (left), disturbed cell (middle), and the difference between the two (right).

Similar homogenization is exhibited by the distribution of cathodic polarization η^c over the surface of the disturbed cell, as compared to the reference quasi-cell (Figure 6.26). Again, by increasing η^c in the low-λ^a domain, and decreasing in the high-λ^a domain, the "load" is more evenly distributed over the cell.

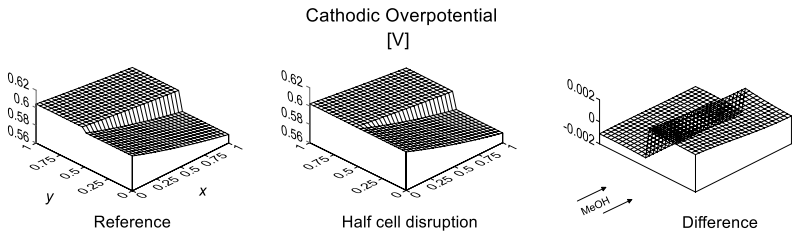

Figure 6.26: Local cathodic overpotential profiles of (composite) reference case (left), disturbed cell (middle), and the difference between the two (right).

Figure 6.27 shows the distribution of local current density over the stack volume. Due to high electric conductivity of BPs, the disturbance in cell #2 does not propagate through the stack.

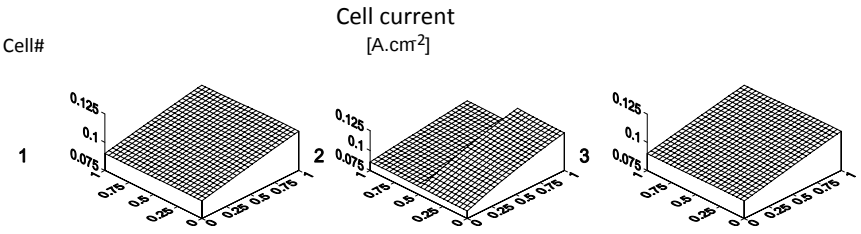

Figure 6.27: Local current profiles for a 5 cell stack, with middle cell – #3 – feed with two different methanol stoichiometries over each half of its area: λ^a = 4 and λ^a = 2.

Figure 6.28 shows the shapes of local current density in the disturbed cell along the y-axis at the three x-locations: at the methanol inlet (x = 0.1), in the middle of the anode channel (x = 0.5) and close to the channel outlet (x = 0.9). The curves at x = 0.5 and 0.9 show the peak of the local current at the interface of low-λ^a and high-λ^a domains (Figure 6.28). This peak manifests the following effect.

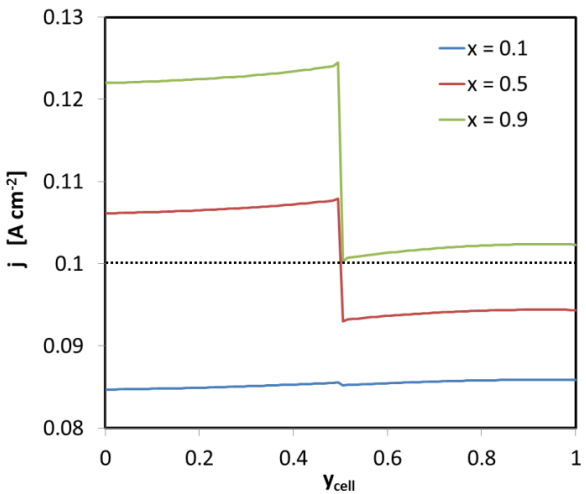

Figure 6.28: Cross-section of current along the y-axis of the disturbed cell. These are shown at three points along the channel – the start, middle and end corresponding to a x-coordinate (dimensionless) of 0.1, 0.5 and 0.9 respectively.

Consider three cells in a stack, the disturbed cell B, and two adjacent cells C and A with the regular methanol feed over the whole active surface (Figure 6.29). Due to imbalance in currents, current produced in the cell A under the high-λ^a domain of cell B cannot go through the cell B moving directly along the stack axis; this current must bypass the high-λ^a domain, as depicted in Figure 6.29. In cell B, this leads to the concentration of local current at the interface between the low- and high-λ^a areas (Figure 6.28). Formation of the peak of local current at the boundary of methanol-depleted region is quite analogous to formation of this peak at the edge of the resistive spot in the stack [61].

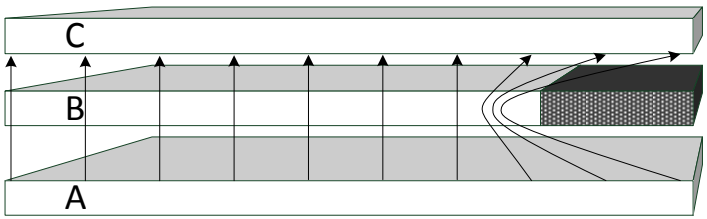

Figure 6.29: Schematic showing how current is diverted around a disparate flow regime. Current is "bent" around the lower feed regime indicated by the darker patch in cell B.

6.5 Cathode Flooding

Eq.(3.39) has been incorporated into our model of DMFC stack and several variants corresponding to different levels of *s* (flooded region) have been calculated. Parameters appearing in Eq.(3.39) are listed in Table 3.2; schematically shown in Figure 6.30. The normalized distance along the air channel at which the condensation front occurs – x^* – is set at 0.5 meaning that the front manifests at the channel midpoint. σ is 0.02 giving a transition between "dry" and flooded regions which is 4% of the total channel length.

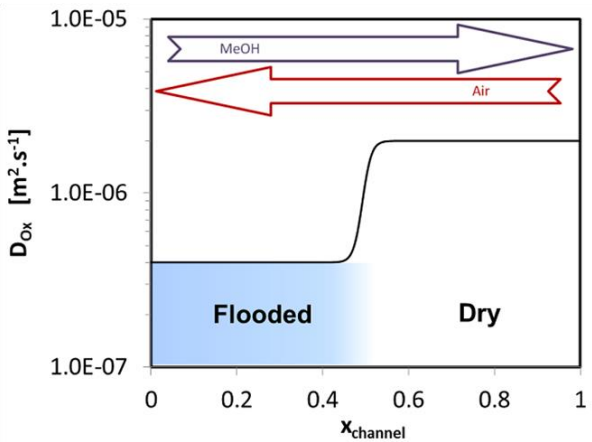

Figure 6.30: Schematic of oxygen diffusion showing the variation of oxygen diffusivity in the cathode GDL along the channel. Partially flooded regime is modelled as a rapid but smooth transition between two different diffusivities – D_{Ox}^{dry} & D_{Ox}^{fld} – along the air channel. Reactant are in counter-flow, with the air inlet at x=1 and outlet at x=0.

Varying liquid saturation s, the flooding amplitude parameter A_D is varied, and applied consistently to every cell throughout the whole stack. A_D needs to be progressively lowered between 1 and 0, and the impact on local performance analysed in order to establish the effect of flooding on the cell – at what point it starts to have an effect, and when this becomes catastrophic for cell operation. It is shown later in sections 6.5.1, 6.5.2 and 6.5.3 that the impact of flooding can be divided into three approximate regions non-critical, transition and critical.

6.5.1 Non-critical disruption

As with disruptions to cell operation discussed in section 6.4, cells that experience minor levels of flooding show little change from non-flooded reference cases. Figure 6.31 shows three levels of flooding – A_D = 0.2, 0.5 & 0.75 – as well as a dry reference case, all of which lie on top of one another in the resistive region, indicating that performance is not

effected at all. For a flooding amplitude parameter of 0.2 there is minor deviation from the reference case for load currents greater than 300 mA cm^{-2}.

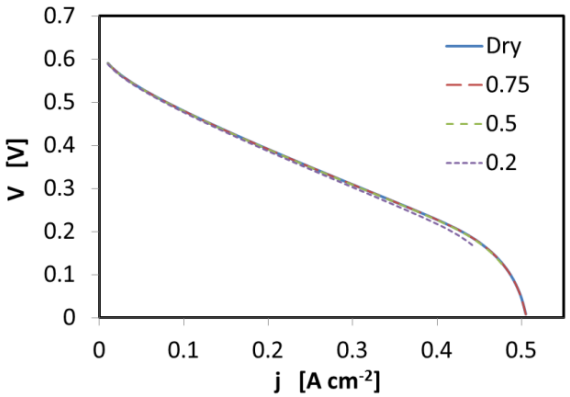

Figure 6.31: Polarisation curve for a reference dry cell, and three levels of (non-critical) flooding corresponding to a flooding amplitude parameter, A_D = 0.2, 0.5 & 0.75.

If we look at local current it is possible to discern a greater impact from flooding, however above A_D = 0.3 the relative change with respect to the dry reference is less than 5 % – a difference which is below the resolution of experimental locally resolved current measurements. In this work the boundary between non-critical and transition region of the flooding parameter has been defined as the point where the maximum relative difference in local current production between flooded and dry cell is 10 %. Depending on stack parameters this occurs in the flooding parameter range 0.2 – 0.3.

6.5.2 Transition region

Figure 6.32 shows polarisation curves for a non-flooded reference cell, partly flooded cell, and two curves corresponding to flooded and dry halves respectively. As expected the dry half-cell curve follows the non-flooded reference up until the mass-transport limited

(MTL) region. In this case A_D = 0.2, which lies in the transition region of the flooding parameter.

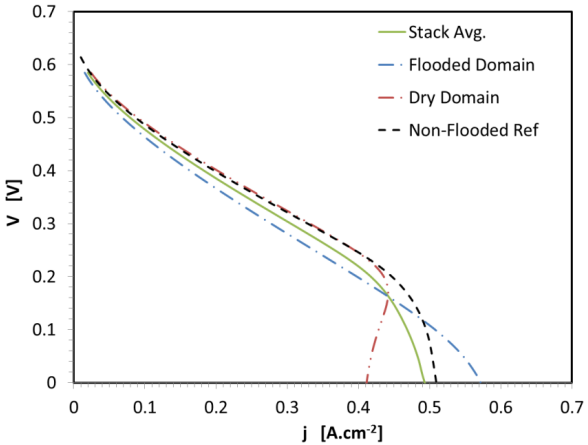

Figure 6.32: Polarisation curves for dry reference, stack average and two half-cell polarisation curves for dry and flooded regions.

Comparing non-flooded reference with a partly flooded cell we see that with the parameters used (Table 3.2), flooding brings a performance cost of between 20 – 40 mV across the typical working range of load current, and as expected, the cell average polarization curve lies between the half-cell curves. An intersect point of dry region, flooded region and average polarization curves occurs at 440 mA cm^{-2} where current production in the dry half becomes restricted, which is due to mass transport limitation in this half of the cell. Unexpectedly, this is brought about by transport limitations *on the anode side*, and will be discussed further below.

Low current region

Figure 6.33 shows local current density along the channel for several amplitudes of flooding A_D. The local current production clearly follows the shape of oxygen diffusion

profile, whereby current is higher at the air inlet (at x=1) and lower at the channel outlet (x=0).

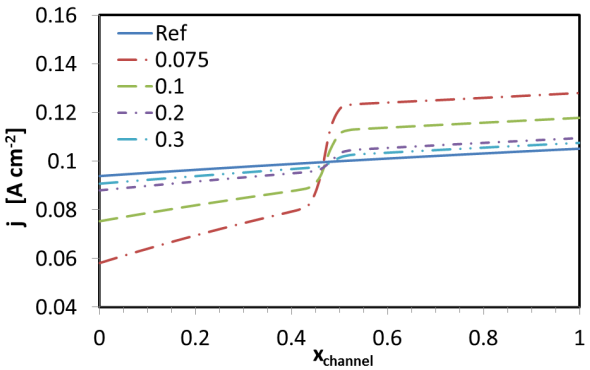

Figure 6.33: Local cell current along the channel for dry reference cell and four levels of flooding: A_D = 0.075, 0.1, 0.2 & 0.3.

Figure 6.34 shows cell current j_* at the air channel outlet (x=0) versus flooding amplitude parameter A_D. For disruptions with a parameter A_D greater than 0.2, there is no great impact of flooding on the cell performance. However, for A_D less than 0.2, the reduction in current production in the flooded region is severe. Current in the flooded domain eventually drops to zero, where there is then a significant risk of cell reversal.

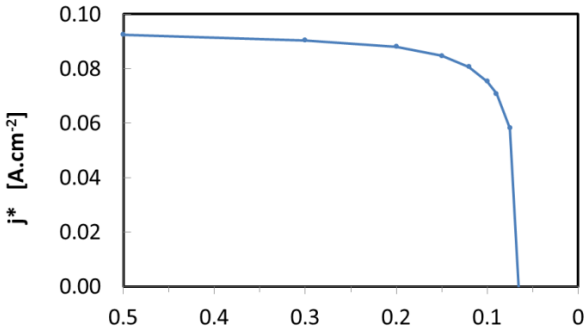

Figure 6.34: j* – the current at the air channel outlet (x=0) – plotted against the flooding parameter – A_D .

Anodic overpotentials for different flooding amplitudes are shown in Figure 6.35. Overpotential in the dry part of the cell is higher where most of the current is produced, while the flooded half of the cell under-produces.

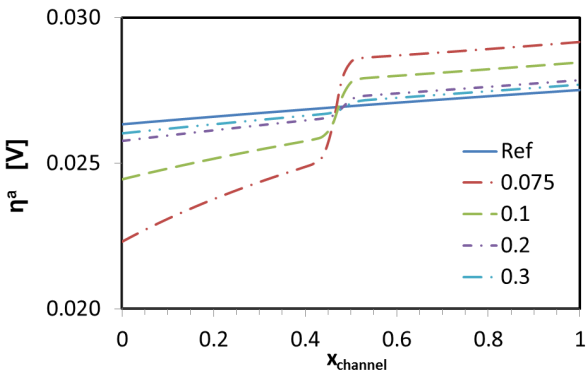

Figure 6.35: Anodic overpotential along the air channel for five different flooding parameters: A_D = 0, 0.075, 0.1, 0.2 & 0.3.

Figure 6.36 shows cathodic overpotential along the channel. We see that this is higher at the end of the air channel (x < 0.5) where oxygen diffusivity is low, and approaches the reference cell value in the high diffusivity region.

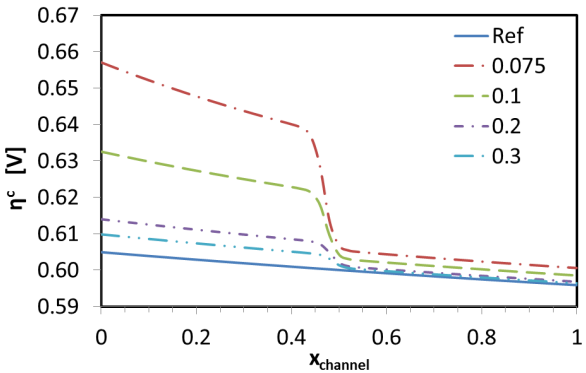

Figure 6.36: Cathodic overpotential along the air channel for five different flooding parameters: A_D = 0, 0.075, 0.1, 0.2 & 0.3.

High current region

The limiting current region which encompasses the final third of the polarization curve (Figure 6.32 from 400 – 600 mA cm^{-2}) is where the over-potential losses due to mass transport limitations become the most significant. The limiting current density profiles necessary to understand this phenomenon can be seen in Figure 6.37 and are plotted using the formula

$$j^a_{\lim} = \frac{6FD_m C_m}{l_{BL}}$$

$$j^c_{\lim} = \frac{4FD_{Ox} C_{Ox}}{l_{BL}}$$

Where $j_{\lim}^{a}$ and $j_{\lim}^{c}$ are anodic and cathodic limiting current density respectively; F is the Faraday constant, D_{m} and D_{Ox} are the methanol and oxygen diffusion coefficients in the BL (backing layer), C_{m} and C_{Ox} the local concentrations of methanol and oxygen respectively in the channel and l_{BL} is the thickness of the backing layer. The anodic limiting current shape is similar to that of the methanol concentration profile, while the cathode limiting current follows the *tanh* shape of oxygen diffusivity (Figure 6.30). In order to get the actual limiting current we need to take the minimum value of both these functions.

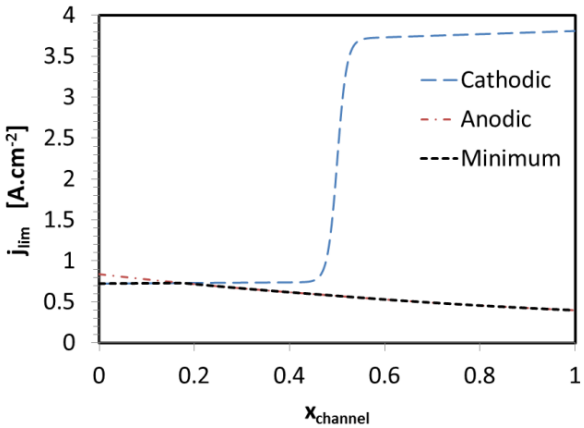

Figure 6.37: Local limiting current for both anode and cathode, showing the minimum limiting current (broken line) for A_D =0.2.

Figure 6.38 shows local current profiles for three different average load currents – 300, 400 and 440 mA cm^{-2} respectively. At 300 mA cm^{-2} it can be seen that local current is not yet limited, and is similar in shape to those at lower currents. At 400 mA cm^{-2} the current at x=1 just touches limiting current, and we start to see some restriction in current production in the dry half part of the channel. This is fully developed at 440mA cm^{-2}, which is the point where the intersection in Figure 6.32 occurs, and is the point where the local current in the dry half of the channel is entirely methanol transport limited.

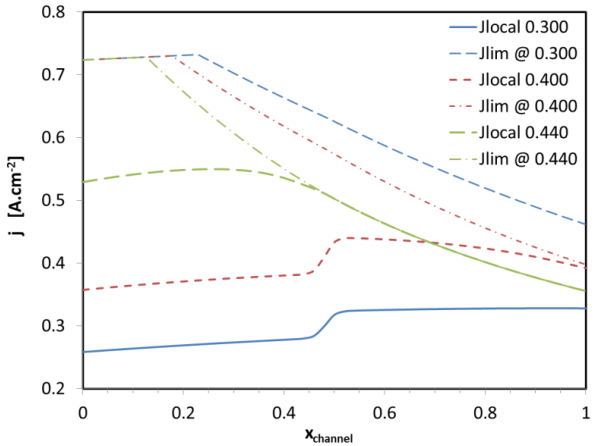

Figure 6.38: Local current density and local limiting current shapes for mean cell current densities of 300 mA cm^{-2}, 400 mA cm^{-2} and 440 mA cm^{-2} A for a flooding parameter of A_D =0.2. Methanol flows from *x* = 0 to *x* = 1, while air flows from *x* = 1 to *x* = 0. Methanol concentration is 1 M with a stoichiometry of 4, while air lambda is 10

Because current production in the dry region has to compensate for the flooded region, it reaches the limiting current sooner than it otherwise would. The flooded region then takes over as the main producer of current, because the dry half of the channel has reached anodic limiting current. This leads to even greater strain on the cell, and elevated overpotentials are seen in both electrodes.

Anodic overpotential becomes large on the dry side of the channel. Figure 6.38 shows that as the load current increases from 300 mA cm^{-2} to 440 mA cm^{-2} the gradient of η^a increases drastically on the dry side. The range of values in the η^a curve at 300 mA cm^{-2} spans 10 mV, whereas at 440 mA cm^{-2} these span a range of 130 mV.

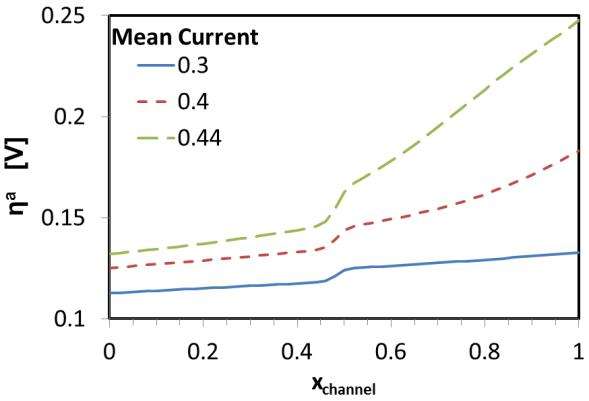

Figure 6.39: Anodic overpotential for three cell current densities: 300 mA cm^{-2}, 400 mA cm^{-2} and 440 mA cm^{-2}.

In contrast the cathodic overpotential η^c increases on the flooded side, but starts to drop on the dry side (Figure 6.40). At load currents less than 400 mA cm^{-2} the spans of η^c remain fairly constant at around 40 mV between their minimum and maximum, and the shape remains similar to the *tanh*-like shape of oxygen diffusion. However, in the MTL region, an interesting effect manifests once the whole dry half of the cell is at limiting current (above 440 mA cm^{-2} load current): At the channel inlet, η^c drops below that of lower load currents. Thus is because of progressive lowering of the local current at the air channel inlet caused by methanol limitation on the anode side.

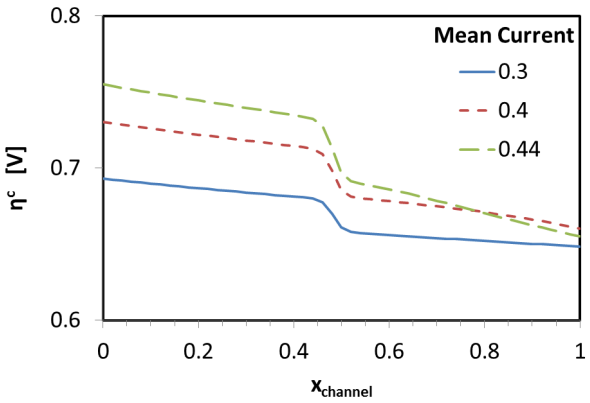

Figure 6.40: Cathodic overpotential for three cell current densities: 300 mA cm^{-2}, 400 mA cm^{-2} and 440 mA cm^{-2}.

6.5.3 Critical disruption

As the disruption becomes critical – A_D < 0.13 – the whole polarization curve shifts, causing the low current region to shrink, and the onset of mass transport limitation (the high current region) to occur earlier. Once A_D has reached 0.07 the cell starts to become bifunctional, with part of the cell area operating as an electrolyser.

Low Current Region

Figure 6.41 to Figure 6.43 show a flooding parameter of A_D = 0.1. Several factors make this level of flooding critical: Large reduction in current production in the flooded zone; high cost of current production on the cathode side – high η^c; and the subsequent shifting of the dry zone to high local currents that cause it to become mass transport limited at lower average load currents.

Figure 6.41 shows the local current spread for an average load current of 100 mA cm^{-2}. Current production at the start of the methanol channel has dropped to almost 3/4 of the average load current – 80 % of the dry reference value at this point. On the dry side of the cell it can be seen that local current is elevated in order to counteract the under production of the flooded region. Important to note that local current production at x=0 is below 90% of the reference curve.

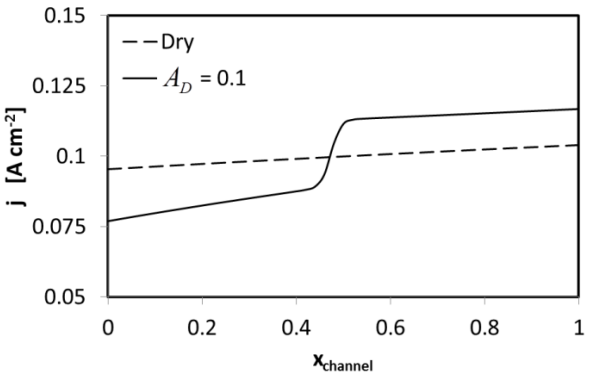

Figure 6.41: Local cell current along the channel for dry reference cell and flooding level A_D = 0.1. Methanol concentration is 1 M with a stoichiometry of 4, while air lambda is 10.

In Figure 6.42 the cost of this current production on the anode side can be seen, and as seen previously this follows the shape of anodic overpotential previously seen, with greater losses on the dry side where more current is produced, and lower losses on the flooded side where less current is produced.

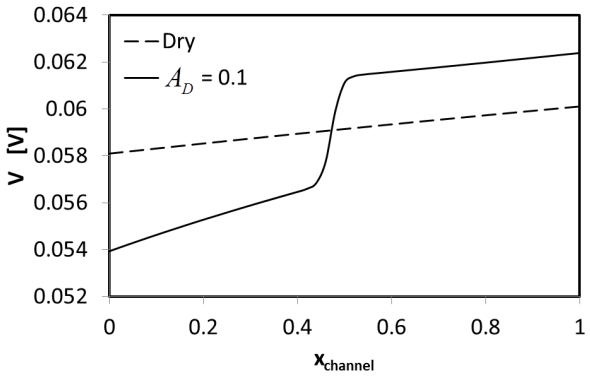

Figure 6.42: Anodic overpotential along the air channel for flooding level A_D = 0.1. Methanol concentration is 1 M with a stoichiometry of 4, while air lambda is 10.

Figure 6.43 shows local cathodic overpotential with a similar shape to less severe degrees of flooding, however here we see a 30 mV difference between flooded and reference cell at a relatively low load current of 100 mA cm^{-2}.

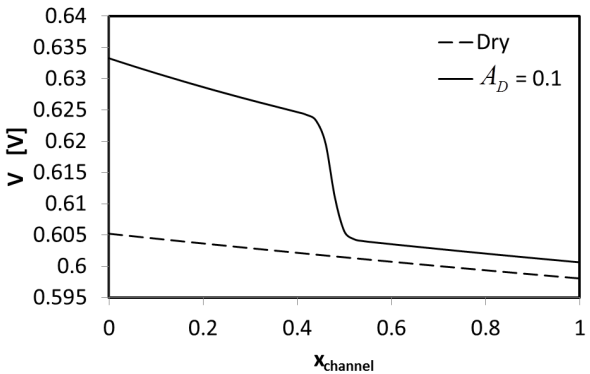

Figure 6.43: Cathodic overpotential along the air channel for flooding level A_D = 0.1.

Further analysis of Figure 6.34 in combination with the idea of limiting currents exhibits some interesting information. It is possible to divide the curve into several regions each representing a different mode of operation within the flooded cell. Figure 6.44 shows the curve of j^* vs. A_D divided into three parts. In the first part, corresponding to A_D greater than 0.23, cathodic limiting current is still higher than anodic limiting current. In this region current production in the flooded region can exceed that in the dry part, once the dry part has reached anodic limiting current; this leads the effect visible in Figure 6.32. Between an A_D of 0.23 and 0.13 the cathodic limiting current is in a similar range to anodic limiting current in the dry half. In this range of disruption the flip in local current 'power-house' between dry and flooded regions witnessed once nearing limiting current become less pronounced. Below 0.13 the cathodic limiting current drops below that of anodic limiting current. Here the flip does not occur. Current production in the flooded region can't exceed that of the dry region right up to full mass transport limitation on the dry side. Another point of note in Figure 6.44 is the axis intersect at j^* equal to zero. This point represents the tipping point at which electrolysis starts to occur.

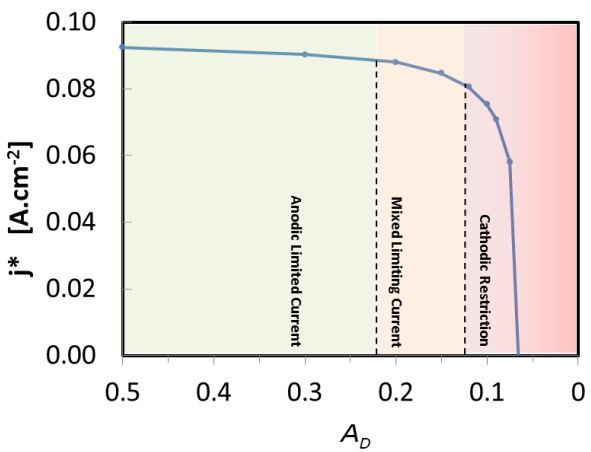

Figure 6.44: j* – the current at the air channel outlet (x=0) – plotted against the degree of flooding disturbance – . Showing regions of differing "limiting current modes".

High Current Region

Figure 6.45: shows j* for 3 different load currents: 50, 100 and 300 mA cm^{-2}. At lower currents the cell has ease compensating for flooding, and current production in the flooded region is lower relative to mean current. As current increases the flooded region needs to contribute more, as the dry half starts to run into mass transport limitation. This is counteracted at lower A_D by the increasing cost in cathodic overpotential, reflected in the shifting of the critical region to a higher A_D – to the left in Figure 6.45:.

The broken line curve in Figure 6.45: shows the ratio of limiting current in the flooded region – taken from the flooded half-cell polarisation curve – to the actual load current. This curve provides the distinction between non-critical, transition and critical regions. Where it is above 1 the flooded region is still able to compensate anodic limitation. Where this drops below 1 is classified as the transition region where limiting current at both electrodes plays a role. The critically flooded region is defined as the point where the limiting current density in the flooded region drops below 90 % of the load current.

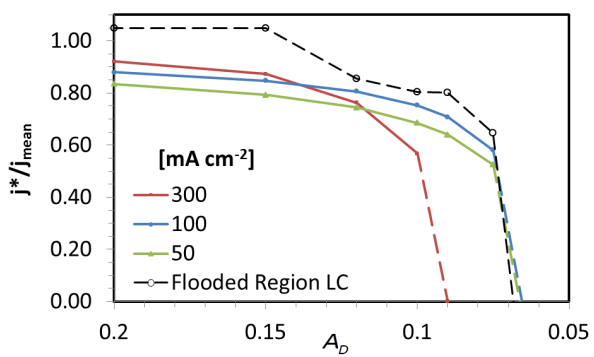

Figure 6.45: j* – the current at the air channel outlet (x=0) – plotted against the degree of flooding disturbance for $\frac{j^*_{lim}}{j}$ three different currents – 50 mA cm^{-2}, 100 mA cm^{-2} and 300 mA cm^{-2}.

6.6 Convergence

This section deals with the performance of the stack model. Data on convergence time and computational load are presented for the various simulations undertaken. These comparisons are meant to provide insight into strengths of the parallel model, and give an idea of computational requirements for each simulated case.

6.6.1 Normal Operation

Convergence for normal stack simulations is quick, and generally only requires a relatively loose mesh, with a grid of 300 by 300 grid points per cell being sufficient for resolving a point on the polarisation curve in less than twenty seconds. Each point needs just two passes of the main polarisation curve loop, with the solver sup-loops producing a solution within the residual conditions after the second solvation process. Figure 6.46 shows residuals from the electric model for a cell with uniform conditions and taken from a simulation done for the operational envelop series in section 6.3. The convergence condition is 10^{-3}, but because the residual on the converged iteration does not print, the graph appears to have a plateau-like shape. Interestingly the residual is never more than 1.03 10^{-3}, meaning that when the iteration feeds its values to the next point in the cycle to use as the starting point for solving the next point on the IV curve, the solution is already very close to convergence. The electric model solver then has no problems solving the new point in one pass.

Figure 6.46 is from a run with methanol lambda 1.5, and 1 M concentration, meaning that it represents a regime that is comparatively difficult for the solvers to resolve, due to high concentration gradients, and significant cross-over. This therefore represents the upper limit of difficulty for the solver, for uniformly operated stacks, and represents no challenge to the programme. The code still has a lot of ability to spare for dealing with trickier problems.

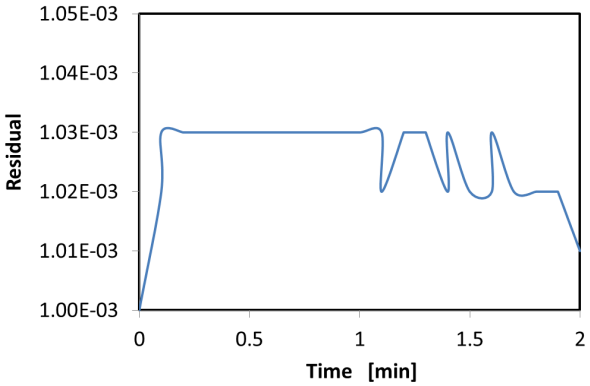

Figure 6.46: Electric model residual vs. Time for a reference cell in standard, normal operation, showing typical rapid conversion character.

6.6.2 Feed Disturbance

For cells with two disparate flow regimes the model is presented with more of a challenge. It has to resolve a sharp change in overpotential losses between the two regions, while dealing with the resulting gradients in feed concentration and current production; at all times maintaining the requisite average load current.

Figure 6.47 shows a typical convergence 'saw-tooth' for one such feed disturbance simulation. This is for a cell with a 50/50 split in area fed with methanol lambda 1.4 and 4. The spikes represent the start of a new point on the IV curve, which decay down with each iteration until the target residual of 10^{-3} is reached, whereupon all data is saved, and inputted as the initial conditions of the next iteration.

As time increases the IV loop progresses from the low to high current region on the polarisation curve, and as the curve approaches mass transport limitation, the step distance between each point becomes more significant. The initial conditions used from the previous iteration have an ever increasing residual, and this is indicated by the increasing peak height

in Figure 6.47. This in turn influences convergence time, by increasing the number of solver iterations needed to resolve domain variables.

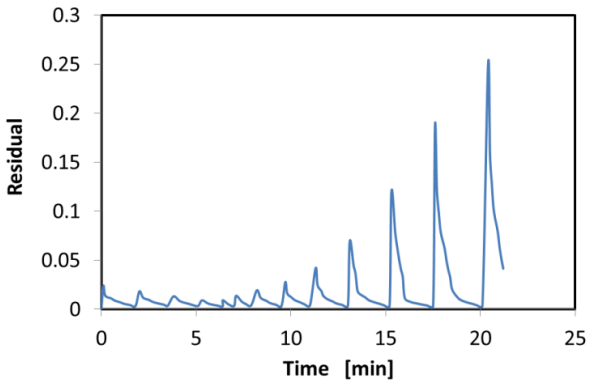

Figure 6.47: Electric model residual vs. Time for a typical feed disturbance simulation, showing characteristic saw tooth shape indicative of increasing computational load, and convergence time. Prematurely terminated after 22 minutes of simulation time.

We also see another factor that the code has to deal with, and that is premature termination. At 22 minutes the programme is abruptly terminated due to the allocated computing timeslot on JUROPA coming to an end. The code is designed to take these in stride, as each successive point that converges is saved to disk as a back-up. The code can then pick up where it left off, and Figure 6.48 shows one such continuation with the zero time adjusted to overlap with the point where the back-up is loaded (broken black line). Here the incomplete cycle is repeated (broken red line), and the polarisation curve solver then continues on (solid red).

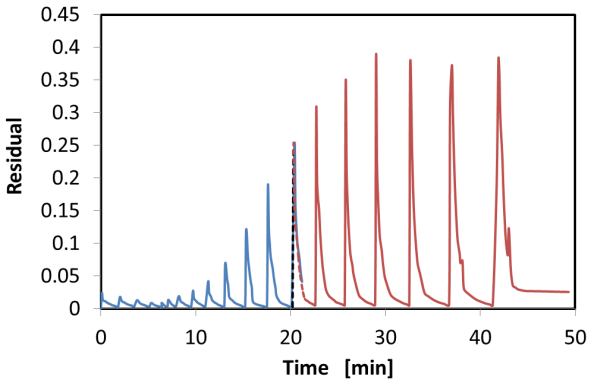

Figure 6.48: Electric model residual vs. Time for a typical feed disturbance simulation, showing characteristic saw tooth shape indicative of increasing computational load, and convergence time. This shows a single simulated case run in two computing sessions, with a break and subsequent continuation at 22 minutes (simulation time).

The continuation however runs into difficulty after a while, and this can be seen in the feature occurring at 45 minutes. The solver bottoms-out at a residual that is above the convergence residual. The code at this point has reached a point where it can no longer resolve the necessary point on the polarisation curve. This means that it cannot reconcile overpotential losses with the load current condition, and will not converge. At this point in the curve it is highly likely that overpotential losses have dropped below zero, and the model returns negative values, indicating that the fuel cell should have reversed its polarity.

Another notable feature, which indicates that the code is starting to have difficulties resolving can be seen in the final successfully resolved cycle and last, incomplete cycle, which have secondary spikes at 38 and 43 minutes respectively. These indicate that the solver was fixing on a stationary point, that turned out not to be the solution, and residual spikes once it has passed over this point.

The feed disturbance here represents an extreme case, and the 40 minutes necessary for a full polarisation curve is the upper limit that the user can expect for such experiments. Any reduction to the level of disturbance, or the disparity between feed regimes will improve convergence and reduce the necessary time for the simulation.

6.6.3 Cathode Flooding

In contrast to the feed disturbance simulations, cathode flooding causes two different regimes to manifest on the cathode side, and rather than splitting the cell vertically, the two disparate regions split the cell horizontally, with dry region on top, and flooded region on the bottom. Here there is a subtle difference in effects that the disruption of oxygen feed causes. On the anode side, feed is first under-used, and used up quickly to make up for the under-producing flooded zone. On the air side oxygen is used up in the dry, power-house zone, and then enters the flooded region. The increase in cross-over, and the sudden transition between sluggish, and compensatory current production cause the code to slow somewhat, in order to achieve convergence. Here it helpful to distinguish the difference between non-critically and critically disrupted cells, as the level of disruption also plays a significant part.

Non-critical Disruption

Figure 6.49 shows a convergence report for a non-critically disrupted cell. For the time below 10 minutes, the code converges each point on the polarisation curve on the second iteration. At 11 minutes, the code reaches the mass transport limited region, and each point starts to require more iterations for convergence. Although the typical saw-tooth shape is visible, the absolute magnitude of each spike is not as large as in Figure 6.48, and only reaches a maximum of 0.02 before non-convergence occurs. It shows the non-convergence feature at 38 minutes, with a stationary point 'mini-spike' at 37 minutes previously described in 6.6.2.

While this is considered a non-critical disturbance it requires at least 40 minutes for a polarisation curve. This represents the average for simulations in the non-critical flooding regime – A_D between 0.2 and 1.

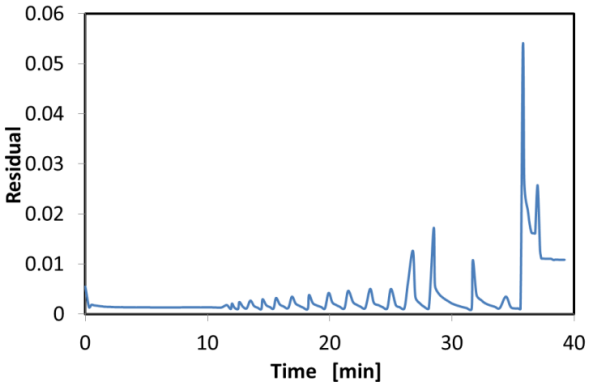

Figure 6.49: Electric model residual vs. Time for a typical cathode flooding simulation with a non-critical flooding amplitude parameter – between 0.2 and 1, showing characteristic saw-tooth behaviour until a non-convergence event occurs at 38 minutes.

Critical Disruption

Figure 6.50 shows a convergence report for a critically disrupted cell. Here absolute residual at the start of each cycle is larger than the non-critically disrupted simulation – between 0.02 and 0.08. The complete polarisation curve requires 80 minutes in comparison to non-critical disruption. This level of disruption represents the upper limit of what the code can handle with the number of processors assigned to this particular job, which divided a 5 cell stack over 80 processors and used a 600 by 600 grid point mesh per cell. While the grid resolution is sufficient, the best way to improve convergence time would be to invest more computing resources in the problem.

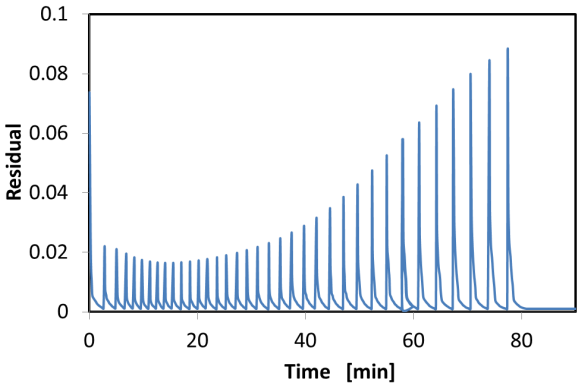

Figure 6.50: Electric model residual vs. Time for a typical cathode flooding simulation with a critical flooding amplitude parameter – below 0.15, showing characteristic saw-tooth behaviour until a non-convergence event occurs at 80 minutes.

7 Summary

The aim of this work was to model aspects of a DMFC stack based on a novel approach to fuel cell modelling. The model is primarily concerned with capturing large scale effects across a DMFC stack, and to capture physical effects that come about due to interactions between the multiple cells that comprise the stack.

The code framework was designed to be highly scalable allowing the user to adapt the model to any size stack, and distribute this model over a variable number of processors. The emphasis is on user control and flexibility, as well as having total control over the physical model. By having complete oversight of the physics governing the entire simulation, cogent statements can be made about the causality of the effects visible in its output.

The code is divided into two parts: Temperature and electric sub-models; with the electric model including the equations governing electrochemical characteristics. The model consists of mass and energy balances in three dimensions. Because cells are thin compared to their surface area, finite difference simplifications are used in both sub-models to reduce differential equations governing axial effects into linear terms. This reduces the 3D differential equations governing temperature and voltage into differential equations in a two dimensional plane that are equated to the generation term and the simplified axial transport term.

The temperature model incorporates thermal source and sink terms for heat from electrochemical reaction, water evaporation, cross-over and conduction. While the electric model determines BPP voltage from the profile of local current – delivered by the electro-chemical model. Acceleration from bubbles is accounted for by introducing a modelling parameter that specifies the resulting expansion of CO_2 based on current.

The code is composed of various iterative loops and procedures which serve different functions. These can be thought of like brackets in an equation, which compartmentalise discrete pieces of functionality.

The code uses two different well documented iterative numerical solver algorithms – a Poisson solver and a *ZeroIn* solver. The Poisson solver is used to find temperature and voltage distribution over the 2D mesh corresponding to the BPP. *ZeroIn* is a root finding solver, which is used within the electrochemical sub-model to determine overpotentials, and the corresponding local current at each point in the 2D plane.

Once the programme has allocated resources it initiates a loop that steps through a predefined polarisation curve. The electric and thermal models form the two main iterative blocks within this process, with the electrochemical sub-model procedure forming half of the electric model, the other half being the voltage solver. The thermal model is composed of temperature solver, and a segment responsible for solving boundary conditions.

Validation of the simulation was undertaken to produce meaningful results. This was done by comparing polarisation curves to experimental cells. Material, electrochemical performance and feed Parameters are matched between simulation and experiment, and modal specific parameters are tuned to give the best fit for a range of different feed concentrations and feed stoichiometries.

Parametric variation provides insights into stack optimisation. By varying concentration and anodic stoichiometry an operational envelope was developed based on limiting currents. This is further refined by adding realistic voltage constraints thus defining a parameter map of producible current vs. methanol feed concentration and stoichiometry.

Two experiments were devised to model failures in cell operation as part of the goal to explore malfunctions in cell operation. The first deals with disruptions to the fuel supply in a cell. Cells were modelled where half the cell area experienced a drop in anodic feed stoichiometry. It was established that those undisrupted parts of the cell lend stability to cell operation, which reduces high overpotentials caused in the disrupted regimes.

In the second experiment of cell malfunction a parametric variation was used to determine the impact of water flooding in the cathode. This highlighted again that cells are remarkably stable up to a certain critical point, whereupon they tip very quickly over into a

critical regime – typified by high overpotential losses. A simplified model was used to mimic flooding, and used to define where the boundaries between non-critical and critical flooding occur.

The code functions well for normal operation simulations with complete polarisation curve runs taking a few minutes. Convergence time increases with increasing disruption to cell operation with cell on the verge of forming bifunctional fuel cell / electrolysis operation requiring up to eighty minutes for a complete polarisation curve run.

8 Conclusions

This work unifies various physical models that tie together many aspects of cell operation and provide deeper insight into how stacks function.

The model combines equations for planer voltage and temperature distribution Eq. (3.1) and (3.30), with an electrochemical model that describes overpotential losses based on local catalytic activity, as well as transport losses from reactant transport (section 5.3). Additional model elements are introduced to describe specific failures in cell operation: Disruption of methanol feed, and flooding of the cathode GDL [73, 74].

This model is realised using self-written C++ code, which is designed to run on parallel processing computers, and tests where run on JUROPA, one of *Forschungszentrum Jülich's* supercomputers. The code is designed to give the operator control over all aspects of the model, as well as controlling the computational resources applied to the problem (section 7). Standard stacks of up to 20 cells take less than 10 minutes to run off full polarisation curves, while stacks with disruptions to normal operation can take up to 90 minutes for similar curves. Long convergence times can be mitigated by applying more processing capacity, with the average number of CPU's required for typical jobs ranging between 80 – 1000 CPU cores.

Three major experiments are reported; the first, an assessment of optimal stack operating regimes; the second and third concerned with disruptions to normal operation: Methanol feed disruption and flooding of the cathode GDL respectively.

To optimise a stack it was shown that a minimum concentration of 0.3 M, and methanol stoichiometry of above 10 is preferable. These feed conditions lead to low methanol crossover, and shallow gradients in local current along the channel length.

Feed disruptions to the cell took the form of disparate flow velocities between each half of its surface. One side was fed with $\lambda^a = 4$, with the other half with $\lambda^a = 1.4$. While gradients are steeper in the disrupted half, the stack shows remarkable stability, with the side

experiencing higher feed flow rate having a minor stabilising influence on overpotential losses (~10 mV).

A parameter study of the effect of cathode flooding showed that the cell current production flips between non-critical and critical regimes, with a rapid transition between the two. It was shown that the cell can handle flooding up to a point after which current production is suddenly restricted. For the operating parameters specified this critical point was related to a GDL water saturation of between 0.5 and 0.65, depending on how saturation is related to the oxygen diffusion coefficient.

9 References

1. Olah, G.A., A. Goeppert, and G.K.S. Prakash, *Methanol and Dimethyl Ether as Fuels and Energy Carriers*, in *Beyond Oil and Gas: The Methanol Economy*2009, Wiley-VCH Verlag GmbH & Co. KGaA. p. 185-231.

2. Olah, G.A., A. Goeppert, and G.K.S. Prakash, *Production of Methanol: From Fossil Fuels and Bio-Sources to Chemical Carbon Dioxide Recycling*, in *Beyond Oil and Gas: The Methanol Economy*2009, Wiley-VCH Verlag GmbH & Co. KGaA. p. 233-278.

3. Kriston, A., T. Szabó, and G. Inzelt, *The marriage of car sharing and hydrogen economy: A possible solution to the main problems of urban living.* International Journal of Hydrogen Energy, 2010. **35**(23): p. 12697-12708.

4. Shinnar, R., *The hydrogen economy, fuel cells, and electric cars.* Technology in Society, 2003. **25**(4): p. 455-476.

5. Stolten, D., *Wasserstoff: Alternative zu fossilen Energieträgern?*, in *Erneuerbare Energie*2011, Wiley-VCH Verlag GmbH & Co. KGaA. p. 128-132.

6. Boretti, A., *Renewable hydrogen to recycle CO2 to methanol.* International Journal of Hydrogen Energy, 2013. **38**(4): p. 1806-1812.

7. Aricò, A.S., V. Baglio, and V. Antonucci, *Direct Methanol Fuel Cells: History, Status and Perspectives*, in *Electrocatalysis of Direct Methanol Fuel Cells*2009, Wiley-VCH Verlag GmbH & Co. KGaA. p. 1-78.

8. Wang, Y., et al., *A review of polymer electrolyte membrane fuel cells: Technology, applications, and needs on fundamental research.* Applied Energy, 2011. **88**(4): p. 981-1007.

9. Dohle, H., J. Mergel, and D. Stolten, *Heat and power management of a direct-methanol-fuel-cell*

(DMFC) system. Journal of Power Sources. **111**: p. 268-282.

10. Wilkinson, D.P. and J. St-Pierre, *Durability*, in *Handbook of Fuel Cells*2010, John Wiley & Sons, Ltd.

11. Wilde, P.M., et al., *Structural and physical properties of GDL and GDL/BPP combinations and their influence on PEMFC performance.* Fuel Cells, 2004. **4**: p. 180 - 184.

12. Oedegaard, A., et al., *Influence of diffusion layer properties on low temperature DMFC.* Journal of Power Sources, 2004. **127**: p. 187.

13. Birgersson, E., et al., *Reduced Two-Phase Model for Analysis of the Anode of a DMFC.* Journal of The Electrochemical Society, 2004. **151**(12): p. A2157.

14. Wang, Z.H. and C.Y. Wang, *Mathematical Modeling of Liquid-Feed Direct Methanol Fuel Cells.* Journal of The Electrochemical Society, 2003. **150**(4): p. A508.

15. Nordlund, J. and G.r. Lindbergh, *A Model for the Porous Direct Methanol Fuel Cells Anode.* Journal of The Electrochemical Society, 2002. **149**(9): p. A1107.

16. Möst, M., M. Rzepka, and U. Stimming, *Analysis of the diffusive mass transport in the anode side porous backing layer of a direct methanol fuel cell.* Journal of Power Sources, 2009. **191**(2): p. 456-464.

17. Xu, C., T.S. Zhao, and Y.L. He, *Effect of cathode gas diffusion layer on water transport and cell performance in direct methanol fuel cells.* Journal of Power Sources, 2007. **171**(2): p. 268-274.

18. Xu, C., T.S. Zhao, and W.W. Yang, *Modeling of water transport through the membrane electrode assembly for direct methanol fuel cells.* Journal of Power Sources, 2008. **178**(1): p. 291-308.

19. Dohle, H., J. Mergel, and P.C. Ghosh, *DMFC at low air flow operation: Study of parasitic hydrogen generation.* Electrochimica Acta, 2007. **52**(19): p. 6060-6067.

20. Das, P.K., X. Li, and Z.-S. Liu, *Analysis of liquid water transport in cathode catalyst layer of PEM fuel cells.* International Journal of Hydrogen Energy, 2010. **35**(6): p. 2403-2416.

21. He, Y.-L., et al., *Numerical study of the effect of the GDL structure on water crossover in a direct methanol fuel cell.* International Journal of Hydrogen Energy, 2012. **37**(5): p. 4422-4438.

22. Kulikovsky, A.A., *A model for mixed potential in direct methanol fuel cell cathode and a novel cell design.* Electrochimica Acta, 2012. **79**: p. 52-56.

23. Birgersson, E., et al., *Reduced Two-Dimensional One-Phase Model for Analysis of the Anode of a DMFC.* Journal of The Electrochemical Society, 2003. **150**(10): p. A1368.

24. Liu, W. and C.-Y. Wang, *Modeling water transport in liquid feed direct methanol fuel cells.* Journal of Power Sources, 2007. **164**(1): p. 189-195.

25. Zhao, T.S., et al., *Mass transport phenomena in direct methanol fuel cells.* Progress in Energy and Combustion Science, 2009. **35**(3): p. 275-292.

26. Kulikovsky, A.A., *Optimal temperature for DMFC stack operation.* Electrochimica Acta, 2008. **53**(22): p. 6391-6396.

27. Pasaogullari, U. and C.-Y. Wang, *Two-phase transport and the role of micro-porous layer in polymer electrolyte fuel cells.* Electrochimica Acta, 2004. **49**(25): p. 4359-4369.

28. Wang, X. and T.V. Nguyen, *An experimental study of the liquid water saturation level in the cathode gas diffusion layer of a PEM fuel cell.* Journal of Power Sources, 2012. **197**: p. 50-56.

29. R.E. Meredith, C.W.T., in *Advances in Electrochemical Science and Engineering*, C.W. Tobias, Editor 1962, Interscience: New York, 1962

30. Zago, M., et al., *Water transport and flooding in DMFC: Experimental and modeling analyses.* Journal of Power Sources, 2012. **217**: p. 381-391.

31. Kulikovsky, A.A., *The regimes of catalyst layer operation in a fuel cell.* Electrochimica Acta, 2010. **55**(22): p. 6391-6401.

32. Wang, Z., Y. Liu, and V.M. Linkov, *The influence of catalyst layer morphology on the electrochemical performance of DMFC anode.* Journal of Power Sources, 2006. **160**(1): p. 326-333.

33. Wang, Q., et al., *A mathematical model and optimization of the cathode catalyst layer structure in PEM fuel cells.* Electrochimica Acta, 2004. **50**(2-3): p. 725-730.

34. M. L. Perry, J. Newman, and E.J. Cairns, *Mass transport in gas–diffusion electrodes: A diagnostic tool for fuel–cell cathodes.* Journal of the Electrochemistry Society, 1998. **145**(1): p. 5-15.

35. Havránek, A. and K. Wippermann, *Determination of proton conductivity in anode catalyst layers of the direct methanol fuel cell (DMFC).* Journal of Electroanalytical Chemistry, 2004. **567**(2): p. 305-315.

36. Boyer, C., et al., *Measurements of proton conductivity in the active layer of PEM fuel cell gas diffusion electrodes.* Electrochimica Acta, 1998. **43**(24): p. 3703 - 3709.

37. Wippermann, K., et al., *Influence of the ionomer type in direct methanol fuel cell (DMFC) anode catalyst layers on the properties of primary and secondary pores.* Journal of Power Sources, 2013. **228**: p. 57-67.

38. Gasteiger, H.A., J.E. Panels, and S.G. Yan, *Dependence of PEM fuel cell performance on catalyst loading.* Journal of Power Sources, 2004. **127**(1-2): p. 162-171.

39. Graham A. Hards, W. and R. Thomas R. Ralph, *Porous electrode for electrode assemblies in a fuel cell*, 1996, EP 0241432A2 (Oct, 1987) ; EP 0292431A2 (Nov, 1988) ; EP 0483085A2 (Apr, 1992) ; GB 9213124.2 (Sep, 1992); US 4804592 (Feb, 1989) Vanderborgh et al. 429/33; US 4816431 (Mar, 1989) Furuya et al. 502/101; US 4876115 (Oct, 1989) Raistrick; US 4877694 (Oct, 1989) Solomon et al.; US 5084144 (Jan, 1992) Reddy et al.; WO 88/06642 (Sep, 1988): US.

40. Wang, Q., et al., *Structure and performance of different types of agglomerates in cathode catalyst layers of PEM fuel cells.* Journal of Electroanalytical Chemistry, 2004. **573**(1): p. 61-69.

41. Murphy, O., G.D. Hitchens, and D.J. Manko, *High power density proton-exchange membrane fuel cells.* Journal of Power Sources, 1994. **47**(3): p. 353.

42. Gottesfeld, S. and T.A. Zawodzinski, *Advances in Electrochemical Science and Engineering*. Vol. 5. 1997: Wiley/VCH.

43. Zheng, W., A. Suominen, and A. Tuominen, *Discussion on the Challenges of DMFC Catalyst Loading Process for Mass Production.* Energy Procedia, 2012. **28**: p. 78-87.

44. Zhao, X., et al., *Influence of ionomer content on the proton conduction and oxygen transport in the carbon-supported catalyst layers in DMFC.* International Journal of Hydrogen Energy, 2012. **37**(12): p. 9845-9852.

45. Dohle, H. and K. Wippermann, *Experimental evaluation and semi-empirical modeling of U/I characteristics and methanol permeation of a direct methanol fuel cell.* Journal of Power Sources, 2004. **135**(1-2): p. 152-164.

46. Xu, C. and T.S. Zhao, *In situ measurements of water crossover through the membrane for direct methanol fuel cells.* Journal of Power Sources, 2007. **168**(1): p. 143-153.

47. Kulikovsky, A.A., *The effect of cathodic water on performance of a polymer electrolyte fuel cell.* Electrochimica Acta, 2004. **49**(28): p. 5187-5196.

48. Kulikovsky, A.A., *Analytical model of the anode side of DMFC: the effect of non-Tafel kinetics on cell performance.* Electrochemistry Communications, 2003. **5**(7): p. 530-538.

49. Kulikovsky, A., *A method for analysis of DMFC performance curves.* Electrochemistry Communications, 2003. **5**(12): p. 1030-1036.

50. Shaffer, C.E. and C.-Y. Wang, *Role of hydrophobic anode MPL in controlling water crossover in DMFC.* Electrochimica Acta, 2009. **54**(24): p. 5761-5769.

51. Matar, S. and H. Liu, *Effect of cathode catalyst layer thickness on methanol cross-over in a DMFC.* Electrochimica Acta, 2010. **56**(1): p. 600-606.

52. Kulikovsky, A.A., *A model for carbon and Ru corrosion due to methanol depletion in DMFC.* Electrochimica Acta, 2011. **56**(27): p. 9846-9850.

53. L. Gancs, et al., *Dissolution of Ru from PtRu Electrocatalysts and its Consequences in DMFCs.* ECS Transactions, 2006. **3**(1): p. 607-618.

54. Ferreira, P.J., et al., *Instability of Pt/C Electrocatalysts in Proton Exchange Membrane Fuel Cells.* Journal of The Electrochemical Society, 2005. **152**(11): p. A2256.

55. Chen, W., et al., *Test on the degradation of direct methanol fuel cell.* Electrochimica Acta, 2006. **51**(12): p. 2391-2399.

56. Cheng, T.T.H., N. Jia, and P. He, *Characterization of the Degree of Ru Crossover and Its Performance Implications in Polymer Electrolyte Membrane Fuel Cells.* Journal of The Electrochemical Society, 2010. **157**(5): p. B714.

57. Andersen, S.M., L. Grahl-Madsen, and E.M. Skou, *Studies on PEM fuel cell noble metal catalyst dissolution.* Solid State Ionics, 2011. **192**(1): p. 602-606.

58. Corpuz, A.R., et al., *Effect of a nitrogen-doped PtRu/carbon anode catalyst on the durability of a direct methanol fuel cell.* Journal of Power Sources, 2012. **217**: p. 142-151.

59. Hartmann, P. and D. Gerteisen, *Local degradation analysis of a real long-term operated DMFC stack MEA.* Journal of Power Sources, 2012. **219**: p. 147-154.

60. Kulikovsky, A.A., H. Scharmann, and K. Wippermann, *Dynamics of fuel cell performance degradation.* Electrochemistry Communications, 2004. **6**(1): p. 75-82.

61. Kulikovsky, A.A., *A method for detection and location of current-free spots in a fuel cell stack: Numerical study.* International Journal of Hydrogen Energy, 2011. **36**(7): p. 4449-4453.

62. Kulikovsky, A.A., *Electrostatic broadening of current-free spots in a fuel cell stack: The mechanism of stack aging?* Electrochemistry Communications, 2006. **8**(8): p. 1225-1228.

63. J.-H. Choi, et al., *Oxygen Reduction Electrocatalysis at Chalcogen-modified Ruthenium Cathodes.* ECS Transactions, 2006. **3**(1): p. 171-179.

64. Dixon, D., et al., *Degradation effects at the methanol inlet, outlet and center region of a stack MEA operated in DMFC.* Journal of Power Sources, 2011. **196**(13): p. 5538-5545.

65. Vera, M., *A single-phase model for liquid-feed DMFCs with non-Tafel kinetics.* Journal of Power Sources, 2007. **171**(2): p. 763-777.

66. Kulikovsky, A.A., *Model of the flow with bubbles in the anode channel and performance of a direct methanol fuel cell.* Electrochemistry Communications, 2005. **7**(2): p. 237-243.

67. Ko, D., et al., *Non-isothermal dynamic modelling and optimization of a direct methanol fuel cell.* Journal of Power Sources, 2008. **180**(1): p. 71-83.

68. Chen, C.-H. and T.-K. Yeh, *A mathematical model for simulating methanol permeation and the mixed potential effect in a direct methanol fuel cell.* Journal of Power Sources, 2006. **160**(2): p. 1131-1141.

69. Kulikovsky, A.A., *A physical model for catalyst layer impedance.* Journal of Electroanalytical Chemistry, 2012. **669**: p. 28-34.

70. Yoon, W. and A.Z. Weber, *Modeling Low-Platinum-Loading Effects in Fuel-Cell Catalyst Layers.* Journal of The Electrochemical Society, 2011. **158**(8): p. B1007.

71. Kulikovsky, A.A., *Polarization curve of partially degraded catalyst layer.* Electrochemistry Communications, 2010. **12**(12): p. 1780-1783.

72. Kulikovsky, A.A., *Heat balance in the catalyst layer and the boundary condition for heat transport equation in a low-temperature fuel cell.* Journal of Power Sources, 2006. **162**(2): p. 1236-1240.

73. McIntyre, J., et al., *Large–scale DMFC stack model: The effect of a condensation front on stack performance.* International Journal of Hydrogen Energy, 2013. **38**(8): p. 3373-3379.

74. McIntyre, J., et al., *Large-scale DMFC Stack Model: Feed Disturbances and Their Impact on Stack Performance.* Fuel Cells, 2012: p. n/a-n/a.

75. Kulikovsky, A.A., *A model for SOFC anode performance.* Electrochimica Acta, 2009. **54**(26): p. 6686-6695.

76. Kulikovsky, A.A., *Heat transport in the membrane–electrode assembly of a direct methanol fuel cell: Exact solutions.* Electrochimica Acta, 2007. **53**(3): p. 1353-1359.

77. Vernersson, T. and G. Lindbergh, *A model for mass transport in the electrolyte membrane of a DMFC.* Journal of Applied Electrochemistry, 2007. **37**(4): p. 429-438.

78. Scott, K., W. Taama, and J. Cruickshank, *Performance and modelling of a direct methanol solid polymer electrolyte fuel cell.* Journal of Power Sources, 1997.

79. Lu, G.Q. and C.Y. Wang, *Electrochemical and flow characterization of a direct methanol fuel cell.* Journal of Power Sources, 2004. **134**(1): p. 33-40.

80. Kulikovsky, A.A., *The effect of stoichiometric ratio λ on the performance of a polymer electrolyte fuel cell.* Electrochimica Acta, 2004. **49**(4): p. 617-625.

81. Liu, F. and C.-Y. Wang, *Water and methanol crossover in direct methanol fuel cells—Effect of anode diffusion media.* Electrochimica Acta, 2008. **53**(17): p. 5517-5522.

82. Eccarius, S., et al., *Experimental validation of a methanol crossover model in DMFC applications.* Journal of Power Sources, 2008. **179**(2): p. 723-733.

Figure 3.1: Stack schematic showing division of cell elements 'U_i'. FD approximations are indicated by yellow arrows, while red arrows show (axial) current. Blue arrows show in-plane effects that are calculated with solvers described in section 5.2.....39

Figure 3.2: Schematic of feed disruption simulation showing a feed reduction over half the cell area; where methanol stoichiometry is reduced from 4 to 1.4.....49

Figure 3.3: Schematic showing the variation of oxygen diffusivity in the cathode GDL along the channel. Partially flooded regime is modeled as a rapid but smooth transition between two different diffusivities – D_{Ox}^{dry} and D_{Ox}^{fld} – along the air channel. Reactant are in counter-flow, with the air inlet at x=1 and outlet at x=0. 51

Figure 4.1: 0D polarization curve fit using Maple's *non-linear fit* function, and compared with the low current region of an experimental cell polarization curve. 69

Figure 4.2: Schematic of CO_2 gas bubble channel formation showing a simplification of gas channels in the ABL, which are then wicked away by the anode feed stream.....72

Figure 6.1: Experimental polarization curves (points) for three methanol concentrations: 0.33 M, 0.5 M & 1 M, with curves from Maple's *non-linear fit* algorithm (lines). 75

Figure 6.2: Average methanol concentration (including gas slugs) along the anode channel for a cell operating at 400 mA cm^{-2} with a methanol stoichiometry of λ^a = 2 @ 500 mA cm^{-2}. 76

Figure 6.3: Anode flow velocity along the anode channel for three different methanol stoichiometries – λ^a = 2, 4 & 8 – at two different methanol starting concentrations: 0.5 M & 1 M, and k = 3. **Error! Bookmark not defined.**

Figure 6.4: Full comparison of Maple fitted and experimental polarization curves showing clear disparity in the mass transport limited region. 77

Figure 6.5: Comparison of Experimental and simulated polarization curves for four different starting methanol concentrations – 0.33 M, 0.5 M, 0.76 M & 1 M.....78

Figure 6.6: Effective diffusion coefficient transformed from experimentally derived limiting current plotted against methanol stoichiometry. 79

Figure 6.7: Effective diffusivity at high methanol stoichiometry calculated through limiting current equation (Eq. 5.12). Each point represents the asymptotic value for each curve in Figure 6.6. 80

Figure 6.8: Stack axial temperature profiles based on average cell temperature for four different stack lengths: 4, 6, 8 & 16 cells. 81

Figure 6.9: Local cell temperature profiles for cells from the end and middle of the stack. 82

Figure 6.10: Cell temperature profiles for a 10 cell stack. 83

Figure 6.11: Polarisation curves for three different methanol stoichiometries – 2, 4 & 8. 84

Figure 6.12: Local current profiles for three different methanol stoichiometries at an average load current of 100 mA cm^{-1} – λ^a of 2 (left), 4 (centre) & 8 (right). 85

Figure 6.13: Polarisation curves for methanol stoichiometry of 4 at three different methanol concentrations – C^0_{MeOH} of 0.5 M, 0.76 M & 1 M. 86

Figure 6.14: Local cell current profiles for methanol stoichiometry of 4 at 100 mA cm^{-2}, and three different methanol concentrations – C^0_{MeOH} of 0.5 M (left), 0.76 M (center) & 1 M (right). 86

Figure 6.15: Local cell crossover current profiles along the anode channel for two different methanol concentrations – 0.5 M & 1 M, and three different methanol stoichiometries – λ^a of 2, 4 and 8..... 87

Figure 6.16: Local methanol concentration along the anode channel for a feed concentration of 1 M and three different stoichiometries – 2, 4 & 8. 88

Figure 6.17: Relative anodic flow velocity for two feed concentrations – 1 M & 0.5 M – and three different methanol stoichiometries – 2, 4 & 8. ..... **Error! Bookmark not defined.**

Figure 6.18: Stack limiting current vs. methanol stoichiometry for three different anode feed concentrations – 0.5 M, 0.76 M & 1 M..... 89

Figure 6.19: Limiting current vs. methanol stoichiometry based on a 200 mV minimum individual cell voltage (solid), and 300 mV minimum average cell voltage (dashed) for three different anode feed concentrations – 0.5 M, 0.76 M & 1 M..... 90

Figure 6.20: Polarisation curve for three methanol feed concentrations – 0.25 M, 0.275 M & 0.3 M. 91

Figure 6.21: Local current profiles of (composite) reference case (left), disturbed cell (middle), and the difference between the two (right). 92

Figure 6.22: Local anodic overpotential profiles of (composite) reference case (left), disturbed cell (middle), and the difference between the two (right). 92

Figure 6.23: Local cathodic overpotential profiles of (composite) reference case (left), disturbed cell (middle), and the difference between the two (right). 93

Figure 6.24: Local current profiles, j, for λ^a = 4 and 1.4 reference cases. 93

Figure 6.25: Local polarization curves in the cell with two different flow regimes compared with their respective reference cases. L4 and L1.4 refer to λ^a = 4 and λ^a = 1.4, respectively. Solid curves show the reference case, while broken lines show the local polarization curves within the disrupted cell for each flow regime. The curve "Avg Disrupted Stack" refers to the stack averaged polarization curve. 94

Figure 6.26: Local current profiles of (composite) reference case (left), disturbed cell (middle), and the difference between the two (right). 95

Figure 6.27: Local anodic overpotential profiles of (composite) reference case (left), disturbed cell (middle), and the difference between the two (right). 96

Figure 6.28: Local cathodic overpotential profiles of (composite) reference case (left), disturbed cell (middle), and the difference between the two (right). 96

Figure 6.29: Local current profiles for a 5 cell stack, with middle cell – #3 – feed with two different methanol stoichiometries over each half of its area: λ^a = 4 and λ^a = 2....97

Figure 6.30: Cross-section of current along the y-axis of the disturbed cell. These are shown at three points along the channel – the start, middle and end corresponding to a x-coordinate (dimensionless) of 0.1, 0.5 and 0.9 respectively. 97

Figure 6.31: Schematic showing how current is diverted around a disparate flow regime. Current is "bent" around the lower feed regime indicated by the darker patch in cell B. 98

Figure 6.32: Schematic of oxygen diffusion showing the variation of oxygen diffusivity in the cathode GDL along the channel. Partially flooded regime is modelled as a rapid but smooth transition between

two different diffusivities – D_{Ox}^{dry} & D_{Ox}^{fld} – along the air channel. Reactant are in counter-flow, with the air inlet at x=1 and outlet at x=0.....99

Figure 6.33: Polarisation curve for a reference dry cell, and three levels of (non-critical) flooding corresponding to a flooding amplitude parameter, A_D = 0.2, 0.5 & 0.75. 100

Figure 6.34: Polarisation curves for dry reference, stack average and two half-cell polarisation curves for dry and flooded regions.....101

Figure 6.35: Local cell current along the channel for dry reference cell and four levels of flooding: A_D = 0.075, 0.1, 0.2 & 0.3. 102

Figure 6.36: j* – the current at the air channel outlet (x=0) – plotted against the flooding parameter – A_D . 103

Figure 6.37: Anodic overpotential along the air channel for five different flooding parameters: A_D = 0, 0.075, 0.1, 0.2 & 0.3. 103

Figure 6.38: Cathodic overpotential along the air channel for five different flooding parameters: A_D = 0, 0.075, 0.1, 0.2 & 0.3.....104

Figure 6.39: Local limiting current for both anode and cathode, showing the minimum limiting current (broken line) for A_D =0.2. 105

Figure 6.40: Local current density and local limiting current shapes for mean cell current densities of 300 mA cm^{-2}, 400 mA cm^{-2} and 440 mA cm^{-2} A for a flooding parameter of A_D =0.2. 106

Figure 6.41: Anodic overpotential for three cell current densities: 300 mA cm^{-2}, 400 mA cm^{-2} and 440 mA cm^{-2}. 107

Figure 6.42: Cathodic overpotential for three cell current densities: 300 mA cm^{-2}, 400 mA cm^{-2} and 440 mA cm^{-2}. 108

Figure 6.43: Local cell current along the channel for dry reference cell and flooding level A_D = 0.1. 109

Figure 6.44: Anodic overpotential along the air channel for flooding level A_D = 0.1. 110

Figure 6.45: Cathodic overpotential along the air channel for flooding level A_D = 0.1 110

Figure 6.46: j* – the current at the air channel outlet (x=0) – plotted against the degree of flooding disturbance – . Showing regions of differing "limiting current modes". 111

Figure 6.47: j* – the current at the air channel outlet (x=0) – plotted against the degree of flooding disturbance for $\frac{j^*_{lim.}}{J}$ three different currents – 50 mA cm^{-2}, 100 mA cm^{-2} and 300 mA cm^{-2}. 112

Figure 6.48: Electric model residual vs. Time for a reference cell in standard, normal operation, showing typical rapid conversion character. 115

Figure 6.49: Electric model residual vs. Time for a typical feed disturbance simulation, showing characteristic saw tooth shape indicative of increasing computational load, and convergence time. Prematurely terminated after 22 minutes of simulation time. 116

Figure 6.50: Electric model residual vs. Time for a typical feed disturbance simulation, showing characteristic saw tooth shape indicative of increasing computational load, and convergence time. This shows a single simulated case run in two computing sessions, with a break and subsequent continuation at 22 minutes (simulation time). 117

Figure 6.51: Electric model residual vs. Time for a typical cathode flooding simulation with a non-critical flooding amplitude parameter – between 0.2 and 1, showing characteristic saw-tooth behaviour until a non-convergence event occurs at 38 minutes. 119

Figure 6.52: Electric model residual vs. Time for a typical cathode flooding simulation with a critical flooding amplitude parameter – below 0.15, showing characteristic saw-tooth behaviour until a non-convergence event occurs at 80 minutes. 120

Band / Volume 276
Pyrochlore as nuclear waste form: actinide uptake and chemical stability
S. C. Finkeldei (2015), IX, 155 pp
ISBN: 978-3-95806-072-2

Band / Volume 277
Herstellung von Elektrodenstrukturen für Lithium-Ionen-Dünnschichtbatterien
A. Bünting (2015), v, 151 pp
ISBN: 978-3-95806-073-9

Band / Volume 278
Keramiken des Monazit-Typs zur Immobilisierung von minoren Actinoiden und Plutonium
J. M. Heuser (2015), viii, 212 pp
ISBN: 978-3-95806-076-0

Band / Volume 279
IEK-3 Report 2015
Systems Research and Engineering for a Sustainable Energy Supply
(2015)
ISBN: 978-3-95806-077-7

Band / Volume 280
IEK-3 Report 2015
Systemforschung und –technik für eine nachhaltige Energieversorgung
(2015)
ISBN: 978-3-95806-078-4

Band / Volume 281
Integration of the German energy transition in the EU-context
A. Ernst (2015), 76 pp
ISBN: 978-3-95806-079-1

Band / Volume 282
Modelling and Experimental Validation of the Viscosity of Liquid Phases in Oxide Systems Relevant to Fuel Slags
G. Wu (2015), XVI, 170 pp
ISBN: 978-3-95806-081-4

Band / Volume 283
Entwicklung von geträgerten protonenleitenden Dünnschichtmembranen für die Wasserstoffabtrennung
W. Deibert (2015), XI, 117 pp
ISBN: 978-3-95806-082-1

Band / Volume 284
Thermochemische Beständigkeit von keramischen Membranen und Katalysatoren für die H_2-Abtrennung in CO-Shift-Reaktoren
E. M. H. Forster (2015), X, 137 pp
ISBN: 978-3-95806-084-5

Band / Volume 285
Spektrale aktinische Flussdichten und Photolysefrequenzen - Untersuchungen in der atmosphärischen Grenzschicht und der freien Troposphäre
I. M. Lohse (2015), VI, 111, VII-XXIII pp
ISBN: 978-3-95806-086-9

Band / Volume 286
Neue Charakterisierungsmethoden für die Gasdiffusionslage in PEM-Brennstoffzellen vor dem Hintergrund produktionsprozessbedingter Materialschwankungen
S. M. Bach (2015), VIII, 149 pp
ISBN: 978-3-95806-088-3

Band / Volume 287
Using the anisotropy of electrical properties for the characterization of sedimentological structures and preferential flow processes
S. Al-Hazaimay (2015), xxii, 94 pp
ISBN: 978-3-95806-090-6

Band / Volume 288
Aktivitätsuntersuchungen und Methoden zur Regeneration von Katalysatoren für die autotherme Reformierung von Dieselkraftstoffen
K. Löhken (2015), II, 147 pp
ISBN: 978-3-95806-093-7

Band / Volume 289
Large-Scale Three Dimensional Modelling of a Direct Methanol Fuel Cell Stack
J. W. McIntyre (2015), 138 pp
ISBN: 978-3-95806-094-4

Energie & Umwelt /
Energy & Environment
Band / Volume 289
ISBN 978-3-95806-094-4